Mechanical & Aerospace Engineering Theses & Dissertations

Mechanical & Aerospace Engineering

Summer 1986

An Analytical and Experimental Study of Clearance and Bearing-Bypass Load Effects in Composite Bolted Joints

Rajiv Vikas Arun Naik
Old Dominion University

Follow this and additional works at: https://digitalcommons.odu.edu/mae_etds

Part of the Mechanical Engineering Commons

AN ANALYTICAL AND EXPERIMENTAL STUDY OF CLEARANCE AND BEARING-

BYPASS LOAD EFFECTS IN COMPOSITE BOLTED JOINTS

by

Rajiv Vikas Arun Naik
B.Tech., June 1979, Indian Institute of Technology, Bombay, India
M.S., June 1982, University of Maine at Orono

A Dissertation Submitted to the Faculty of
Old Dominion University in Partial Fulfillment of the
Requirements for the Degree of

DOCTOR OF PHILOSOPHY

ENGINEERING MECHANICS

OLD DOMINION UNIVERSITY
August, 1986

Approved by:

_____

_____

_____

_____

_____

ABSTRACT

AN ANALYTICAL AND EXPERIMENTAL STUDY OF CLEARANCE AND BEARING-
BYPASS LOAD EFFECTS IN COMPOSITE BOLTED JOINTS

Rajiv Vikas Arun Naik
Old Dominion University, 1986
Director: Dr. Ram Prabhakaran
Co-Director: Dr. John H. Crews, Jr.

A combined analytical and experimental study is conducted
to determine the effects of clearance and bearing-bypass loading for
mechanically fastened joints in composites. A simple method of
analysis is developed to account for the nonlinear effects of bolt-
hole clearance. The nonlinear load-contact variations for clearance-
fit fasteners are also measured using specially instrumented
fasteners. For a quasi-isotropic graphite/epoxy laminate, results
show that the contact arc as well as the peak stresses around the
hole and their locations are strongly influenced by the clearance.
After a slight initial nonlinearity, the peak stresses vary linearly
with applied load. The typical clearance levels are shown to have
only a minor influence on the overall joint stiffness.

Quasi-isotropic graphite/epoxy laminates (T300/5208) are
tested under combined bearing and bypass loading to study failure
modes and strengths. Radiographs are made after damage onset and
after ultimate load to examine the failure modes. Also the laminate
stresses near the bolt-hole are calculated for each test condition,

and then used with appropriate failure criteria to analyze the test data. The tension data show a linear interaction for combined bearing and bypass loading with damage developing in the net-tension mode and growing to failure in the same mode. Failure modes are more complex in compression. The compression bearing-bypass strengths for damage-onset show an unexpected interaction involving the bearing mode. Compressive bypass loads reduce the bearing strength by decreasing the bolt-hole contact arc and thus increasing the severity of the bearing loads. Bearing damage-onset, for compressive bearing-bypass loads, causes a weakening of the offset-section leading to ultimate failure in the offset compression-bearing mode. Damage-onset is predicted reasonably well using the peak stresses at the hole. Strength predictions indicate that damage corresponding to ultimate strength is governed by the maximum stress near the hole.

This investigation will help improve the basic under-standing of composite bolted joints and lead to better structural design procedures.

ACKNOWLEDGEMENTS

The author wishes to express his sincere gratitude to his advisor Dr. Ram Prabhakaran, for all the help and effort provided during the course of this study at Old Dominion University. He is also indebted to Dr. John H. Crews, Jr., of the NASA Langley Research Center, whose friendly guidance and direction made this work possible.

Special thanks are due to Dr. A. Sidney Roberts, Jr. for his support through the Aeronautics Research Participation Program, grant number NGR 47-003-052, which included invaluable accessibility to research facilities at the NASA Langley Research Center in Hampton, Virginia. The author also wishes to thank researchers at the NASA Fatigue and Fracture Branch for their help, encouragement, and valuable suggestions and comments.

The author is very grateful to his wife, Vibha, for painstakingly typing the preliminary and final stages of the manuscript, and also for her patience, help, and considerable understanding. Finally, the author is also grateful to his parents Mr. and Mrs. A. S. Naik for their constant support and encouragement in this endeavor.

ii

TABLE OF CONTENTS

iii

v

LIST OF TABLES

vi

LIST OF FIGURES

viii

ix

x

LIST OF SYMBOLS

a_{oc}	compression characteristic dimension for average-stress failure criterion, m
a_{os}	shear characteristic dimension for average-stress failure criterion, m
a_{ot}, d_{ot}	tension characteristic dimension for average-stress failure criterion, m
c	radial bolt-hole clearance, m
c_d	diametrical bolt-hole clearance, %
c	notch sensitivity factor, m^{-1}
C_{bc}	coefficient for compression bearing damage-onset prediction
C_{bt}	coefficient for tension bearing damage-onset prediction
C_{nc}	coefficient for net-compression damage-onset prediction
C_{nt}	coefficient for net-tension damage-onset prediction
d	hole diameter, m
e	specimen edge distance, m
E	Young's modulus for laminate, MPa
E_1, E_2	ply modulus in fiber and transverse directions, MPa
f	material fringe value, N/m
G	laminate shear modulus, MPa
G_{12}	ply shear modulus, MPa
k	bypass ratio, S_{bp}/S_g
K_{bb}	bearing stress concentration factor

K_I	stress-intensity factor, $\text{MPa}\sqrt{m}$
K_{IC}	laminate fracture toughness, $\text{MPa}\sqrt{m}$
K_o	constant in modified point-stress criterion, $\sqrt{m}$
K_{tb}	tension stress concentration factor
L_t	tension length, m
m	exponential parameter in modified point-stress criterion
N	fringe order
P, P_g	applied load, N
P_b	bearing load, N
P_{bp}, P_p	bypass load, N
P_u	ultimate load, N
r, θ	polar coordinates, m and degrees
r_b	bolt radius, m
r_c	radial distance to characteristic curve, m
r_o	characteristic dimension for point-stress criterion, m
r_{ot}, r_{oc}	characteristic distance for net-tension, net-compression
r_{ocb}	and offset compression-bearing mode, respectively, m
r_{ox}, r_{oy}	distances to characteristic curve along x- and y-axis, m
R	hole radius, m
R_o	reference radius in modified point-stress criterion, m
S	ply shear strength, MPa
S_b, S_b^*	nominal bearing stress, P_b / dt, MPa
S_{bp}	nominal bypass stress, P_{bp} / wt, MPa
S_{bu}	ultimate bearing strength, MPa
S_c	shear strength of symmetric cross-ply laminate, MPa
S_g	nominal gross-section stress, P_g / wt, MPa
S_{np}	nominal net-section stress, $P_{bp} / (w-d)t$, MPa

t	laminate thickness, m
t_1	ply thickness, m
u, v	x and y displacements, m
w	laminate width, m
x, y	Cartesian coordinates, m
X_c , X_t	compressive and tensile strengths along x-axis, MPa
Y_c , Y_t	compressive and tensile strengths along y-axis, MPa
β	bearing-bypass ratio, S_b / S_{np}
δ	hole elongation, m
θ_c	contact angle, degrees
θ_1 , θ_2	contact angles for dual contact, degrees
θ_f	angular location of failure, degrees
μ	coefficient of friction
ν_{12}	Poisson's ratio
σ_{bc}	critical stress for compression bearing damage-onset, MPa
σ_{bt}	critical stress for tension bearing damage-onset, MPa
σ_{bu}	ply strength for equal biaxial loading, MPa
σ_{cu}	ultimate compressive strength for laminate, MPa
σ_{nc}	critical stress for net-compression damage-onset, MPa
σ_{nt}	critical stress for net-tension damage-onset, MPa
σ_{rr} , $\sigma_{\theta\theta}$	polar stress components, MPa
σ_{tu}	ultimate tensile strength for laminate, MPa
σ_{xx} , σ_{yy}	Cartesian stress components, MPa
σ_1 , σ_2	ply stresses parallel and normal to fibers, MPa
σ_{12} , τ_{12}	ply shear stress, MPa
τ_{xy}	Cartesian shear stress, MPa

CHAPTER 1

INTRODUCTION

Composite structures offer advantages over metal structures for weight-critical aerospace applications. As a result, composite aerospace structures are being increasingly used. Unfortunately, however, many of the current structural design procedures, developed through years of experience with metals, do not apply directly to composites. This is especially true for predictions of strength. In contrast to metals, which typically fail by a single crack that grows in a self-similar manner, composite failures are very complex. Composites exhibit failure mechanisms involving localized micro-damage such as matrix cracking and fiber debonding followed by macro-damage in the form of fiber failures and delamination.

Failures that develop in structures usually originate at joints. For composite structures, mechanical fastening is the preferred joining technique despite the fact that fasteners seriously weaken composites. Within a joint, fasteners introduce severe load concentrations. Furthermore, fastener holes give rise to high stress concentrations. Mechanically fastened joints in composites display three principal failure modes [1]*- net-section tension, bearing, and shearout (see Fig. 1). Furthermore, interactions can exist between these failure modes [2]. A failure that initiates in one mode can

---

* Numbers in brackets indicate references.

LOADED HOLE SPECIMEN

NET-TENSION FAILURE

SHEAROUT FAILURE

BEARING FAILURE
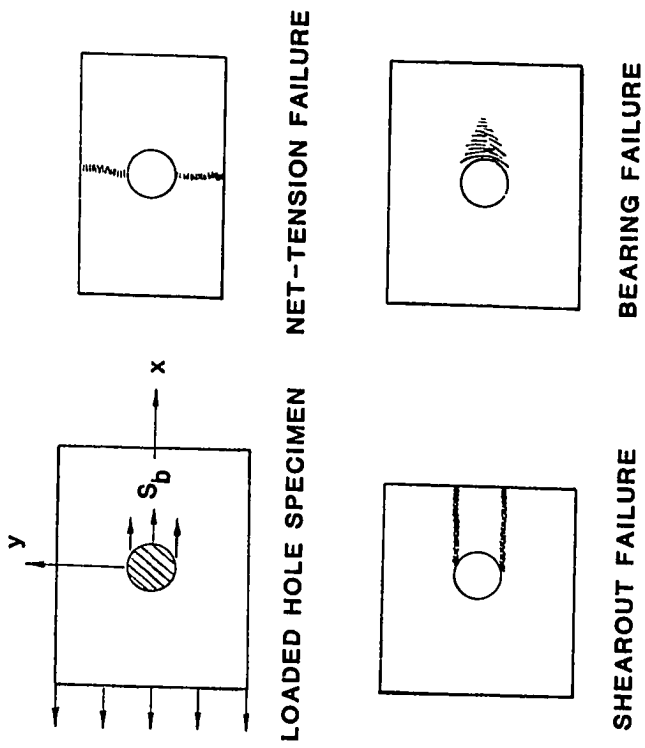
Fig. 1   Failure modes for laminates with loaded holes.

amplify the stresses associated with a second mode and thereby lead to failure by this second mode. In general, there are three categories of parameters that affect the failure of mechanically fastened joints in composites. They are:

(1) <u>Material parameters</u>: material properties of fiber and resin, fiber volume fraction, fiber orientation and stacking sequence.

(2) <u>Configurational parameters</u>: hole size, bolt geometry, bolt-hole clearance, washer size, plate thickness, joint geometry and clamping force.

(3) <u>Environmental parameters</u>: loading type, moisture content and temperature of surrounding air.

It is clear that, in view of the very large number of variables involved, a complete characterization of composite joint behavior is very difficult. Current design procedures for composite joints typically involve numerous simplifying assumptions and therefore do not properly account for all of the composite damage mechanisms. Such procedures usually lead to very conservative designs in which the advantages of composites are not fully exploited. The present research seeks to improve the basic understanding of composite joints and thereby could lead to better structural design procedures.

1.1 Material Parameters

One would expect that fiber arrangement in laminated composites affects the strength of the laminate. Different fiber orientations produce different constitutive elastic properties and therefore different stress patterns. Collings [3] demonstrated that fiber orientations had a definite influence on the failure of

mechanically fastened joints. For (0/±45) laminates he found that bearing, net tension, and shearout failures were dependent on the percentage of $0°$ plies in the laminate. With 50-60% of $0°$ plies he obtained optimum strengths in the three basic failure modes. His studies further revealed that fiber orientation also influenced the position around the hole circumference at which failure was initiated. For the (0/±45) laminates failure initiated at $\theta = 45°$, ($\theta°$ to the loading axis) for the (0/90) laminates at $\theta = 0°$, and for (0/±60) laminates at $\theta = 30°$. These results were in general agreement with the theory proposed by Waszczak and Cruse [4] in which it was suggested that failure initiation occurred at points on the circular boundary where fibers were either tangential or normal to the boundary.

Quinn and Matthews [5] investigated the bearing strength of glass/epoxy laminates and suggested that placing 90-degree plies (perpendicular to the load direction) at or near the surface improved bearing strength. They also found that failure mode depended on the stacking sequence. Collings [3] further studied the effect of stacking sequence on the strength of graphite/epoxy joints. He concluded that different stacking sequences resulted in differences of only 2% and 6% in shearout and net tension strength, respectively. Differences of 16%, however, were shown for bearing strength. In general, the most homogeneous stacking sequences produced better bearing strengths.

A better understanding of the influence of fiber orientation and stacking sequence on the stress patterns around a loaded hole can be vividly obtained by photoelasticity. Prabhakaran [6] applied the methods of photo-orthotropic elasticity to study

bolted joints in glass/epoxy composites. The differences in the
stress patterns for the quasi-isotropic and unidirectionally-
reinforced models are clearly evident from the isochromatic fringe
patterns. Hyer and Liu [7] also determined the stresses, using
photoelasticity, in quasi-isotropic, unidirectional and angle-ply
glass/epoxy laminates. Crews et al [8] computed stresses, using the
finite element method, for various fiber orientations and stacking
sequences in graphite/epoxy laminates. For an infinite pin-loaded
laminate they found that the $[0/\pm45]_s$ laminates had a stress
concentration factor (SCF) that was 59% lower than the 0°-
unidirectional laminates. This suggests that the addition of $\pm45^\circ$-
plies to a $[0^\circ]$ laminate reduces the SCF and is in general agreement
with the experimental results of Collings [3].

1.2 Configurational Parameters

This group of parameters includes the geometrical
dimensions of the bolt, washer, hole, and plates. The clamping force
and bolt-hole clearance are also important configurational
parameters. Basically, there is the choice between screws, rivets,
and bolts. Screws give the lowest load-carrying capacity. Whether
self-tapping or screwed into tapped holes, extensive damage is done
to the laminate. Riveted joints give adequate strength in high-duty
composites in thicknesses up to about 3 mm. However, due to the
nature of the riveting process the closing force is not readily
controlled and in some cases may cause damage to the laminate. Bolts
offer the greatest strength for mechanically fastened joints in
composites. The washers may dig into the laminate if the bolts are

excessively overtightened. The washer size can influence strength and it is important, as reported by Stockdale and Matthews [9], that the hole in the washer should be a close fit to the bolt. Another parameter that influences the strength of bolted joints is the ratio of hole diameter (d) to plate thickness (t). The bearing strength reduces as (d/t) increases [3] for graphite/epoxy laminates. Kretsis and Matthews [10] obtained similar results for the effects of the (d/t) ratio on glass/epoxy laminates.

The spacings between the rows and the columns of fasteners in a multi-fastener joint (see Fig. 2) also influences the joint strength. In order to simplify the analysis of a multi-fastener joint, it can be represented as an array of single-fastener coupons. The width w and end distance e of such single-fastener coupons can be varied to evaluate the influence of joint geometry on strength. In 1974, Van Siclen [11] studied the effects of width and end distance on the strength and failure modes of single-fastener joints. He concluded that the net-tension strength for a particular graphite/epoxy laminate varied with the width-to-hole diameter (w/d) ratio. Also, the shearout strength varied with the (e/d) ratio and finally, the bearing strength was a constant and was the maximum load that could be transferred at the joint. Hart-Smith [12] obtained similar results for the influences of w/d and e/d ratios on strength. Figure 3 shows the effects of w/d and e/d ratios for quasi-isotropic, graphite/epoxy laminates tested using the procedures described in Ref. 14. For w/d values less than about 4, failures occurred by the net-tension mode and joint strength increased as w/d increased
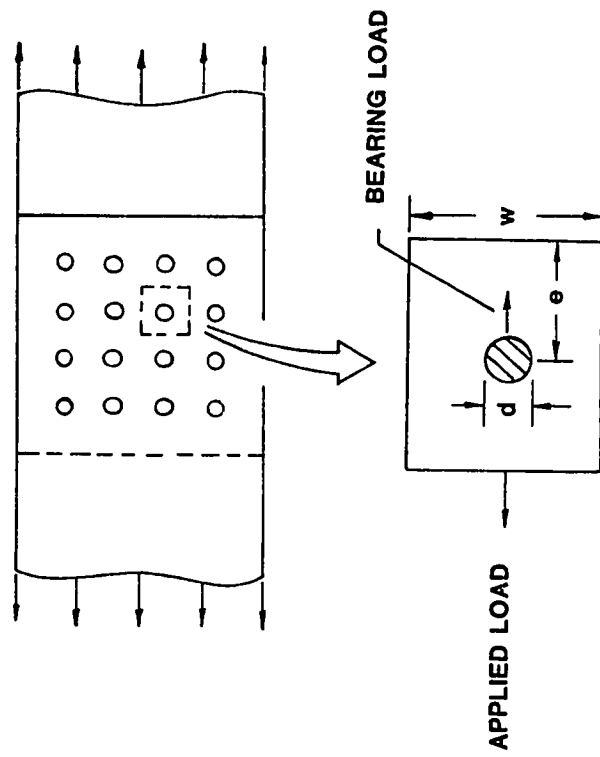
Fig. 2   Multifastener joint and a single-fastener element.
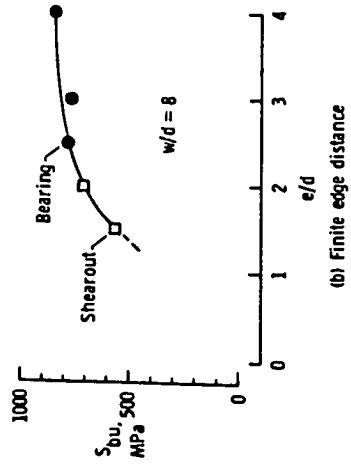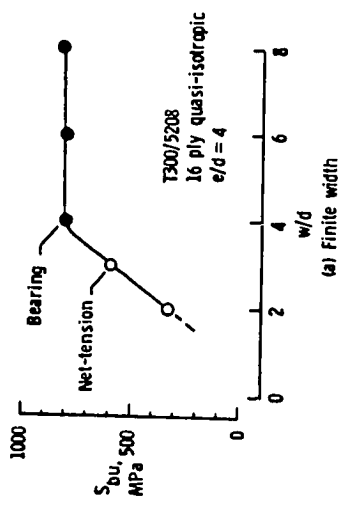
Fig. 3 Laminate strength for w/d and e/d ranges.

(see Fig. 3(a)). Wider specimens (w/d > 4) failed in the bearing mode and bearing strength was unaffected by w/d. Similar results were observed for e/d ratios. The shearout failure mode for e/d < 2 changed to a bearing mode for larger e/d ratios (see Fig. 3(b)). The trends exhibited in Figs. 3(a) and 3(b) give significant information for joint design. One can assume that bearing strength is a laminate property, since it is not influenced by joint geometry (w/d and e/d). A joint should be designed to fail in the bearing mode to use the full strength of the laminate.

A better understanding of the influence of width and end distance on laminate strength can be obtained by looking at the stresses around a loaded hole. For a quasi-isotropic laminate with a loaded hole, the effects of width and end distance are shown in Figs. 4 and 5. These stresses were calculated using the finite-element analyses from Ref. 8. The distributions along the y-axis, the x-axis, and the shearout plane (y = d/2) correspond to the three failure modes for a loaded hole. In Fig. 4 results are compared for a wide (w/d = ∞) and a narrow (w/d = 3) laminate. The narrow width amplifies the peak σ_{xx} stress on the net section, Fig. 4(a), by about 80 percent compared to the infinite case. The peak bearing and shearout stresses, Figs. 4(b) and 4(c), are influenced by less than 20 percent. This explains the observed trend for narrow laminates to fail in the net-tensile mode rather than in the bearing or shearout modes. The effects of end distance e on local stresses are shown in Fig. 5. Both the peak net-section tensile stress, Fig. 5(a), as well as the peak shearout stress, Fig. 5(c), are elevated for
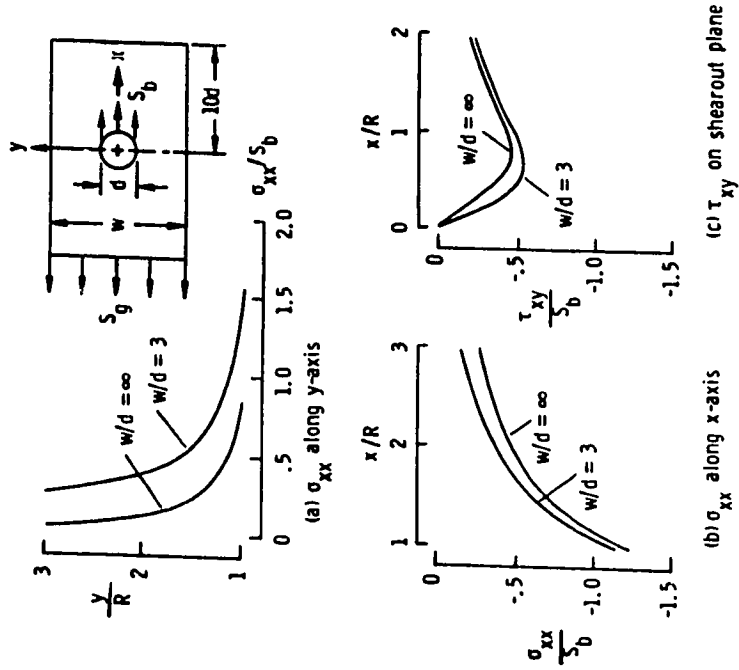
Fig. 4   Stresses near a loaded hole in finite-width quasi-isotropic laminate.
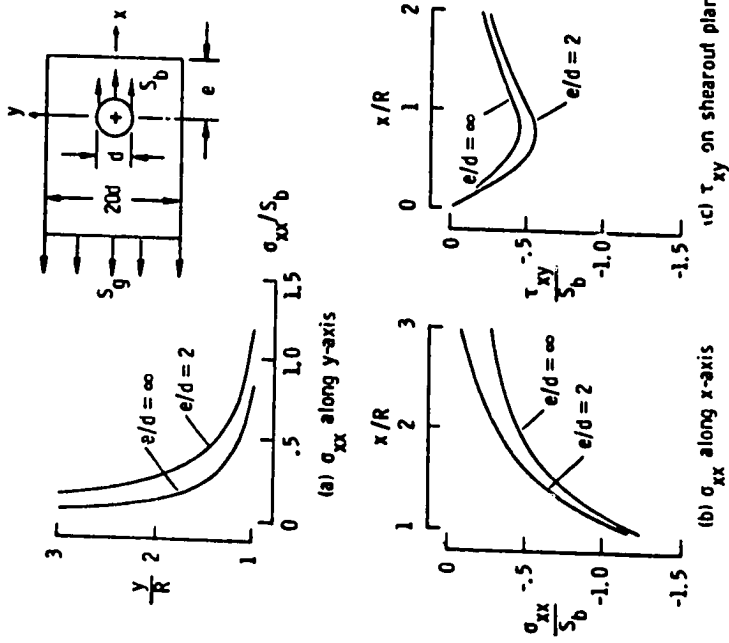
Fig. 5   Stresses near a loaded hole in a quasi-isotropic laminate with a finite edge distance.

e/d = 2, compared to the infinite laminate case. However, test
results in Fig. 3(b) show that only the shearout stresses are
critical for small e/d values. The effects of w/d and e/d on
laminate strength will be discussed further as the various strength
prediction approaches are reviewed.

The amount of clamping force (or lateral constraint)
exerted by the bolt clamp-up torque strongly influences the bearing
strength. Crews [13] reported higher strengths for larger clamp-up
levels. The larger clamp-up torques improved bearing strength by
more than 100 percent compared to the unconstrained case. Collings
[3] noted that there is an upper limit of clamping force beyond which
an additional increase will have little effect on the strength of a
composite joint.

In most joints some clearance, c, exists between the
fastener and the hole. Crews and Naik [14] illustrated the influence
of clearance for a pin-loaded hole in a graphite/epoxy laminate. For
a clearance of only 0.8 percent of hole diameter, the peak tangential
stress $(\sigma_{\theta\theta})$ around the hole boundary was 12 percent higher than the
snug-fitting (c = 0) case (see Fig. 6). Also the $\sigma_{\theta\theta}$ peak had
shifted its location by 15° as compared to the snug-fitting case. It
is important to be able to determine the location of the peak value
of $\sigma_{\theta\theta}$ because the onset of damage in composite joints may start at
this location. In many cases, then, an analysis with a "no
clearance" assumption may not be appropriate for real joints. Clear-
ance is difficult to account for in a stress analysis because it
leads to a contact region at the bolt-hole interface that increases
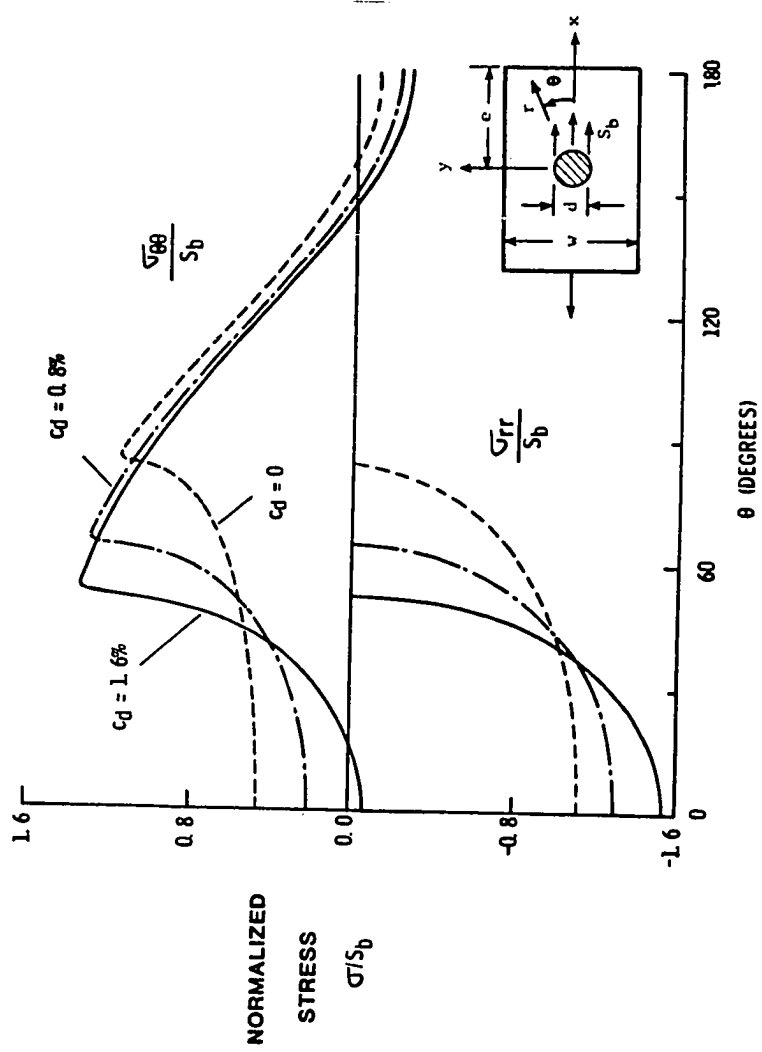
Fig. 6 Stress distributions along hole boundary.

nonlinearly with the bearing load. Prabhakaran and Naik [15] developed an experimental technique, using a specially instrumented pin, to study this nonlinear load-contact behavior in a clearance-fit joint. Naik and Crews [16] developed a stress analysis method, to account for the nonlinear load-contact behavior, in a clearance-fit joint. Development of the load-contact measurement techniques and the stress analysis method for clearance-fit joints were a part of the present research and will be dealt with extensively later.

1.3 Environmental Parameters

This group of parameters includes loading type (static or dynamic), moisture content and temperature of surrounding air. As mentioned earlier, one approach to simplify the analysis of multi-fastener joints assumes that the joint can be represented as an array of single-fastener coupons. An accurate analysis of the loading at each fastener hole is essential to this approach. In the most general case, this loading consists of a component that is reacted as a bearing load at the hole and a second component that bypasses the hole and is reacted elsewhere, as shown in Fig. 7. This combination bearing-bypass loading can strongly affect failure mode and strength at the fastener hole.

Garbo [17], Hart-Smith [12] and Ramkumar [18-20] found that, for low bearing loads in tension, laminates failed in the net-tension mode. For increasing values of bearing loads the net-tension strength of the laminate decreased linearly with the bearing stress until the failure mode switched from net-tension to bearing (Fig. 8). Unlike the net-tension strength, the bearing strength was
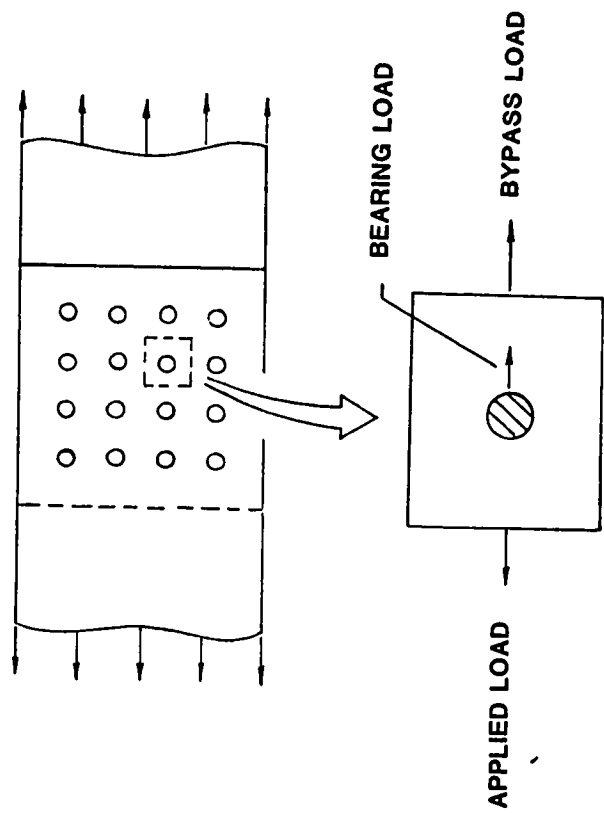
Fig. 7 Bearing-Bypass loading in a multi-fastener joint.
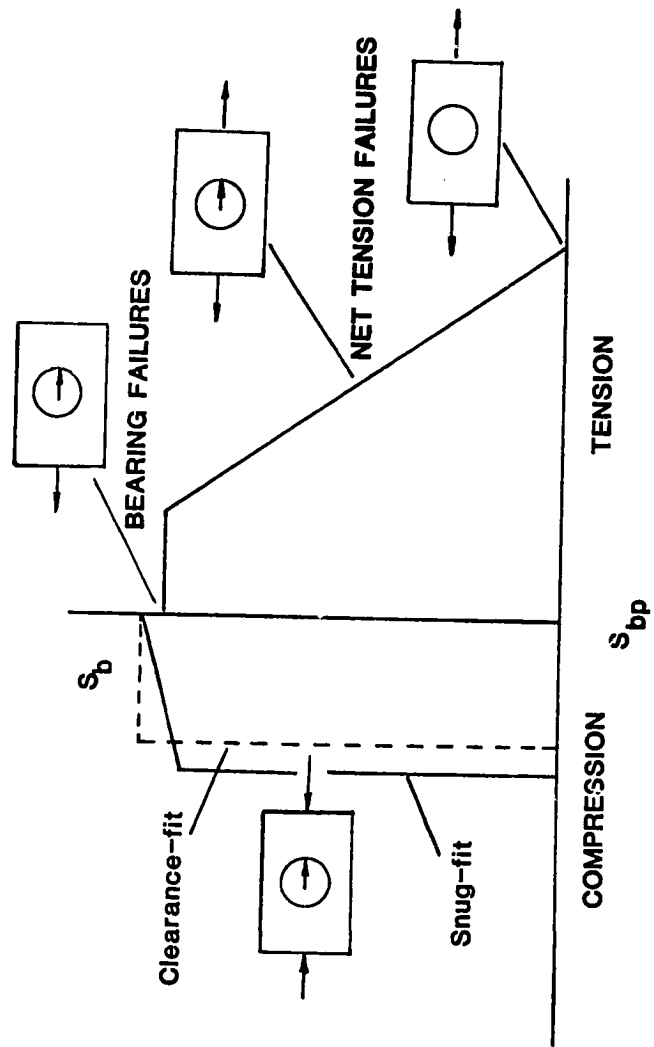
Fig. 8   Bearing-bypass strength diagram.

independent of load. For snug-fitting joints subjected to compress-
ive bearing-bypass loads, Hart-Smith [12] and Ramkumar [18-20] found
that laminate strength was unaffected for low values of bearing load
until a certain value of bearing load was reached. Beyond this value
there was a linear interaction between the laminate strength and the
bearing stress and the failure mode switched from net-section
compression to bearing (Fig. 8).

In general, very little research has been published on the
effects of compressive bearing-bypass loading on laminate strength
and failure modes. There are several apparent differences for
laminate failure under compressive bearing-bypass loading compared to
tensile bearing-bypass loading. For example, under certain loading
conditions, compressive bypass loads could cause contact on both
sides of the bolt leading to load transfer across the bolt. This
results in lower stress concentrations at the hole and thus leads to
an increase in bolt bearing strength. Furthermore, the failure modes
can interact during combined bearing and bypass loading. Bearing
failures, for example, could cause a weakening of the laminate along
the specimen width and could thereby precipitate a failure across the
width of the specimen.

The presence of a clearance between the bolt and the hole
could further complicate the problem because of the nonlinear bolt-
hole contact. In most practical applications some clearance exists
between the fastener and the hole and the region around the hole is
generally subjected to combined bearing-bypass loading. A detailed
study of the nonlinear effects of clearance and the influence of
combined bearing-bypass loading at clearance-fit fastener holes is

the focus of the present research and will be discussed extensively in later chapters.

The effects of fatigue loading at laminate fastener holes were studied by Crews [13], Ramkumar [20] and others. In general, fatigue strength was lower than static strength by about 20 percent. Environmental moisture and elevated temperature effects were beyond the scope of the present study in which tests were conducted at room temperature in laboratory air.

1.4 Strength Prediction Procedures for Loaded Holes

The early procedures used to predict laminate strength at fastener holes were based on empirical methods [11,12]. However, such methods typically require extensive joint testing and may apply only over the range of these tests. In contrast, analytical approaches use material properties to predict the joint response. The development of analytical methods requires a fundamental understanding of joint behavior. This behavior must be interpreted in terms of the joint configuration, loading, and material properties. Unfortunately, the complicated nature of fastener hole failures prevents a completely analytical approach for predicting laminate strength. As a result, various simplifying assumptions have been used to develop semi-analytical prediction procedures.

Predicting the strength for a laminate fastener hole involves two basic steps. First, the local stresses near the fastener hole must be accurately calculated. Second, the local stresses are then used in an appropriate failure criterion to predict a local failure mode and strength. A major problem associated with

the use of fibrous composites in loaded hole applications is the
selection of a suitable failure criterion both for individual laminae
and the laminate as a whole. Typically, several failure modes are
possible and a different failure criterion may be needed for each
failure mode. In general, a governing stress (or combination of
stresses) must be calculated for each failure mode and then compared
with a corresponding failure criterion to determine the strength for
each mode. The lowest such calculated strength is taken as the
strength prediction for the laminate. Note that the relative
severity of a given failure mode cannot be estimated from the
magnitude of the computed stresses alone but instead must be based on
the severity of the stresses compared to the strength for the
particular mode.

Stress analyses of laminates with loaded holes are
inherently difficult. Closed-form solutions do not exist even for
the simplest cases. Most stress analyses are based on either finite-
element or boundary-collocation methods. Typically, several
simplifying assumptions are used in such analyses. For example, many
investigators have approximated the bolt-laminate interaction by
applying a cosine distribution of bearing stress on the hole
boundary. Other researchers have assumed a snug-fit, frictionless
bolt. Figure 9 shows the stress distributions near the hole for a
quasi-isotropic laminate loaded by a smooth, rigid, snug-fitting pin
[2]. The distributions along the y-axis, the x-axis, and the
shearout plane correspond to the three failure modes for a loaded
hole. These distributions were calculated using the finite-element
analyses described in Ref. 8. Notice that multi-axial stresses exist
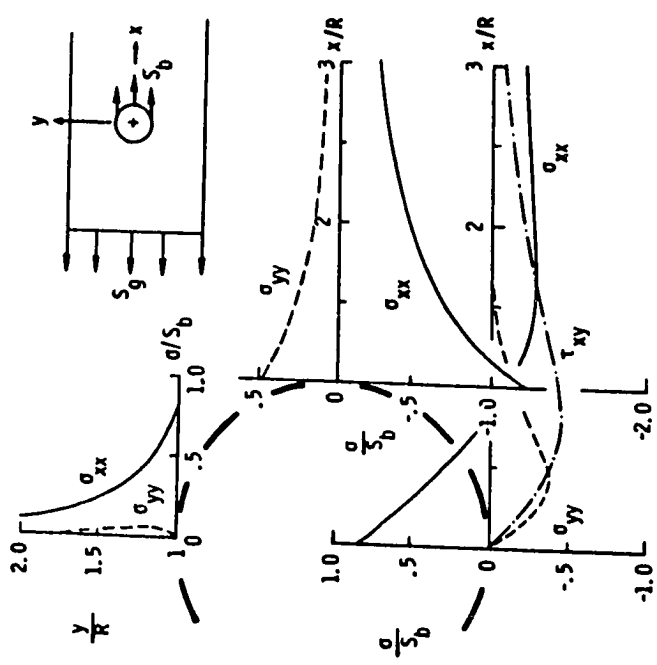
Fig. 9   Stress distributions near a loaded hole in an infinite quasi-isotropic laminate.

along each of the planes associated with the failure modes. For the x-axis and especially the shearout plane, these multi-axial stresses could influence the laminate strength.

In 1971, Waszczak and Cruse [21] presented a strength prediction procedure that used the stresses at the hole boundary and the Tsai-Hill failure criterion [22]. In terms of ply stresses, the Tsai-Hill criterion is given as follows:

$$\frac{\sigma_1^2}{X_t^2} - \frac{\sigma_1 \sigma_2}{X_t^2} + \frac{\sigma_2^2}{Y_t^2} + \frac{\tau_{12}^2}{S^2} \geq 1 \qquad (1.1)$$

The subscripts 1 and 2 indicate directions parallel and perpendicular to the ply fibers. The X_t and Y_t are the corresponding ply tensile strengths in these directions and S is the ply shear strength. They applied this procedure to each ply. When a ply was predicted to fail, it was eliminated from the analysis and ply stresses were recalculated. The bolt-bearing load was increased until the next ply failed. This procedure was continued until the last ply failed and that load was taken as the predicted laminate strength. These predictions were found to be generally conservative. Oplinger and Gandhi [23] modified the Waszczak and Cruse procedure by using the Hoffman failure criterion [24] instead of the Tsai-Hill criterion. The two-dimensional version of Hoffman's criterion is of the following form:

$$\frac{\sigma_1^2 - \sigma_1 \sigma_2}{X_t X_c} + \frac{\sigma_1(X_c - X_t)}{X_t X_c} + \frac{\sigma_2^2}{Y_t Y_c} + \frac{\sigma_2(Y_c - Y_t)}{Y_t Y_c} + \frac{\sigma_{12}^2}{S^2} \geq 1$$

(1.2)

The subscripts 1 and 2 indicate directions parallel and perpendicular to the ply fibers. The X_t and Y_t represent ply strengths in these directions; S is the ply shear strength. The subscript t indicates tension and c indicates compression. The Hoffman criterion has an advantage over the Tsai-Hill criterion because it accounts for differences in tensile and compressive strengths. Soni [25] followed the general approach used in Refs. 23 and 24 but used the Tsai-Wu criterion [26]. In terms of ply stresses and strengths, this criterion can be expressed as follows:

$$F_1 \sigma_1 + F_2 \sigma_2 + F_{11} \sigma_1^2 + F_{22} \sigma_2^2 + F_{66} \sigma_{12}^2 + 2F_{12} \sigma_1 \sigma_2 \geq 1 \qquad (1.3)$$

where,

$$F_1 = \frac{1}{X_t} - \frac{1}{X_c}$$

$$F_{11} = \frac{1}{X_t X_c}$$

$$F_2 = \frac{1}{Y_t} - \frac{1}{Y_c}$$

$$F_{22} = \frac{1}{Y_t Y_c}$$

$$F_{12} = -\frac{1}{2} \sqrt{F_{11} F_{22}}$$

and,

$$F_{66} = \frac{1}{S^2} .$$

Soni's predictions were based on hole boundary stresses and were also generally conservative. The conservative strength predictions presented in Refs. 23-25 are typical of procedures based on stresses at the hole boundary. Experimental investigations have shown that the effective stress concentrations corresponding to laminate failure are significantly smaller than the elastic stress concentration values [11,12]. A plausible explanation for this discrepancy is that a laminate develops localized damage consisting of ply splitting and/or delamination in the region of high stress and this "softened" damage zone reduces the stress concentration before the laminate fails. Strength prediction methods based on the elastic stresses at undamaged holes do not account for this effective reduction in the local stress concentration. As a result, these methods underpredict laminate strength.

In 1976 Eisenmann [27] used a linear elastic fracture mechanics approach for predicting the strength of loaded holes. He assumed eight cracks equally spaced around the hole. Failure was predicted if the stress intensity factor K_I for any crack was equal to the laminate fracture toughness K_{IC}. Although this approach produced excellent correlation with measured strengths, its broader usage requires complicated K_I solutions for cracks emnating from pin-loaded holes in orthotropic laminates.

In 1974, Whitney and Nuismer [28] introduced two versions of the so-called two-parameter approach to predict notched laminate strength. They assumed that the material near the hole is severely stressed over a small distance. They looked at the σ_{xx} stress

distribution on the net-section of a notched laminate and noted that the computed tensile stress σ_{xx} at failure was greater than the ultimate tensile strength σ_{tu} over a distance from the hole. In their first approach, this distance from the hole boundary was calculated by determining the point at which $\sigma_{xx} = \sigma_{tu}$ on the net section. This computed distance r_o was the basis for their point-stress failure criterion. A second two-parameter approach, introduced by Whitney and Nuismer [28,29], was called the average-stress criterion. This approach was based on the assumption that failure would occur when the average tensile stress over a characteristic distance d_{ot} from the hole equalled σ_{tu}.

In 1977, Agarwal [30] adopted the average-stress criterion [28] to predict the strength of laminates with loaded holes. A NASTRAN finite-element code was used to compute laminate stresses. For net-tensile failures, the tensile stress normal to several radial lines (at 22.5° intervals) were averaged over a distance of a_{ot} measured from the hole. Failure was predicted when the average stress reached the laminate tensile strength σ_{tu}. For bearing failures, compressive stresses were averaged along radial lines to obtain averages over a distance a_{oc} and failure was predicted when an average stress equalled the laminate compressive strength σ_{cu}. Similarly shearout failures were predicted by averaging the shear stress over the length a_{os} on the shearout plane (see Fig. 5(c)).

In 1981, Garbo and Ogonowski [31] used the point-stress approach together with the Tsai-Hill failure criterion [22]. Instead of looking at σ_{xx} at a distance r_o from the hole, their procedure involved looking at the Tsai-Hill parameter at intervals around the

hole to determine the failure location. Such an approach accounted for the multi-axial stress state around the loaded hole. They also used the Hoffman, Tsai-Wu, maximum stress, and maximum strain failure criteria along with the point-stress criterion [28].

In 1977, Karlak [32] modified the Whitney-Nuismer point stress criterion by introducing the concept of a variable characteristic length. He expressed r_o as a function of hole radius R and the "characteristic factor" K_o,

$$r_o = K_o \sqrt{R} \tag{1.4}$$

In 1979, Pipes, Wetherhold, and Gillespie [33] extended Karlak's modified point stress criterion by expressing r_o as:

$$r_o = (R/R_o)^m / C \tag{1.5}$$

where R_o is a reference radius, m is an exponential parameter, and C is a notch sensitivity factor. Wilson and Pipes [34] applied this modified point-stress criterion to predict shearout strength for loaded holes. Predictions were made for a range of hole sizes, w/d ratios, and e/d ratios. York, Wilson, and Pipes [35] applied a similar procedure to predict net-section failures for ranges of hole sizes and w/d values. Chang, Scott, and Springer [36] presented an even more generalized form of the point-stress approach in 1982. They assumed that failure will occur when ply stresses satisfy a given failure criterion at any point on the characteristic curve shown in Fig. 10. They expressed this curve as:
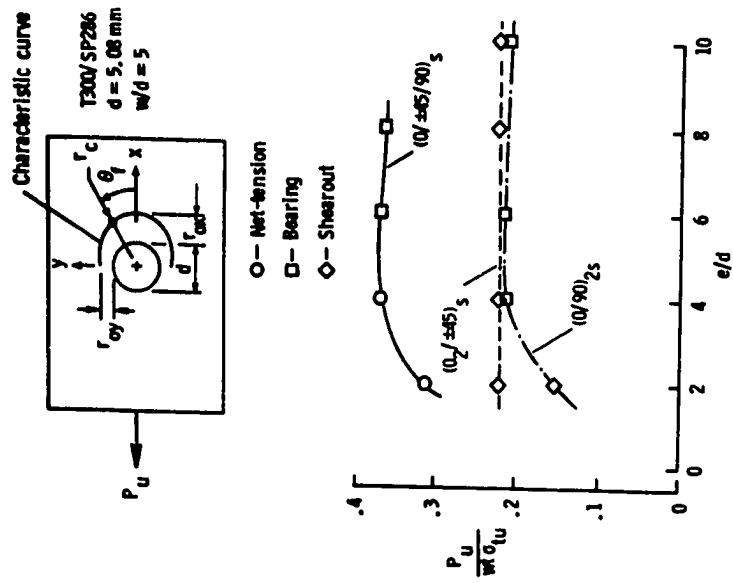
Fig. 10 Strength predictions for e/d range.

$$r_c = \frac{d}{2} + r_{oy} + (r_{ox} - r_{oy}) \cos \theta \; , \; -\pi/2 \le \theta \le \pi/2 \qquad (1.6)$$

Failure calculations were based on the Yamada-Sun [37] failure criterion:

$$(\frac{\sigma_1}{X_t})^2 + (\frac{\sigma_{12}}{S_c})^2 \ge 1 \qquad (1.7)$$

The S_c in equation (1.7) is the ply shear strength measured from a symmetric cross-ply laminate. This "in situ" shear strength is different from that measured from single plies. Laminate failure was defined by the first-ply failure and the corresponding failure mode was determined by the location θ_f on the characteristic curve. The following ranges of θ_f indicated the failure modes:

$-15° < \theta_f < 15°$ —   bearing mode

$30° < \theta_f < 60°$ —   shearout mode

$75° < \theta_f < 90°$ —   net-tension mode

Chang predicted strengths for the data presented by Agarwal [30] and by Garbo and Ogonowski [31] and compared the predictions with those in Refs. 32 and 33. Predictions based on the characteristic curve method agreed with the data within 10 percent, in most cases. On the other hand, the predictions given by the Agarwal and by the Garbo and Ogonowski methods were in error by as much as 50 percent. Figure 10 shows an example of predictions based on the characteristic curve

method. A rather complete survey of strength analysis methods for laminates with holes is provided in Ref. 2. All the works cited here are two-dimensional analyses which do not take through-thickness effects into account. Three-dimensional effects on laminate strength can be significant but, enhancing the analytical capabilities to include predictions of interlaminar failure modes and the corresponding strengths would mean the use of costlier, three-dimensional stress analyses. Also, at present, there are no generally accepted failure criteria and procedures for predicting interlaminar failure.

1.5 Research Objectives and Scope

The present work investigates the influence of clearance and combined bearing-bypass loading on laminate strength and failure modes. First, a detailed experimental and analytical study is made of the effects of bolt-hole clearance on the contact and stresses around a fastener hole. Second, an extensive analytical and experimental study is made of the effects of combined bearing-bypass loading on the contact, stresses, failure modes, failure sequences and failure strengths of laminate fastener holes.

In the present work, the effects of bolt-hole clearance on the contact and stresses around the fastener were studied experimentally by using photoelastic specimens and specially instrumented bolts. A new finite element analysis technique was developed to analyze clearance-fit fastener holes and a comparison of experimental and analytical results was made. The effects of combined bearing-bypass loading on laminate fastener holes were

examined by testing graphite/epoxy specimens. Specimens were 16-ply quasi-isotropic T300/5208 graphite/epoxy laminates and were subjected to various bearing/bypass load ratios. Radiographs, enhanced with a dye-penetrant, were used to observe local inplane damage. A finite-element analysis was conducted for each test condition to determine how the bearing/bypass loading influenced the local stresses near the fastener. The computed stresses were then used with laminate failure criteria to predict failure modes and strengths.

The stress analysis method to analyze clearance-fit fastener holes is described in Chapter 2. The experimental determination of load-contact variations and stresses is the subject of Chapter 3. The bearing/bypass test procedures and results are described in Chapter 4. Failure predictions for damage onset and ultimate failure are presented in Chapter 5. Finally, concluding remarks and further research possibilities are discussed in Chapter 6.

CHAPTER 2

STRESS ANALYSIS METHOD

To better understand the complex behavior of mechanically fastened joints, it is important to develop accurate stress analyses for bearing-loaded fastener holes. This is especially important for composite structures since they can be seriously weakened by fastener holes and often have rather complex failures modes. Further, in most joints some clearance exists between the fastener and the hole. This clearance is difficult to account for in a stress analysis because it leads to a contact region at the bolt-hole interface that increases nonlinearly with the bearing load. Closed form solutions do not exist even for the simplest cases of laminates with loaded holes. Therefore numerical techniques have been used for the analysis of laminates with loaded holes.

In the following sections, a new numerical technique is first developed for the analysis of fastener holes subjected to bearing loads only. Next, this analysis method is extended to include the effects of combined bearing and bypass loads. Finally, this technique is applied to the analysis of the more complicated cases involving dual contact.

2.1 Fastener Holes Subjected to Bearing Loads

In 1970, Harris et al [38] studied the influence of clearance in mechanically fastened joints. In their analysis of the nonlinear contact at the bolt-hole interface, they used a trial and error procedure to determine the redundant radial reactions between the plate and the fastener for a given load level. Several studies have since used numerical techniques to investigate the nonlinear contact problem associated with a smooth clearance-fit bolt under bearing loads. Oplinger and Gandhi [39] used an analytical function approach in conjunction with least squares boundary collocation. Waszczak and Cruse [21] introduced a finite element approach, but replaced the bolt with an assumed cosine stress distribution. Eshwar [40] developed a continuum analysis together with an inverse technique in which the contact angle was specified and the bearing load was calculated. Mangalgiri et al [41] also used an inverse technique but with a finite element analysis and an assumed cosine distribution of radial displacements at the bolt-hole interface.

Several studies have also been done [42-45] for the more general problem of the contact between elastic bodies including the effects of clearance. These procedures could also be used in the analysis of clearance-fit bearing-loaded holes. Francavilla and Zienkiewicz [42] used an iterative finite element formulation in terms of the contact pressures at possible contact points of the two bodies. White and Enderby [43] also used a finite element approach but with special elements at possible contact points and an iterative scheme. Sholes and Strover [44] employed an incremental piecewise-linear finite element analysis. Chan and Tuba [45] introduced an

iterative finite element procedure to include the effects of both clearance and friction. A comprehensive review of elastic analyses of pin joints has been done by Rao [46] in 1978.

More recently, Wilkinson, Rowlands, and Cook [47] used an iterative-incremental finite element scheme that accounted for friction and clearance. Kim [48] determined bolt contact angles using a combined photoelastic-finite-element method and an interactive computer graphics method. All of these analyses used either an iterative-incremental approach or made simplifying assumptions for the stresses or displacements in the contact region.

In the present study a simple numerical technique is developed for the stress analysis of a clearance-fit bolt under bearing loads. The technique uses a finite element analysis with an inverse formulation like that in reference 40. Conditions along the bolt-hole interface are specified by constraint equations. These equations describe the contact conditions more realistically than the distributions usually assumed for radial displacement or stress. Furthermore, the present technique does not need an iterative-incremental method of solution. A single-fastener clearance-fit joint was analyzed for a typical range of clearances found in aerospace applications. The finite element analysis was performed using the NASTRAN computer code. The material properties used in the analysis represented a quasi-isotropic T300/5208 graphite/epoxy laminate (see Table 1). The bolt was assumed to be rigid and the interface to be frictionless.

The nonlinear contact along the bolt-hole interface in a clearance-fit joint leads to a problem with mixed boundary conditions

Table 1   Material Properties of T300/5208 Graphite/Epoxy.

Property	Symbol	Value (Units)
Ply Properties		
Modulus in fiber direction	E_1	134.00 (GPa)
Modulus in transverse direction	E_2	11.54 (GPa)
Shear Modulus	G_{12}	6.18 (GPa)
Poisson's ratio	ν_{12}	0.38
Thickness	t_1	0.13 (mm)
Laminate Properties[a]		
Young's Modulus	E	59.45 (GPa)
Shear Modulus	G	20.40 (GPa)
Tensile strength	X_t	414.00 (MPa)
Compressive strength	X_c	455.00 (MPa)
Thickness	t	2.08 (mm)

[a]These properties represent a 16-ply, quasi-isotropic, laminate with a $[0/45/90/-45]_{2s}$ layup.

with moving boundaries. In order to determine the contact angle for a given applied load one needs to adopt an iterative-incremental method of solution. However, one could look at the "inverse" problem which states: given the angle of contact θ_c and the clearance c_d, find the correct load level. This inverse problem is simpler to deal with, because the boundary conditions are fixed and known at the outset. The correct load level can be determined by an "inverse technique" similar to that used by Eshwar [40]. An inverse technique, as discussed in the following sections, was used in the present work to solve the nonlinear contact problem.

2.1.1 Analysis Model

The configuration and loading analyzed in the present study are shown in Fig. 11. The bolt-bearing load results in a nominal bearing stress, S_b, at the hole and is reacted in tension at the left end of the model. The configuration is described by the tension length L_t, the edge distance e, the width w, and the hole diameter d. The diametrical clearance c_d between the hole and the bolt is expressed as a percentage of d. For the snug-fit joint ($c_d = 0$), the contact angle θ_c, along the bolt-hole interface, does not change with S_b and a simple linear stress analysis can be used. However, for the clearance-fit joint ($c_d > 0$), the contact angle, θ_c, increases non-linearly with S_b as shown in Fig. 12. This nonlinearly varying boundary condition at the bolt-hole interface greatly complicates the stress analysis.
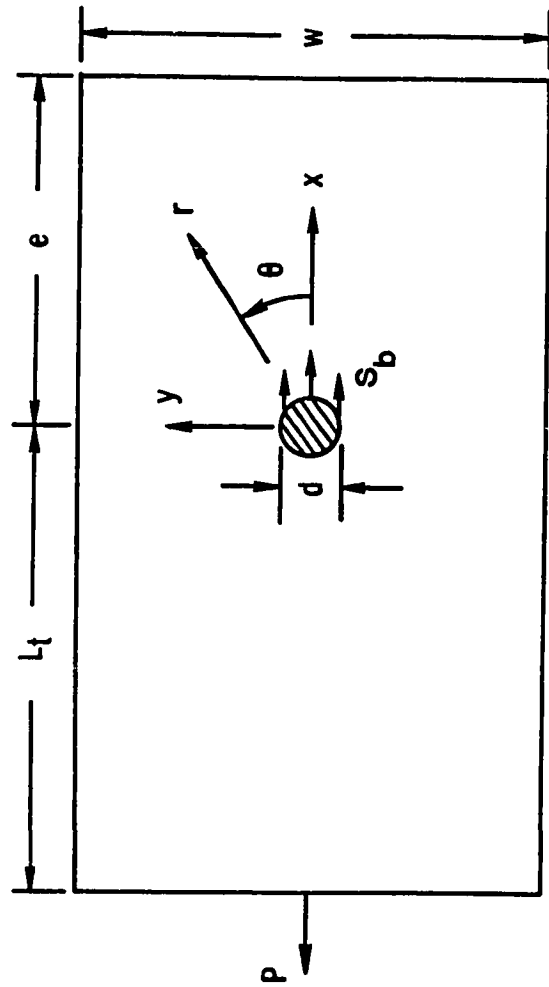
Fig. 11 Configuration and loading.
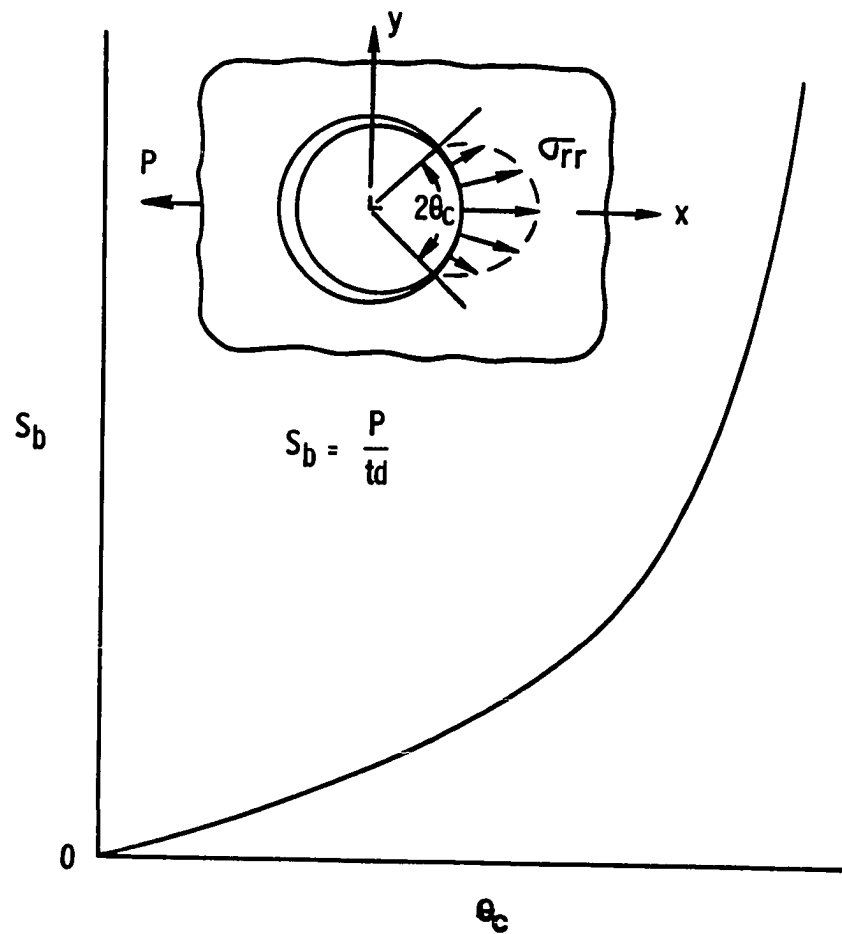
Fig. 12 Nonlinear relationship between bearing stress and contact angle.

2.1.2 Inverse Formulation

An iterative-incremental method could be used to determine the contact angle θ_c, for a given nominal bearing stress, S_b, or an inverse technique can be used to determine the nominal bearing stress, S_b, for a given contact angle, θ_c. The inverse technique is simpler to use because the boundary conditions are fixed and are known at the outset. Therefore, the inverse technique, with a finite element analysis, was used in the present work. Although the contact problem is nonlinear, the inverse technique requires only linear finite element analyses to arrive at a solution; thus, linear NASTRAN procedures were used to solve this nonlinear problem. As previously mentioned, the conditions along the bolt-hole interface were specified by displacement constraint equations. The formulation of these constraint equations and the solution procedure are described in the following two sections.

2.1.3 Displacement Constraint Equations

Figure 13 shows the analysis model, where the bolt radius, r_b is smaller than the hole radius, R, by the amount of radial clearance c. When no load is applied, the only contact point between the bolt and the hole is at point A. To simplify the analysis, the bolt is assumed to be fixed in space. The origin of the reference coordinate system is located at the center of the undeformed hole. After the model is loaded, points along the hole boundary which lie within an assumed contact arc AB have moved to the frictionless surface of the fixed rigid bolt.
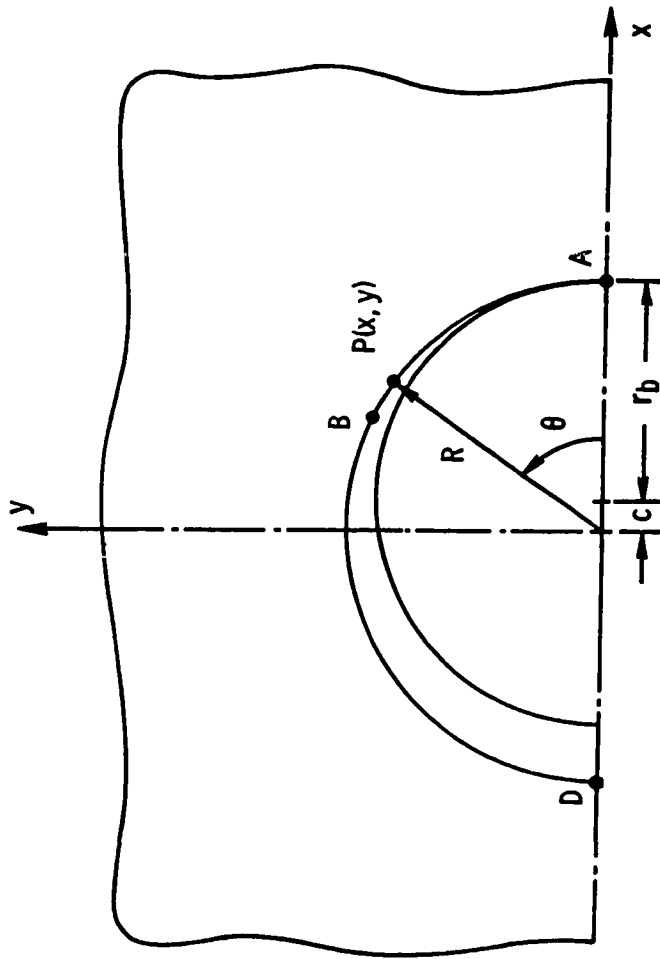
Fig. 13 Hole clearance notation.

Consider a point P(x,y) on the hole boundary within the assumed contact arc AB (see Fig. 13). Let u and v be the x- and y-displacements necessary to move point P from its original position to a point on the surface of the bolt. The deformed position of P may be described by the following equation:

$$[(x - c) + u]^2 + [y + v]^2 = r_b^2 \qquad (2.1)$$

By expressing x and y in polar coordinates and neglecting the higher order terms in u and v, equation (2.1) may be rewritten as follows:

$$Au + Bv = C \qquad (2.2)$$

where,

$$A = R \cos \theta - c \qquad (2.3)$$

$$B = R \sin \theta \qquad (2.4)$$

and,

$$C = R c (\cos \theta - 1) \qquad (2.5)$$

Equation (2.2) is a constraint equation for the u- and v-displacements of any point, P(x,y) on the contact arc AB. For any point within the assumed θ_c , the quantities A, B, and C can be computed at the outset since they are functions of the initial

geometry. In the finite element analysis, the displacements of each node within the contact region can be specified by applying equation (2.2) as a multi-point constraint. Note that the region beyond the contact arc on the hole boundary is free of radial stress. This fact will be used later in the analysis.

2.1.4 Solution Procedure

To determine the correct nominal bearing stress for the assumed contact angle, a simple procedure using a finite element analysis was established. Figure 14 shows the mesh used for the finite element analysis. One half of the plate was modeled by isoparametric elements. Nodes were placed at every 0.9375 degrees along the hole boundary. At node A, which was assumed to be in contact with the rigid bolt throughout the analysis, all degrees of freedom were set equal to zero. For an assumed contact angle, θ_c, displacements of the nodes within the contact arc were restricted to those allowed by the multi-point constraints given by equation (2.2). Thus all the boundary conditions, including those along the bolt-hole interface, are known at the outset. However, since the contact angle, θ_c, and the nominal bearing stress, S_b, are nonlinearly related, the correct S_b corresponding to the assumed θ_c is still unknown.

The correct S_b level for the assumed θ_c value was determined by a simple procedure [40]. Note that for a specified θ_c, the problem is linear and thus, the stresses in the plate are linearly related to S_b. A linear equation relating σ_{rr}, at the end of the contact arc, and S_b can be written as follows:
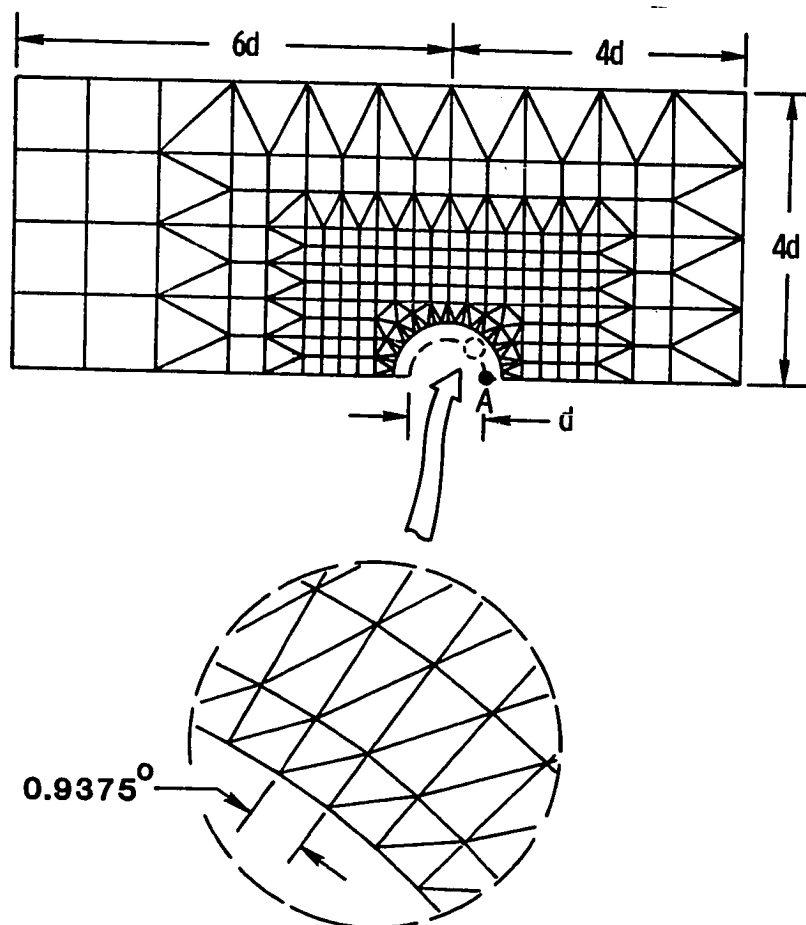
Fig. 14 Finite-element model.

$$\sigma_{rr}(R,\theta_c) = F_1 S_b + F_2 \qquad (2.6)$$

The first term in this equation represents the σ_{rr} component solely attributable to the applied bearing load. The second term represents the σ_{rr} associated with the imposed multi-point constraints. This second term is a function of clearance, as indicated by (2.2 - 2.5).

As mentioned earlier, the hole boundary region beyond the contact arc is stress free. Thus,

$$\sigma_{rr}(R,\theta) = 0, \qquad \theta_c \leq \theta \leq \pi \qquad (2.7)$$

This stress boundary condition was imposed at the end of the contact arc as,

$$\sigma_{rr}(R,\theta_c) = 0 \qquad (2.8)$$

The correct solution must satisfy equation (2.8). If S_b^* is the correct nominal bearing stress corresponding to the contact angle, θ_c, then, from equations (2.6) and (2.8), we have the following relation:

$$F_1 S_b^* + F_2 = 0 \qquad (2.9)$$

This equation can be rewritten as follows:

$$S_b^* = -F_2/F_1 \qquad (2.10)$$

Equation (2.10) was evaluated by the following procedure. For an assumed θ_c, an S_b was selected arbitrarily and the σ_{rr} was calculated at the end of the contact arc using a finite element analysis. These S_b and σ_{rr} values were then substituted into equation (2.6) to get an equation for F_1 and F_2. Next, a second S_b was selected and again the corresponding σ_{rr} at the end of the contact was calculated. This second set of S_b and σ_{rr} values was used with equation (2.6) to get a second equation for F_1 and F_2. The two equations were solved to determine F_1 and F_2 which were used in equation (2.10) to find S_b^*. This procedure was repeated for a series of θ_c values to determine the corresponding S_b^* values. These pairs of θ_c and S_b^* values were then plotted as $S_b - \theta_c$ curves for the nonlinear contact in the clearance-fit joint.

2.1.5 Results and Discussion

First, to evaluate the accuracy of the present analysis, results are compared with previously published work. Next, the effects of clearance on the contact angle, local stresses, and the hole elongation are presented. Also, the effect of different levels of the nominal bearing stress on the local stress distribution is shown.

The $S_b - \theta_c$ curve obtained for an essentially infinite plate (w = 20 d, e = 10 d, L_t = 10 d) with isotropic material properties using the NASTRAN program is shown as a solid line in Fig. 15. The dash-dot curve represents the infinite plate results obtained by Eshwar [40] using a continuum analysis. For both curves, the diametrical clearance c_d was 0.8 percent. The two curves are in
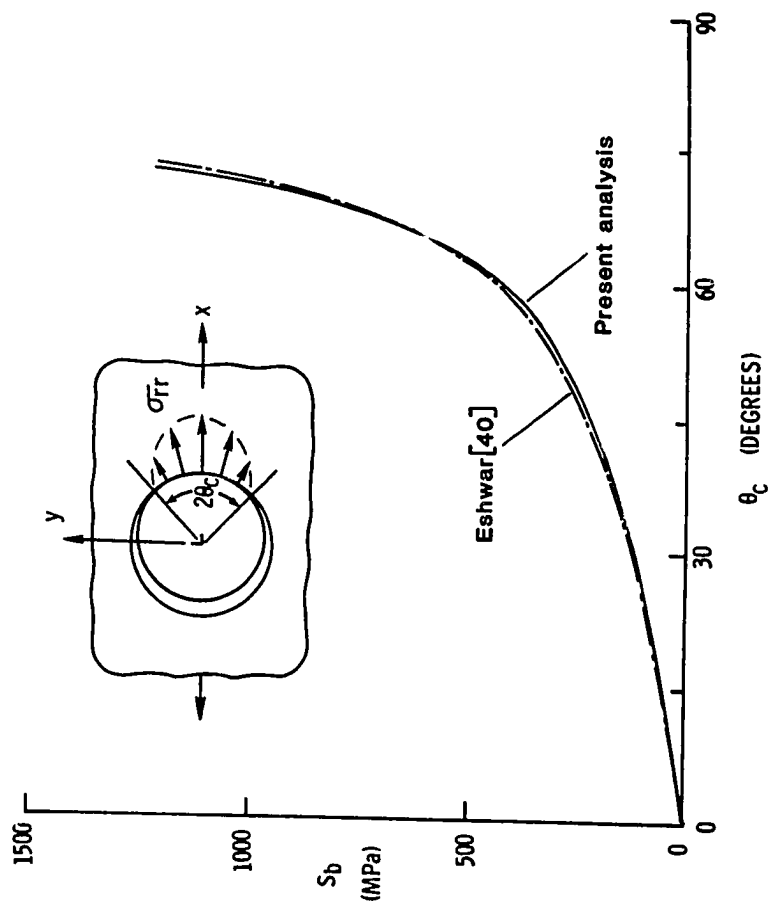
Fig. 15 Comparison of infinite plate results.

excellent agreement, which verifies the finite element model and the numerical procedure used in the present study. A comparison of the stress results for a finite plate (see Fig. 14), with c_d = 0.8% is made in Table 2. The tensile stress-concentration factor, K_{tb}, (i.e. $(\sigma_{\theta\theta})_{max}$ /S_b) and the bearing stress-concentration factor, K_{bb}, (i.e. $(\sigma_{rr})_{max}$ /S_b), obtained from the present analysis techniques, are compared with those computed using the stress analysis methods described in references 41 and 49. Reference 41 assumes a cosine distribution of radial displacements, while, reference 49 assumes a sinusoidal radial stress distribution at the bolt-hole interface.

The present analysis technique does not make any simplifying assumptions for the stresses or displacements in the contact region. Conditions along the bolt-hole interface are specified by displacement constraint equations which describe the contact conditions more realistically than the distributions usually assumed for radial displacement or stress. It is therefore believed that the results using the present procedure are more accurate than those obtained by the methods described in references 41 and 49. Further, a comparison is also made of experimental and analytical results, for load-contact curves and local stresses, in the following chapter.

Two values of the bolt-hole clearance, c_d = 0.8 percent and 1.6 percent, were used in the present study. These values are typical of clearances recommended for mechanically fastened joints in aerospace structures made of composite materials [1]. In addition, the snug-fit case (c_d = 0) was used as a reference. All of the following results were obtained for the finite size plate shown in

Table 2   Comparison of stress results.

Solution Method	K_{tb}	K_{bb}
Present	1.27	1.26
Reference 41	1.28	1.26
Reference 49	1.24	1.49
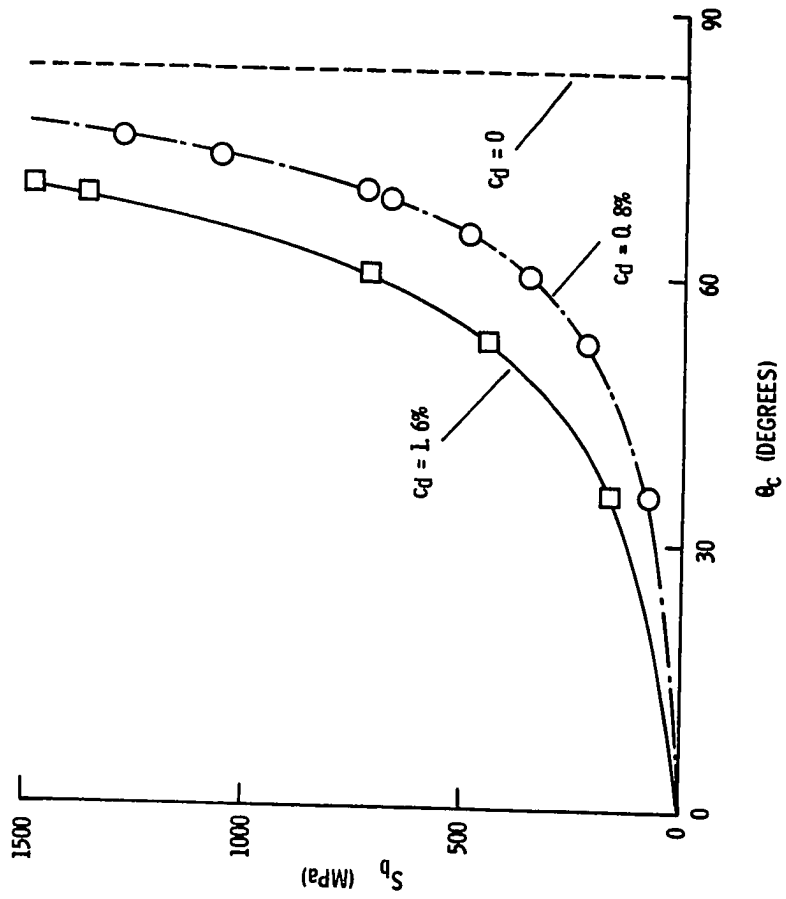
Fig. 16 Effect of clearance on the $S_b - \theta_c$ relationship.

Fig. 14 with $w = 8\ d$, $e = 4\ d$, $L_t = 6\ d$. The influence of the value c_d on the $S_b - \theta_c$ curves is shown in Fig. 16. The dashed line corresponds to the snug-fit case ($c_d = 0$). In this linear case, the contact angle; $\theta_c = 83$ degrees, does not change with increasing S_b. For both the nonlinear cases (the dashed-dot and solid curves), at low levels of S_b, the contact angle, θ_c, increased rapidly for small increases in S_b. At higher S_b levels, the contact angle was less sensitive to increases in the load level and appeared to approach an asymptotic limit. A least-squares fit to the finite element results indicated asymptotic values for θ_c of about 76 degrees for $c_d = 1.6$ percent and about 83 degrees for $c_d = 0.8$ percent. In general, the $S_b - \theta_c$ curves in Fig. 16 show that the clearance had a strong influence on the contact angle.

The normalized hole boundary stresses are shown in Fig. 17 for the different values of c_d. All the results shown in this figure were calculated for a nominal bearing stress of 475 MPa. Again the dashed curves represent the snug-fit ($c_d = 0$) reference case, where $\theta_c = 83$ degrees. For the case of $c_d = 0$, the peak value of ($\sigma_{\theta\theta}/S_b$) $= 1.16$ was reached about 2 degrees beyond the contact region. The contact angle for the case of $c_d = 0.8$ percent was 65 degrees. The peak value of $\sigma_{\theta\theta}/S_b$ here was 1.29, 11 percent higher than the snug-fit case. The contact angle for the 1.6 percent clearance case was only 53 degrees. The peak value of $\sigma_{\theta\theta}/S_b$ was 1.34, which was about 16 percent higher than the snug-fit case. Furthermore, the peak value of σ_{rr}/S_b was 36 percent higher than that for the snug-fit case. This figure shows that the peak stresses and their locations were strongly influenced by clearance.
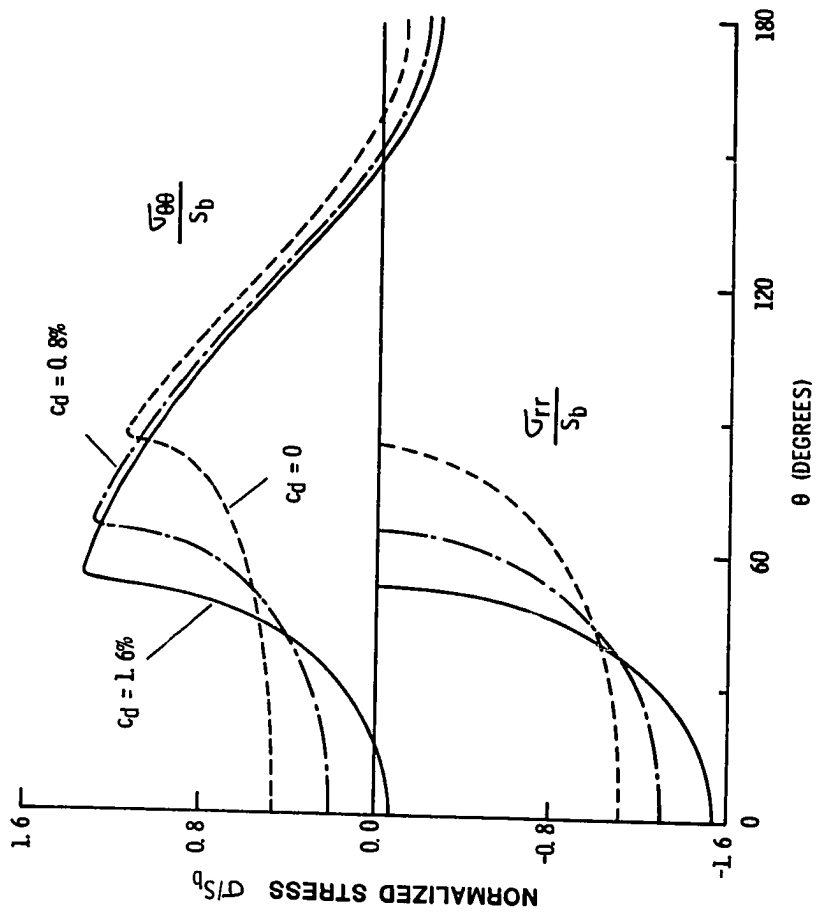
Fig. 17 Effect of clearance on local stresses.

For c_d = 0.8 percent, the radial (σ_{rr}) and tangential $(\sigma_{\theta\theta})$ stresses around the hole boundary are shown in Fig. 18 at several S_b levels. At each S_b level, the peak tangential stress occurs about 2 degrees beyond the contact region. It is important to be able to determine the location of the peak value of $\sigma_{\theta\theta}$ because the onset of damage in composite joints may start at this location [14]. Furthermore, under fatigue loading the $\sigma_{\theta\theta}$ peak will move with the cyclic load which severely complicates the fatigue damage analyses.

The variations of the peak stresses with increasing stress level S_b are shown in Figs. 19 and 20 for several values of c_d. As expected, for the linear snug-fit case $(c_d = 0)$, the peak $\sigma_{\theta\theta}$ and σ_{rr} stresses vary linearly with increasing S_b. For clearance cases, both the peak $\sigma_{\theta\theta}$ stress and the peak σ_{rr} stress show a slight initial nonlinearity, although, at higher load levels, both peak stresses increase linearly. It is interesting to note that, although the location of the peak $\sigma_{\theta\theta}$ stress changes nonlinearly with the load, the magnitude of the peak $\sigma_{\theta\theta}$ stress increases linearly after a slight initial nonlinearity.

Loading will cause the hole to elongate and the plate to deform. The hole elongation was calculated as the x-displacement of point D relative to fixed point A (see Fig. 13). The overall plate deformation was calculated as the x-displacement of the left end of the model. Figure 21 shows the change in the hole elongation and overall plate deformation with bearing stress for a 6.35 mm diameter hole. As expected for the snug-fit case, both the hole elongation and overall plate deformation vary linearly with increasing S_b. After a slight initial nonlinearlity, the hole elongation and overall plate
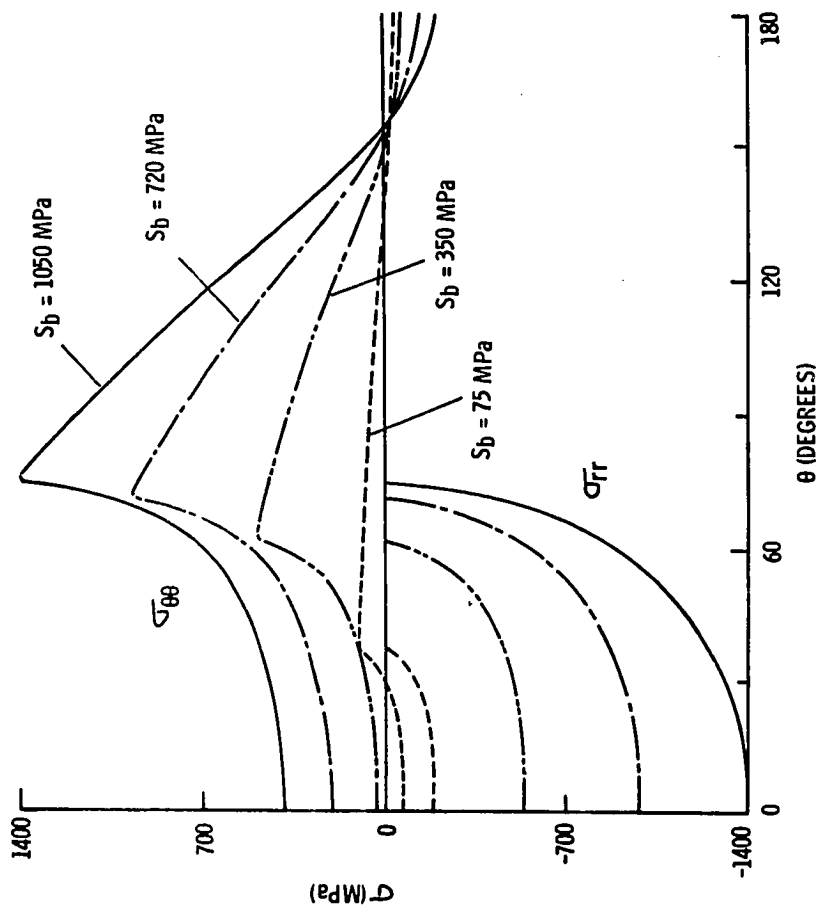
Fig. 18 Local stress distributions at different loads, c_d = 0.8 percent.
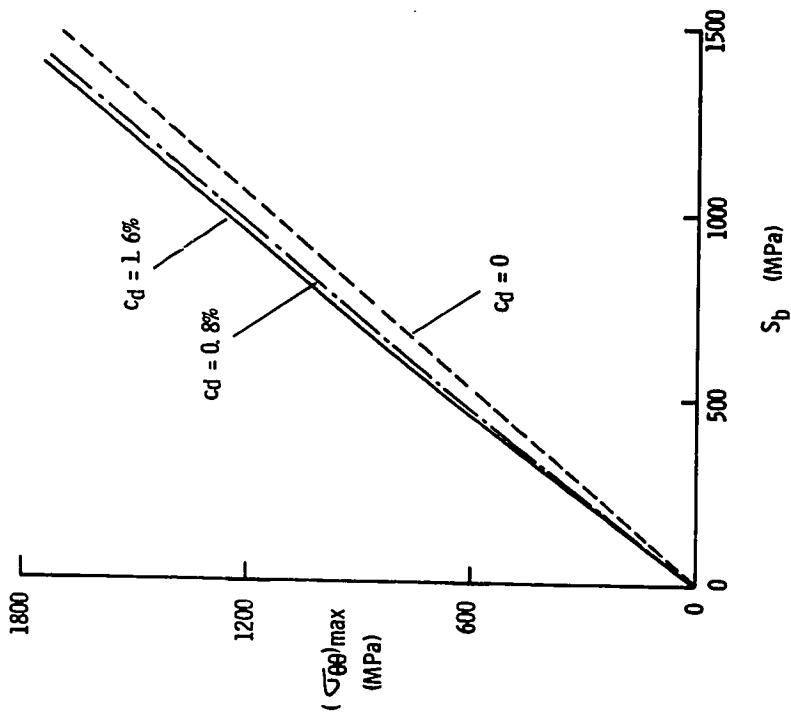
Fig. 19 Variation of peak tangential stress with S_b .
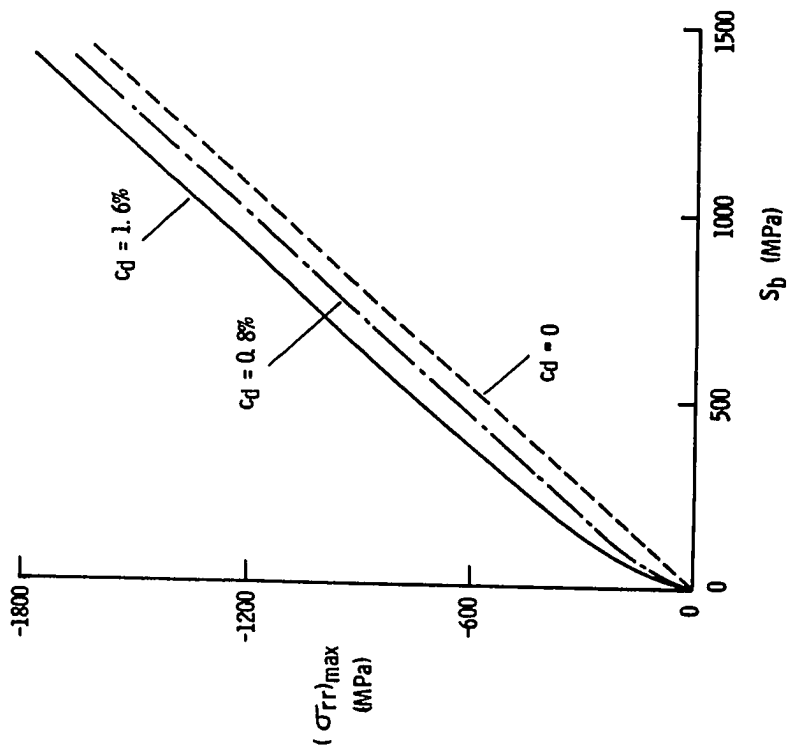
Fig. 20 Variation of peak radial stress with S_b .
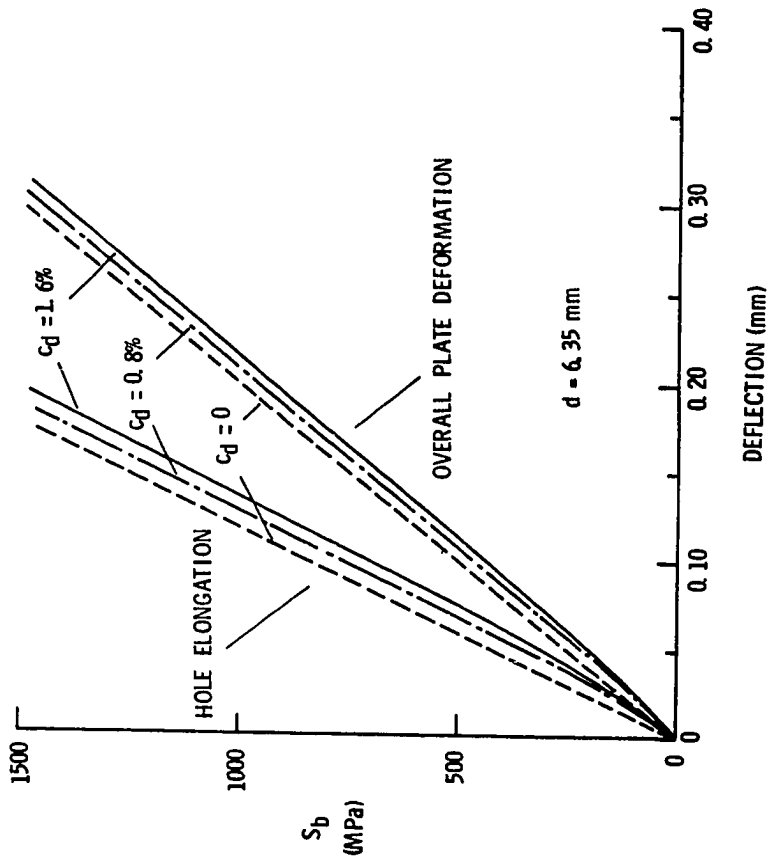
Fig. 21 Hole elongation and overall plate deformation.

deformation also vary linearly with increasing bearing stress for the clearance cases. At a typical laminate bearing strength level of $S_b =$ 1000 MPa, [14] the $c_d = 1.6\%$ case shows a 16% higher hole elongation than for the snug-fitting case. As expected, when compared to the hole elongation, the overall plate deformation is less sensitive to clearance. Also the initial nonlinearity of the overall plate deformation is less severe. For the $c_d = 1.6$ percent case, overall deformation is only 7 percent higher than the reference $c_d = 0$ case at $S_b = 1000$ MPa. The length $L_t = 6$ d used in the present study is typical of bolt spacing used in multi-fastener joints. Hence the above results for overall plate deformation suggest that clearance is probably not a critical factor in the stiffness analysis of multi-fastener joints.

2.2 Fastener Holes Subjected to Combined Bearing and Bypass Loads

The stress analysis of a multi-fastener joint can be simplified by representing it as an array of single-fastener elements. The loading at each fastener consists of a component that is reacted as a bearing load at the hole and a second component that bypasses the hole and is reacted elsewhere, as shown in Fig. 17. Single-fastener elements subjected to such combined bearing-bypass loading can be analyzed and tested in order to better understand the complex behavior of a multi-fastener joint. In general, very little research has been published on the analysis of single-fastener elements subjected to bearing-bypass loading. In 1981, Ramkumar [18] used a two-dimensional finite-element stress analysis to determine the stress state around the fastener in a single-fastener laminate

subjected to bearing-bypass loads. The fastener load was modelled by imposing zero radial displacements on the load-carrying half-segment of the fastener hole surface. In the same year, Garbo [17] used his BJSFM analysis [31] to obtain the stresses in a single-fastener laminate subjected to bearing-bypass loads. The fastener load was simulated by specifying a radial stress boundary condition varying as a cosine over half the hole.

All the stress analyses done in the past have neglected the effect of the clearance between the hole and the fastener. In almost all practical applications some clearance exists between the hole and the fastener. The presence of a clearance leads to a nonlinear contact between the hole and the bolt (see Fig. 12) and influences the stress state around the hole considerably as discussed in the previous sections. It is important to make an accurate stress analysis because strength predictions for the joint are to be made based on these computed stresses and an appropriate failure criterion.

For stress analysis purposes, the combined bearing-bypass loading could be resolved into two simpler loading cases - the un-loaded hole case and the loaded hole case (see Fig. 22). The local stresses for these two cases could then be calculated individually using finite-element methods and then superposed to approximate the desired local stresses for a given combination of bearing-bypass loading. In a clearance-fit joint, however, this would involve the superposition of a nonlinear contact problem (the loaded hole case) and a linear open hole problem. In general, such a superposition will not adequately model the nonlinear contact between the bolt and

(a) Unloaded hole case.

(b) Loaded-hole case.

(c) Combined bearing and bypass case.
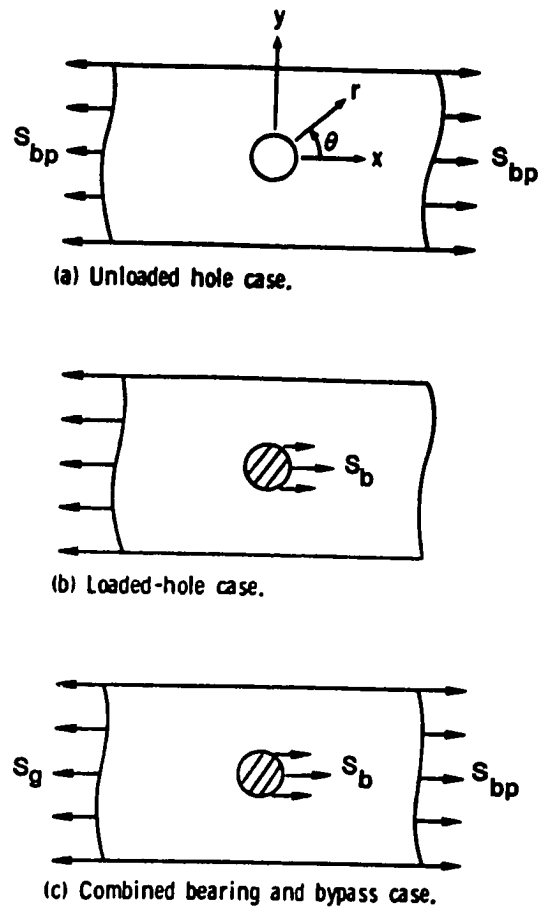
Fig. 22 Basic loading cases for single-fastener coupons.

the hole for combined bearing-bypass loading. It was therefore decided to use a direct solution approach without superposition. An inverse technique, as described in Sections 2.1.2 - 2.1.4 is used in the solution of this nonlinear problem.

It is customary to specify the bearing-bypass ratio, $\beta = S_b/S_{np}$, where S_{np} is the nominal net-section bypass stress, in order to describe the bearing-bypass loading. In the present analysis the applied nominal gross stress, S_g , and the applied nominal bypass stress, S_{bp} , appear explicitly in the equations and so it was more convenient to use the bypass ratio, $k = S_{bp}/S_g$, to describe the bearing-bypass loading.

As indicated in Fig. 12, the contact angle between the bolt and the hole varies nonlinearly with the load. In order to determine the contact angle for a given load level, one needs to determine the nonlinear variation of the contact angle with load. For a given configuration, this nonlinear relation between the contact angle and the load is different for different values of bearing-bypass ratio β and for different values of clearance c_d between the bolt and the hole. Thus, before a stress analysis can be performed for a given joint configuration, at a given load level, S_g , and a given bearing-bypass ratio, β, one needs to determine the nonlinear relation between the contact angle and the load for the given conditions.

The objective of the following sections is to develop a procedure to determine this nonlinear relationship between the applied load and the contact angle for a given clearance and any given bearing-bypass load ratio. A description of the analysis model is followed by a discussion of the inverse technique used. A

solution method is then developed for bearing-bypass loads. Finally an example is used to demonstrate the use of the suggested solution procedure.

2.2.1 Analysis Model

The configuration and loading analyzed in the present study are shown in Fig. 23. The gross applied load P_g is reacted partly in bearing, P_b, and partly as a bypass load, P_{bp}, at the other end of the model. The bolt was assumed to be rigid and the bolt-hole interface to be frictionless. The diametrical clearance c_d between the hole and the bolt was expressed as a percentage of the hole diameter d. The material properties used in the analysis represented a quasi-isotropic T300/5208 graphite/epoxy laminate (see Table 1). The mesh used for the finite element analysis was similar to that shown in Fig. 14. As described in Section 2.1.4, nodes were placed at every 0.9375 degrees along the hole boundary. At node A, (see Fig. 13) which was assumed to be in contact with the rigid bolt throughout the analysis, all degrees of freedom were set equal to zero. An inverse technique was used to determine the nominal gross stress S_g for an assumed contact angle θ_c. Conditions along the bolt-hole interface and within an assumed contact angle, θ_c, were specified by multi-point constraints as described in Section 2.1.3. However, since the contact angle, θ_c, and the nominal gross stress, S_g, are nonlinearly related, the correct S_g corresponding to an assumed θ_c (for a given clearance c_d and bypass ratio k) is still unknown. The correct S_g level for an assumed θ_c value was determined by the procedure described in the following section.
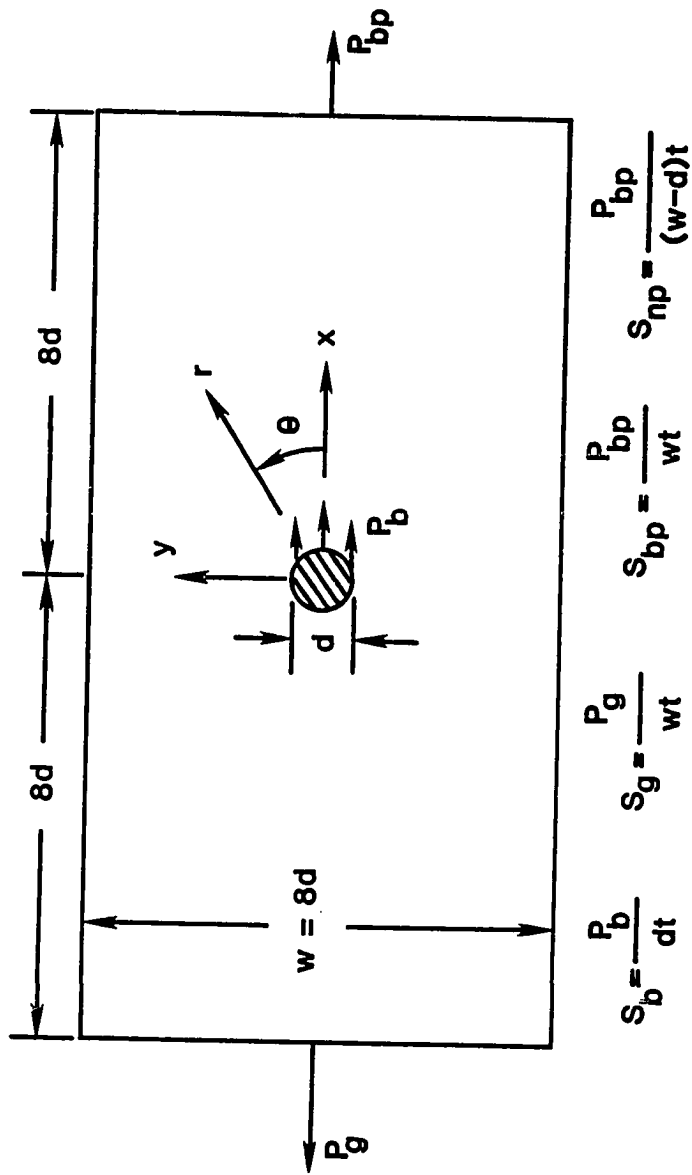
Fig. 23 Configuration and loading for combined bearing bypass loading.

$$S_b = \frac{P_b}{dt}$$

$$S_g = \frac{P_g}{wt}$$

$$S_{bp} = \frac{P_{bp}}{wt}$$

$$S_{np} = \frac{P_{bp}}{(w-d)t}$$

2.2.2 Solution Method for Bearing-Bypass Loads

The correct S_g level for an assumed θ_c value was determined by a simple procedure. Note that for a specified θ_c, the problem is linear and thus, the stresses in the plate are linearly related to the applied load S_g, the bypass load S_{bp}, and the forces associated with the imposed multi-point constraints. A linear equation relating σ_{rr} at the end of the contact arc, S_g and S_{bp} can be written as:

$$\sigma_{rr}(R,\theta_c) = A_1 S_g + B_1 S_{bp} + C_1 \qquad (2.11)$$

The first two terms in this equation represent the σ_{rr} components attributable to the applied load S_g and the bypass load S_{bp} respectively. The third term represents the σ_{rr} associated with the multi-point constraints. Only three different finite element solutions, as described in Section 2.1.4, for any three different combinations of S_g and S_{bp}, are needed to determine the constants A_1, B_1, and C_1 in equation (2.11). As mentioned earlier, (Section 2.1.4) the correct solution for a given contact angle θ_c must satisfy the condition $\sigma_{rr}(R,\theta_c) = 0$. Therefore, for every correct solution we have,

$$A_1 S_g + B_1 S_{bp} + C_1 = 0 \qquad (2.12)$$

Equation (2.12) represents a linear relationship between S_g and S_{bp}. This means that for a given contact angle θ_c, the correct solutions for different combinations of S_g and S_{bp}, will lie on the same straight line given by equation (2.12). This straight line

represents a family of solutions over a range of (S_{bp}/S_g) ratios for a given contact angle θ_c.

A different contact angle θ_d will lead to a straight line of a different slope in the $S_g - S_{bp}$ plot (see Fig. 24). A family of straight lines can be generated for a range of contact angles. Similar plots can be made in the $S_b - S_{bp}$ plane where S_b is the nominal bearing stress (see Fig. 25).

In order to obtain the nonlinear relation between S_g and contact angle θ_c for a given bypass ratio k, one needs to construct a straight line of slope k in the $S_g - S_{bp}$ plot (Fig. 24). The values of S_g and θ_c, at which the straight line of slope k intersects the straight lines of constant contact angle, can then be plotted on a $S_g - \theta_c$ plot to give the required nonlinear relation (see Fig. 26).

The above formulation for combined bearing-bypass loading can be applied to cases involving either tension bearing-bypass or compression bearing-bypass. Note that equation (2.11) is satisfied regardless of the signs of S_g and S_{bp}. However, as discussed later in Section 2.2.5, the above procedure cannot be used for cases of dual contact under compression bearing-bypass loads. An example that illustrates the above procedure is described in the following section.

2.2.3 Illustrative Example

Consider a quasi-isotropic T300/5208 graphite/epoxy laminate subjected to combined bearing-bypass loading. For a clearance of $c_d = 0.8\%$ it is required to determine the stresses
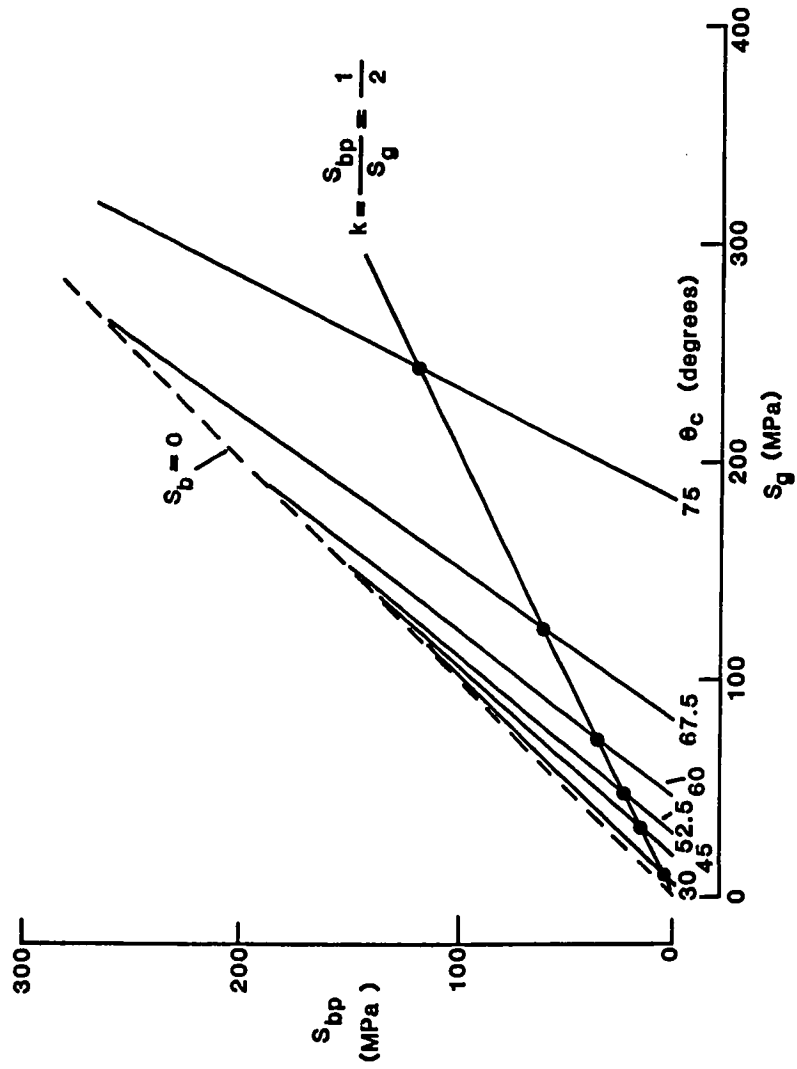
Fig. 24 Linear relation between S_g and S_{bp} for constant θ_c.
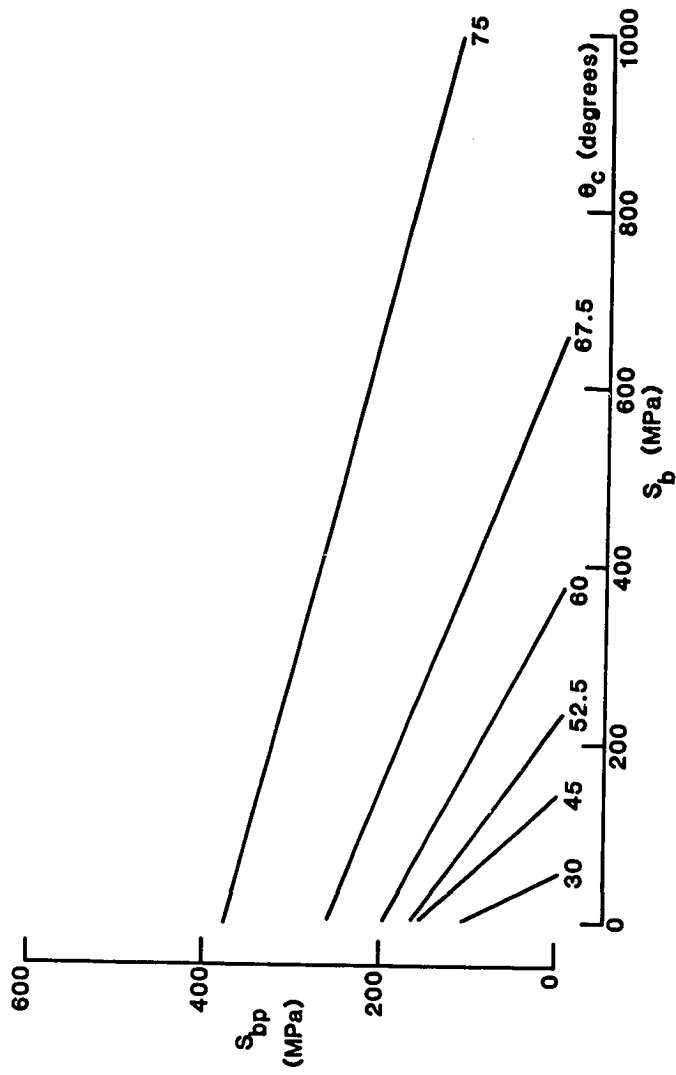
Fig. 25 Linear relationship between S_b and S_{bp} for constant θ_c.
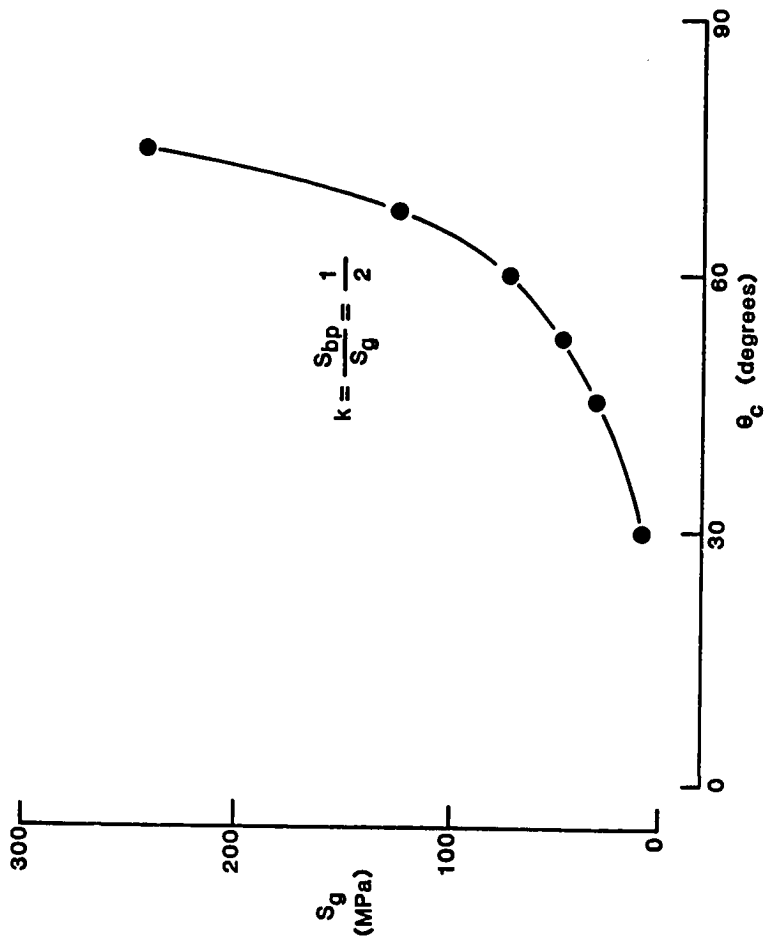
Fig. 26 Nonlinear relationship between S_g and θ_c for bypass ratio of 1/2 .

around the hole at a load level of S_g = 150 MPa and a bypass ratio, $k = (S_{bp}/ S_g)$ of 0.5.

Before the stress analysis can be done using the finite-element method one needs to determine the contact angle θ_c that corresponds to a load level of 150 MPa and a bypass ratio of 0.5. In order to determine this contact angle θ_c one needs to determine the nonlinear relation between S_g and θ_c for the given conditions. This can be done by constructing a straight line of slope k in the S_g - S_{bp} plot (Fig. 24). The values of S_g at which this straight line intersects the straight lines of constant contact angle are then plotted on a S_g - θ_c plot to give the required nonlinear relation (see Fig. 26). For a stress level of 150 MPa the corresponding contact angle can now be read off from Fig. 26 as 69.5 degrees.

Finally a finite-element analysis can be done with an applied load of S_g = 150 MPa, a bypass load of S_{bp} = 75 MPa, and a contact angle of θ_c = 69.5 degrees to obtain the required stresses around the hole.

2.2.4 Effects of Bearing-Bypass Ratio

The bearing-bypass ratio, $\beta = S_b / S_{np}$, was found to have a considerable effect on the load-contact behavior (see Fig. 27), the hole elongation, and the stresses around the hole. The values of β that were used in the present study were $\beta = \pm 0, \pm 1, \pm 3, \pm \infty$. Note that a $\beta = -\infty$ corresponds to a compression bearing case with no bypass load and a $\beta = 0$ corresponds to a tension bypass case with $S_g = S_{bp}$ and $S_b = 0$. All of the following results were obtained for the finite size plate shown in Fig. 23 with a bolt-hole clearance of
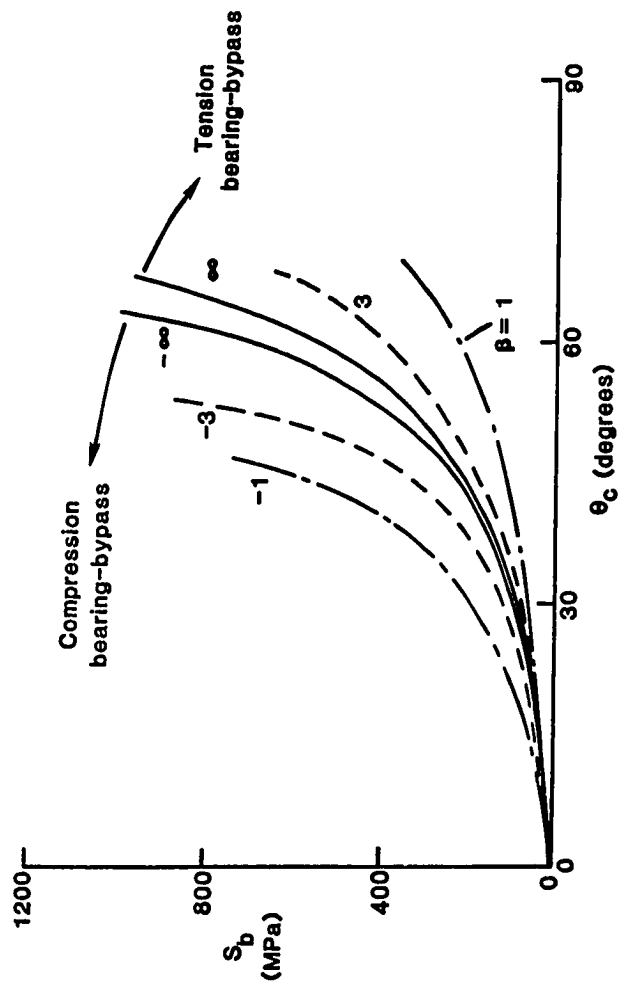
Fig. 27 Effect of bearing-bypass ratio on the S_b - θ_c relationships.

$c_d = 1.2\%$. The influence of the value of β on the $S_b - \theta_c$ curves is shown in Fig. 27. For the tension bearing-bypass cases an increase in β lead to a decrease in contact angle for the same S_b level. The opposite was true for the compression bearing-bypass cases in which an increase in β lead to an increase in θ_c for the same S_b level.

The hole elongation δ was calculated as the x-displacement of point D relative to fixed point A (see Fig. 13). If the point D moved towards the point A in the positive x-direction, then the hole elongation δ was taken as positive. Figure 28 shows the change in hole elongation with S_{np} for a 6.35 mm diameter hole. After a slight initial nonlinearity, the hole elongation varies linearly with increasing S_{np} for all three compression bearing-bypass cases. For the $\beta = -3$ case, δ is negative; i.e. the point D moves away from the point A and the hole elongates (in the x-direction) with increasing load. The opposite is true for the $\beta = -1$ and $\beta = -0.5$ cases where δ is positive and the point D moves towards point A. Thus with increasing load, the point D will make contact with the bolt and lead to a dual contact situation. Any further increase in load will then lead to contact regions on both sides of the bolt. This dual contact problem is more complicated than the single-sided contact problems dealt with in Section 2.2.2. The solution method developed in Section 2.2.2 for bearing-bypass loads and single-sided contact cannot be used for dual contact problems. A new technique for the analysis of dual contact in a clearance-fit joint under bearing-bypass loads is described in the following section.
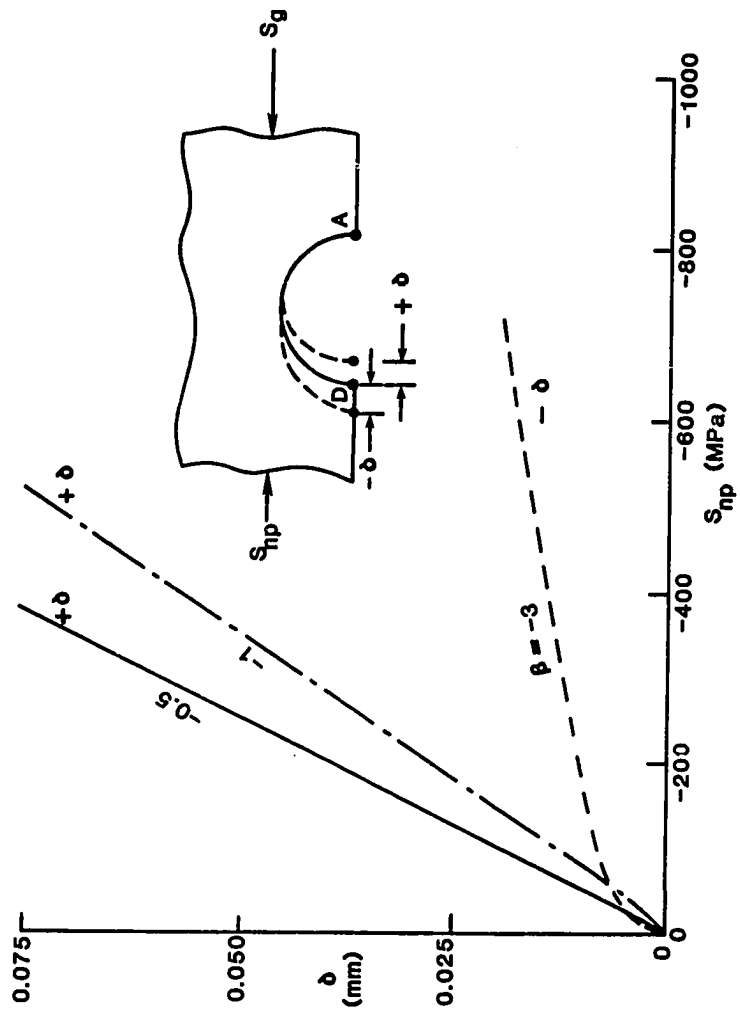
Fig. 28 Variation of hole elongation for different bearing-bypass ratios.

2.3 Analysis Method for Dual Contact Problems

As described earlier in Section 2.2.5, a clearance-fit joint subjected to compression bearing-bypass loads may lead to dual contact at the bolt. The presence of a clearance between the bolt and the hole further complicates the problem as it leads to two nonlinearly increasing contact regions around the hole. An extensive survey of the literature revealed that an analysis method for this problem had not been developed before. In the present study a simple numerical technique was developed using a finite element analysis and an inverse formualtion.

2.3.1 Analysis Model

The configuration and loading analyzed in the present study are shown in Fig. 29. The gross applied compressive load P_g is reacted partly in bearing, P_b, and partly as a compressive bypass load, P_{bp}. The bolt was assumed to be rigid and the bolt-hole interface to be frictionless. A diametrical clearance $c_d = 1.2\%$ was used in the analysis. The material properties used represented a quasi-isotropic T300/5208 graphite epoxy laminate (see Table 1). The mesh used for the finite element analysis was similar to that shown in Fig. 14. As described in Section 2.1.4, nodes were placed at every 0.9375 degrees along the hole boundary. When no load is applied, the only contact point between the bolt and the hole is at point A (see Fig. 30). To simplify the analysis, the bolt is assumed to be fixed in space. The origin of the reference coordinate system is located at the center of the undeformed hole. As compressive bearing-bypass load is applied, contact starts increasing around
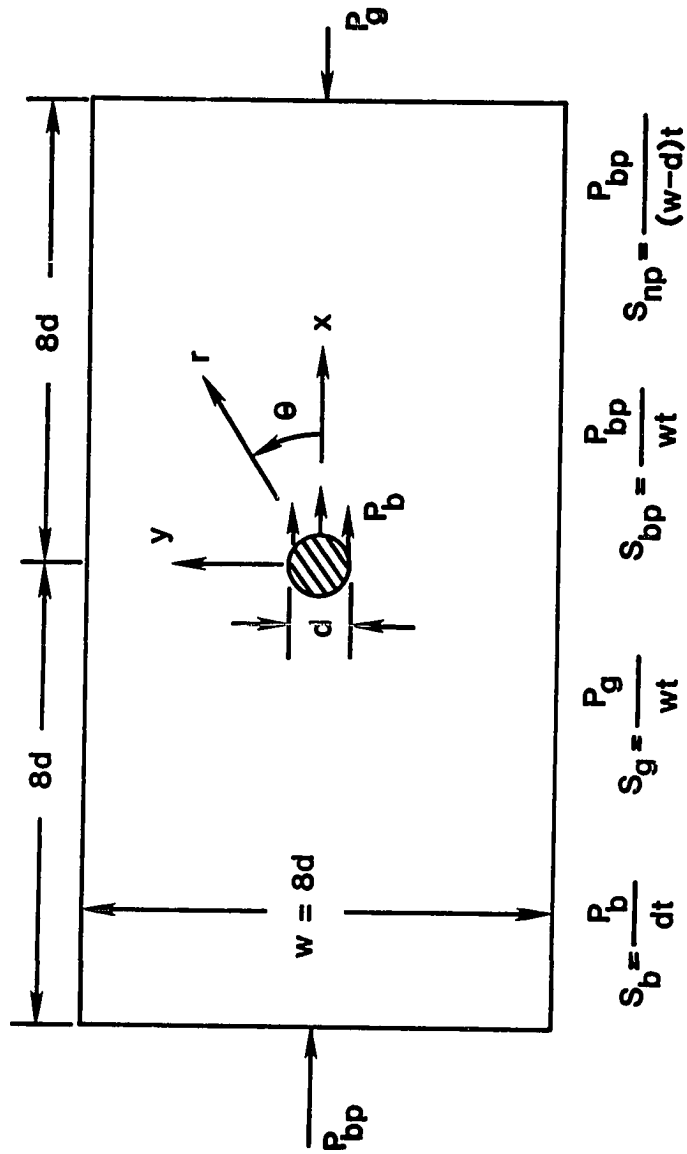
Fig. 29 Configuration and loading for compression bearing-bypass loading.

$$S_b = \frac{P_b}{dt} \qquad S_g = \frac{P_g}{wt} \qquad S_{bp} = \frac{P_{bp}}{wt} \qquad S_{np} = \frac{P_{bp}}{(w-d)t}$$
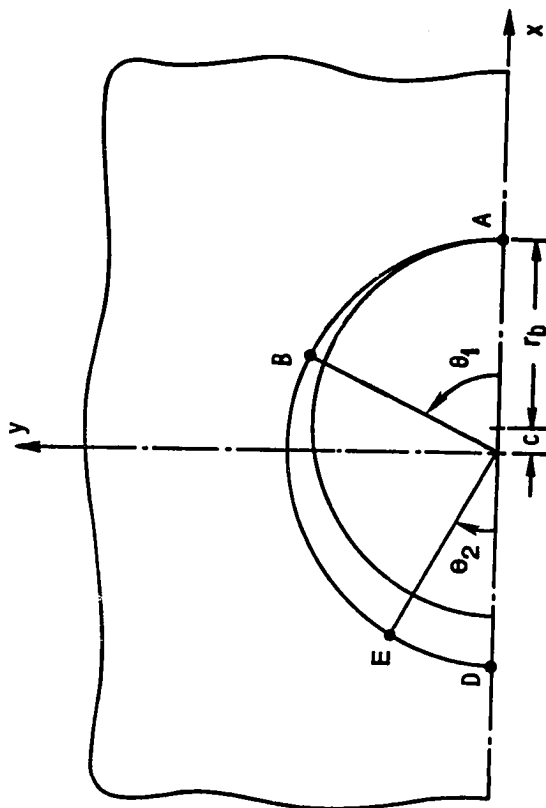
Fig. 30 Contact angle notation for dual contact.

point A. At the same time the point D moves inwards (for certain values of β) towards the frictionless surface of the fixed rigid bolt. The solution method described in Section 2.2.2 can be adopted only until there is single-sided contact around point A and the point D has not made contact with the bolt. For $\beta = -0.5$, a hole diameter of 6.35 mm, and a clearance of 0.076 mm ($c_d = 1.2\%$), the analysis in Section 2.2.2 predicts that point D will contact the bolt at a load level of $S_{np} = 375$ MPa (see Fig. 26). The analysis for dual contact should then be used for any further increments in load. As the load is increased further a dual contact situation prevails. At a certain load, there may be contact along arc AB (see Fig. 30) and also contact along arc DE leading to contact angles θ_1 and θ_2 respectively.

An iterative-incremental analysis method could be used to determine the unknown contact angles θ_1 and θ_2 for a given load level. However, such an analysis would not be cost effective and would require tedious node tracking along the contact arcs. In the present method an inverse technique is used in which contact angles θ_1 and θ_2 are both assumed and the corresponding load levels determined by a simple procedure. The inverse technique is simpler to use because the boundary conditions are fixed and are known at the outset. Conditions along the bolt-hole interface, and within the assumed contact angles θ_1 and θ_2, were specified by multi-point constraints as described in Section 2.1.3. The corresponding load levels S_g and S_{bp} were determined by the procedure described in the following section.

2.3.2 Solution Procedure

The correct S_g and S_{bp} levels for the assumed contact angles θ_1 and θ_2 were determined by a simple procedure. Note that for specified θ_1 and θ_2 the problem is linear and thus the stresses in the plate are linearly related to the applied load S_g, the bypass load S_{bp}, and the forces associated with the imposed multi-point constraints. A linear equation relating σ_{rr}, S_g, and S_{bp} can be written at the end of each contact arc as:

$$\sigma_{rr}(R,\theta_1) = A\, S_g + B\, S_{bp} + C \qquad (2.13)$$

$$\sigma_{rr}(R,\theta_2') = D\, S_g + E\, S_{bp} + F \qquad (2.14)$$

where, $\theta_2' = 180° - \theta_2$

The first two terms in these equations represent the σ_{rr} components attributable to the applied load S_g and the bypass load S_{bp} respectively. The third term represents the σ_{rr} associated with the imposed multi-point constraints. Only three different finite element solutions (see Section 2.2.2) for any three different combinations of S_g and S_{bp} are needed to determine the constants A, B, C, D, E and F in equations (2.13) and (2.14). As mentioned earlier (Section 2.1.4), the correct solution must satisfy the conditions: (i) $\sigma_{rr}(R, \theta_1) = 0$ and (ii) $\sigma_{rr}(R, \theta_2') = 0$. From equations (2.13) and (2.14) we have,

$$A\, S_g + B\, S_{bp} + C = 0 \qquad (2.15)$$

and,

$$D\ S_g + E\ S_{bp} + F = 0 \qquad\qquad (2.16)$$

The only unknowns in the above equations are S_g and S_{bp} and can be determined by the simultaneous solution of equations (2.15) and (2.16). The above procedure can be repeated for different sets of assumed contact angles θ_1 and θ_2 to generate an array of solutions as shown in Fig. 31. Each solid circular symbol represents a solution corresponding to the assumed contact angles θ_1 and θ_2. The dashed curve represents the onset of dual contact. In the region to the left of this curve there was contact only on one side of the bolt. The solution procedure developed in Section 2.2.2 may be used in this region. The solid straight lines in this region represent solution lines simliar to those in Fig. 25. The region to the right of the dashed curve represents the dual contact solutions. Unlike the single contact region, lines of constant θ_1 and constant θ_2 are not linear in this region. The dashed-dot line represents the $\beta = -0.5$ bearing-bypass ratio. It intersects the dual-contact onset curve (dashed curve) at $S_{np} = 375$ MPa. Thus dual contact for this case would begin at $S_{np} = 375$ MPa. The effect of dual contact on the $S_b - \theta_c$ curve is shown in Fig. 32. This curve was constructed from Fig. 31 by picking out the S_b, θ_1 and θ_2 values on the $\beta = -0.5$ line. Some interpolation was needed in the dual contact region. The $S_b - \theta_1$ curve in the single contact region was generated by the procedure described in Section 2.2.2. The $S_b - \theta_1$ relationship changes after the onset of dual contact. The $S_b - \theta_2$ curve is also nonlinear and
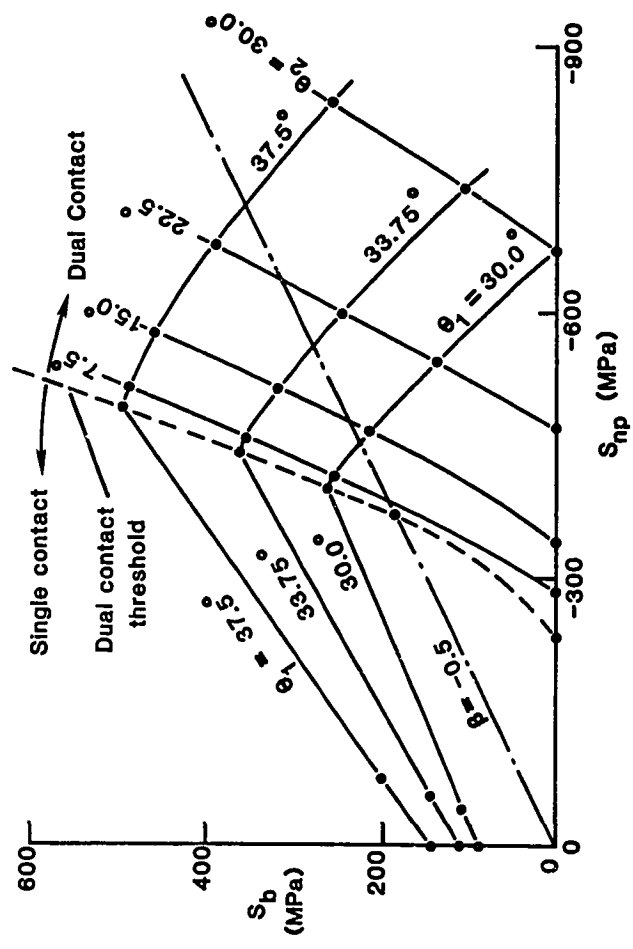
Fig. 31 Solution array for dual contact.
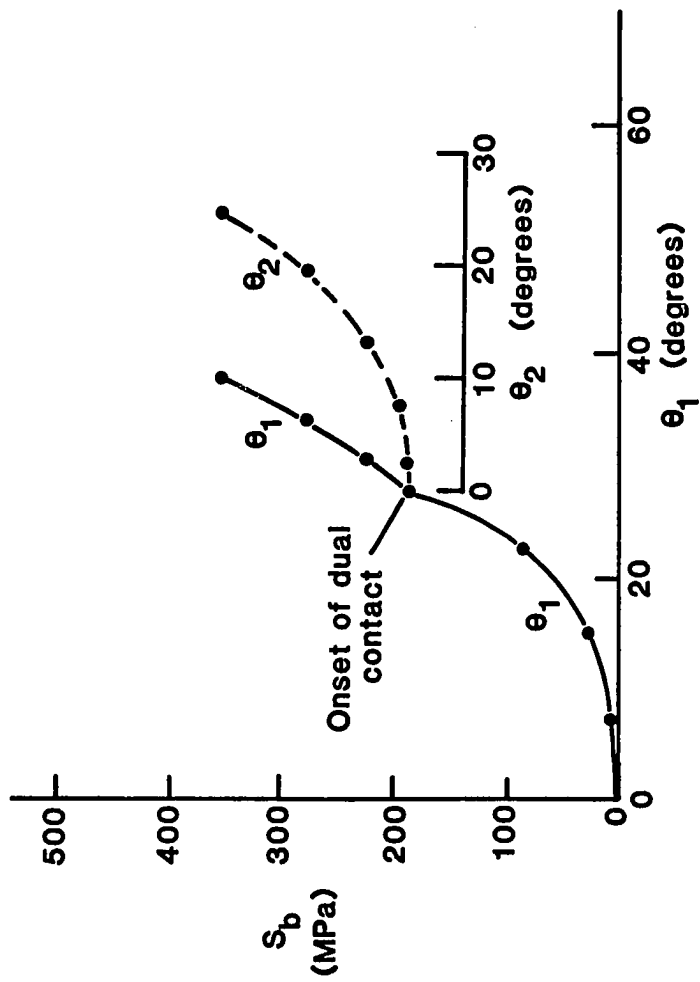
Fig. 32 Effect of dual contact on the $S_b - \theta$ relationship.

θ_2 increases more rapidly than θ_1 with increasing load. The effects of combined bearing-bypass loading and dual contact on the local stresses around the hole will be discussed in Chapter 5.

CHAPTER 3

EXPERIMENTAL TECHNIQUES

A new stress analysis method for the analysis of clearance-fit bolted joints was developed in the previous chapter. Before applying this method along with composite failure theories to predict the strength of bolted joints, it was considered appropriate to verify the finite element predictions for the load-contact variations and the stress distributions. The absence of friction in the finite element analysis in particular, required justification. In the present chapter, simple experimental techniques, using instrumented pins, are developed for the measurement of the load-contact variation in a clearance-fit, pin-loaded hole. The ability to accurately determine the arc of contact at any load was crucial for this measurement. An instrumented pin, that activated a make-or-break electrical circuit in the pin-hole contact region, was used to measure contact angles. Because of the limitations of this method another technique using an optical fiber sensing system was also developed and applied to this problem. A layout fluid technique was used for measuring contact angles in small diameter bearing loaded holes. Load-contact variations in photoelastic specimens were measured by observing the isochromatic fringe patterns around the bolt-hole interface. All such experimental load-contact variations were compared with analytical results obtained by the procedures described in Chapter 2.

Finally, photoelastic results for stresses around the hole are also compared with analytical results.

3.1 Electrical Instrumented Pin Technique

This technique was used to measure load-contact variations in a graphite/epoxy specimen. The good electrical conductivity of graphite/epoxy was the basis for this technique. An instrumented pin, that activated a make or break electrical circuit in the pin-hole contact region, was a key component in the measuring system.

3.1.1 Instrumented Pin

The instrumented pin was made of steel and consisted of two parts, (i) an inner rotating shaft and (ii) an outer slotted ring, as shown in Fig. 33. The inner rotating shaft contained a 1.6 mm diametrical hole that met a larger axially drilled hole, forming an L-shaped passage. An insulated wire was passed through this L-shaped passage. The wire could be fixed in the desired location by means of a set screw as shown in Fig. 33. The outer ring consisted of a 1.6 mm wide slot over half of its circumference. The inner rotating shaft was placed on bearings that fitted inside the outer slotted ring. The assembled instrumented pin is shown in Fig. 34. In the assembled pin, the insulated wire passes through the L-shaped passage in the inner rotating shaft and projects through the slot in the outer ring (Fig. 34). The inner shaft, along with the insulated wire, is free to rotate when the pin is under load. In order to measure the angle of rotation of the inner shaft, dowel pins were located on one face of the inner shaft and the outer ring (Fig. 33).
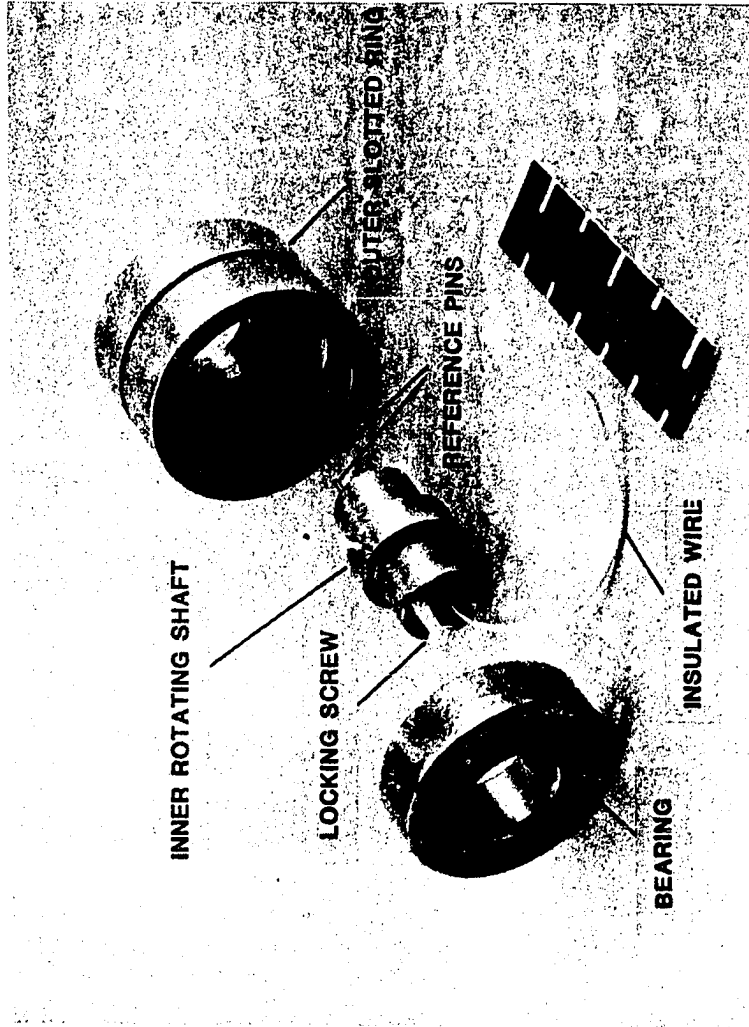
Fig. 33 Instrumented pin - exploded view.
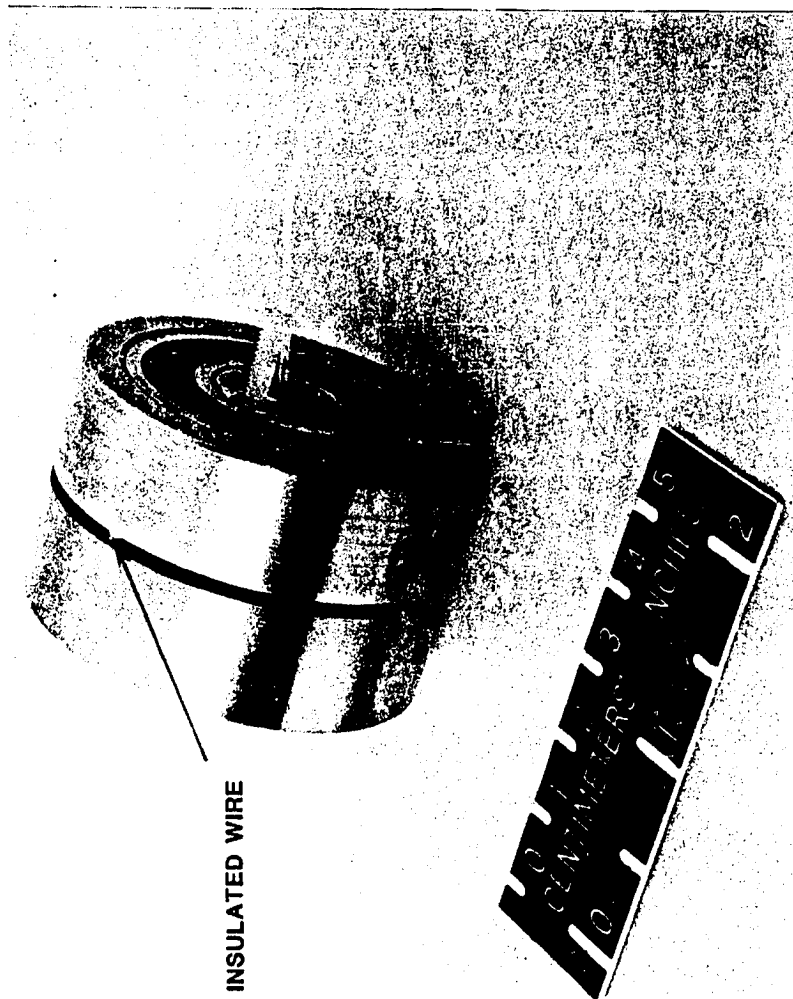
INSULATED WIRE

Fig. 34 Instrumented pin - assembled view.

3.1.2 Initial Setting

For accurate pin-hole contact angle measurements, it was necessary to locate the insulated wire such that it was flush with the surface of the pin. This adjustment was made by placing the pin on a flat metal surface with the slotted half of the pin facing the metal surface. With the pin held stationary, the inner shaft was rotated until the insulated wire touched the metal surface and activated an electrical circuit. If the insulated wire was not flush with the pin surface, but protruded outside the slot, then the electrical circuit remained activated over a finite arc of inner shaft rotation. If the insulated wire stayed below the pin surface, inside the slot, then the electrical circuit was not activated over the entire 180 degree rotation of the inner shaft. When the insulated wire was flush with the pin surface, it touched the metal surface at just one point over the entire rotation of the inner shaft and the electrical circuit was activated at that point. It was thus possible to locate the insulated wire such that it lay flush with the pin surface. The wire was fixed in this location by means of a set screw (Fig. 33).

3.1.3 Test Procedure and Results

The specimen was a 4.41 mm thick T300/5208, 32-ply, quasi-isotropic laminate with a $[0/45/90/-45]_{4s}$ layup. It had a 50.8 mm diameter hole which was loaded using a 49.8 mm diameter instrumented pin (see Fig. 35). This resulted in a pin-hole clearance of 1.0 mm. The width (w) of the plate was 139.7 mm and the end distance, e, (from the center of the hole to the free end) was 127 mm. This resulted in a plate-width to hole-diameter ratio (w/d) of 2.75 and a
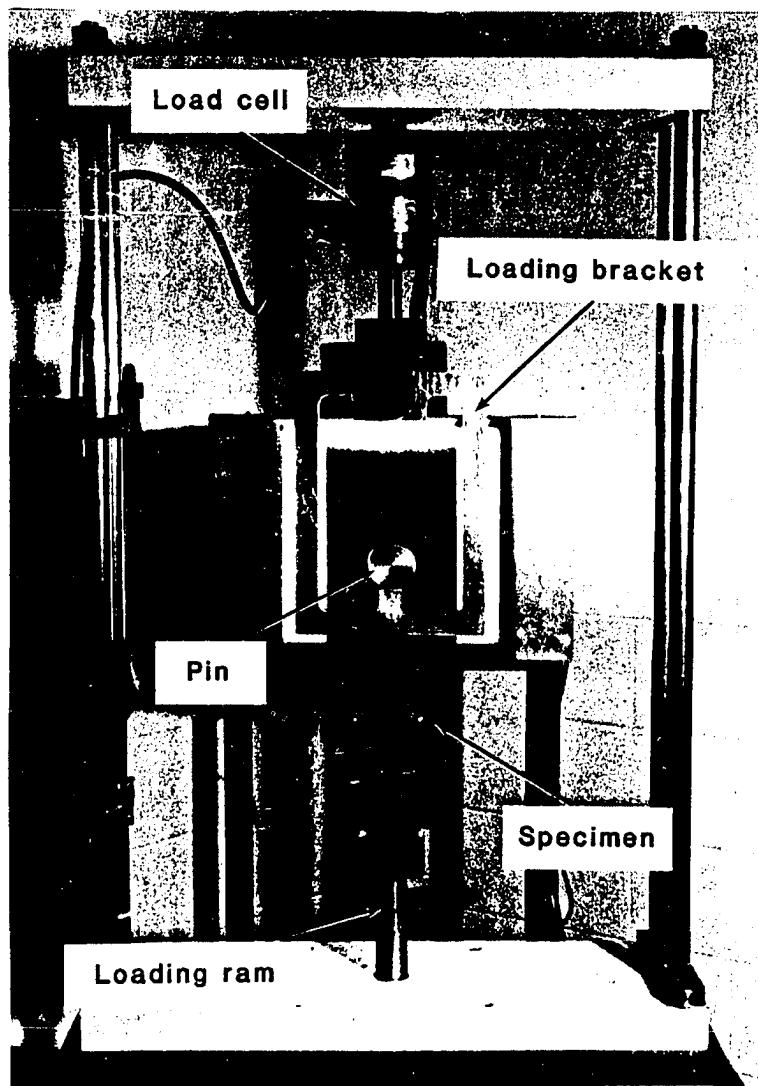
Fig. 35 Specimen configuration and load arrangement.

end-distance to hole diameter ratio (e/d) of 2.5. The pin was placed in the hole such that the slot in the pin was oriented towards the bearing side of the hole and was located in the middle of the plate thickness. A make-or-break electrical circuit was connected between the graphite/epoxy specimen and the insulated wire. This electrical circuit was activated when the rotation of the inner shaft caused the insulated wire to make contact with the hole in the graphite/epoxy plate. Throughout the region of pin-hole contact, the insulated wire made contact with the hole in the graphite/epoxy plate. Therefore the electrical circuit remained activated over the entire arc of pin-hole contact. The angle subtended by this contact arc was measured with a universal bevel protractor (least count 5 min.) using the dow-els on the face of the inner shaft and outer ring as reference. Con-tact angle measurements were made at increasing pin load levels and the results are shown in Fig. 36. Similar measurements were made for an aluminum specimen to assess the influence of interfacial friction.

The load-contact measurements for the aluminum specimen were obtained for two different values of interfacial friction and are plotted in Fig. 37. The static coefficient of friction, μ, between the bare steel pin and the aluminum plate was 0.33. The interfacial friction between the pin and the plate was reduced by using a graphite solid lubricant at the pin-hole interface. This resulted in a static friction coefficent of 0.15. The load-contact variation predicted by the analysis technique described in Chapter 2 is also shown in Figs. 36 and 37. The analysis assumes a rigid pin and a smooth ($\mu=0$) pin-hole interface. The experimental load-contact angle curves had a zero shift of about 10 degrees at no load. This
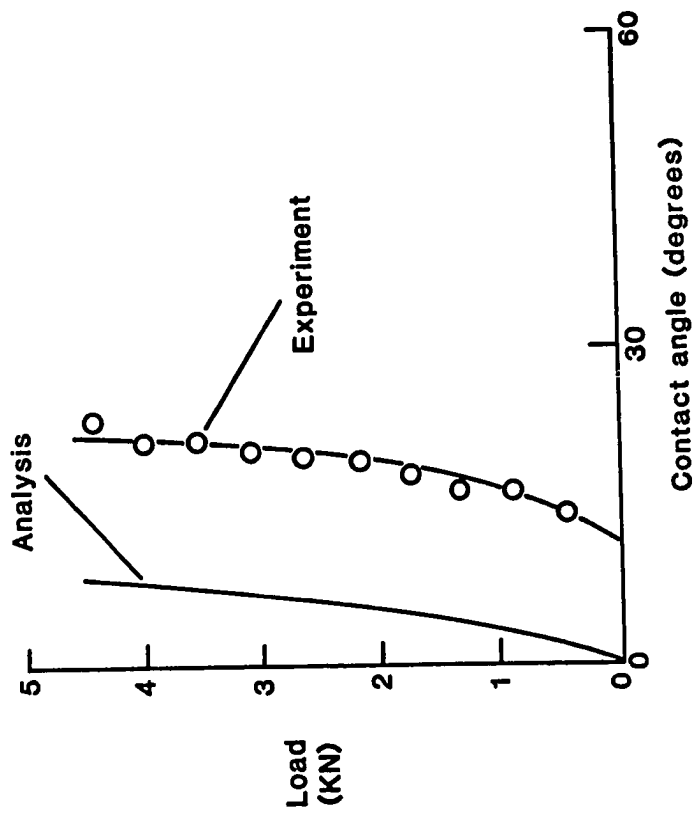
Fig. 36 Experimental and analytical load-contact variations in graphite/epoxy.
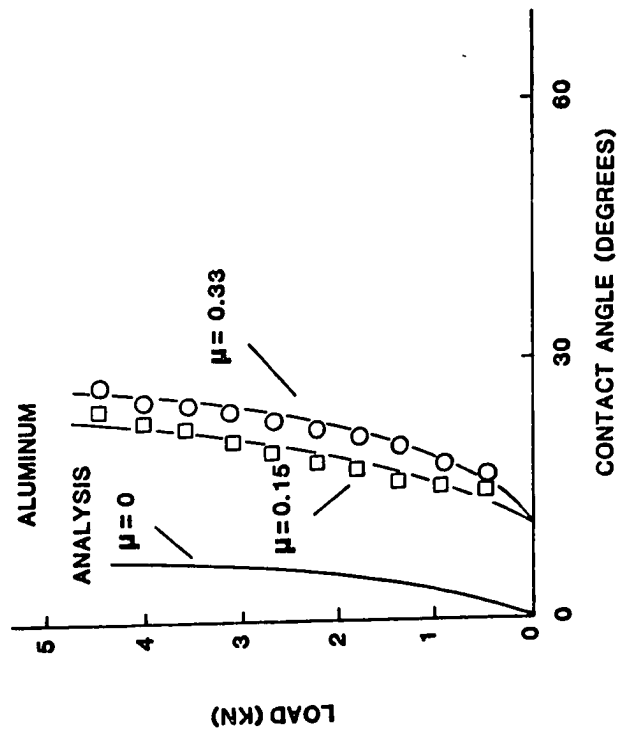
Fig. 37 Experimental and analytical load-contact variations in aluminum.

zero shift was a characteristic of the measurement technique and was called the "dead" contact angle. This dead contact angle was found to be a function of the hole diameter relative to the pin diameter. Figure 38 shows the variation of the dead contact angle with 1/R, where R is the hole radius. Figures 39 and 40 show the load-contact angle variations for graphite/epoxy and aluminum respectively after the dead contact angle was subtracted from the experimental readings. For both materials, the trend of the experimental load-contact angle variations is the same as the trend given by the finite element analysis. In the case of aluminum, it is clear that if the coefficient of friction can be further reduced, the experimental curve will approach the analytical curve.

3.2 Optical Fiber Technique

The electrical technique posed two problems: first, the dead contact angle had to be accounted for and the load-contact curves had to be shifted; second, the slit in the outer ring resulted in the bearing load being applied nonuniformly over the specimen thickness. In order to overcome these shortcomings the load-contact variation in the graphite epoxy specimen was also measured by an optical fiber sensing system. A light source was placed on one side of the loaded hole and an optical fiber sensed the light on the other side. Since the graphite/epoxy plate and the steel pin were opaque, there would be no light transmission in the region of pin-hole contact. However, in the region of no contact, light would be transmitted through the gap in the clearance-fit pin joint (Fig. 41). The optical fiber would therefore conduct light only in the no contact
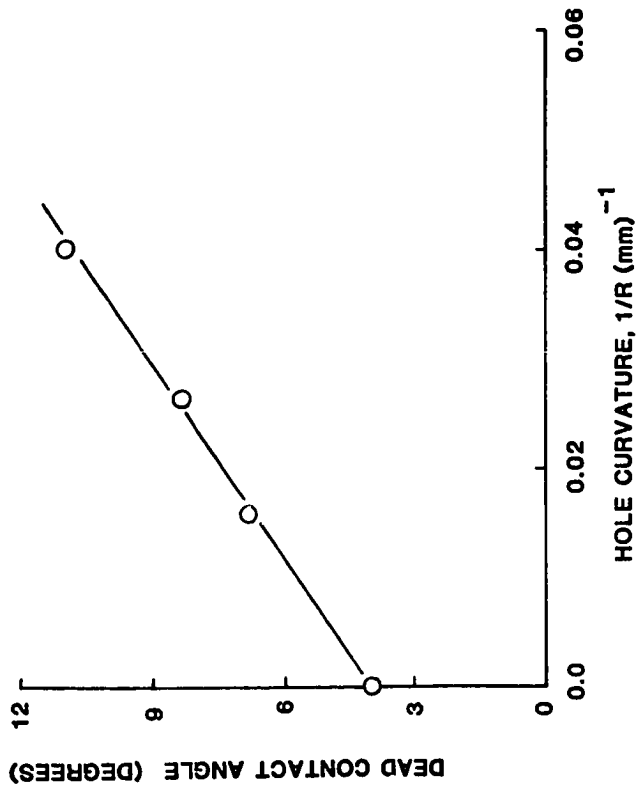
Fig. 38 Variation of dead contact angle with 1/R.
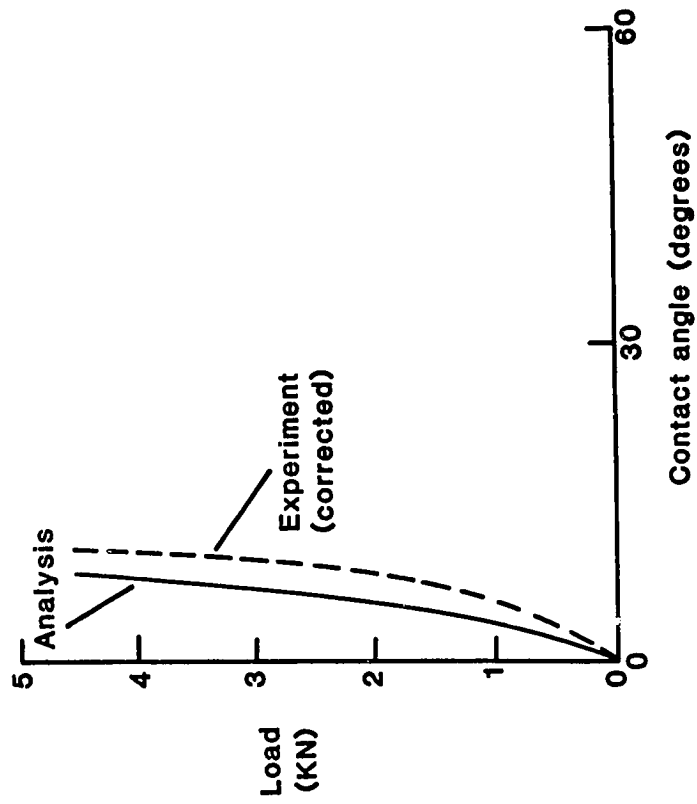
Fig. 39 Load-contact angle variation for graphite/epoxy after accounting for dead contact angle.
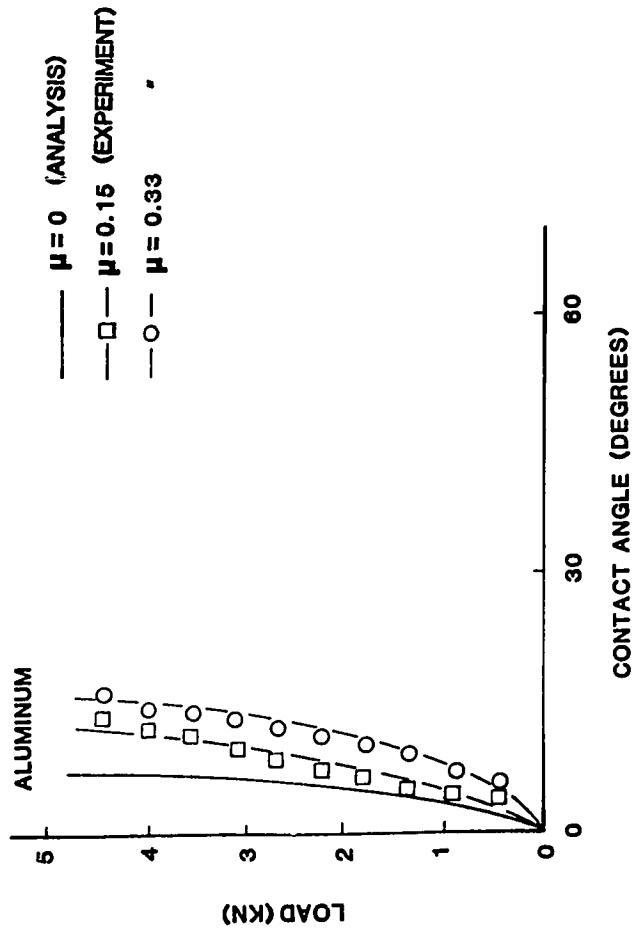
Fig. 40 Load-contact angle variation for aluminum after accounting for dead contact angle.
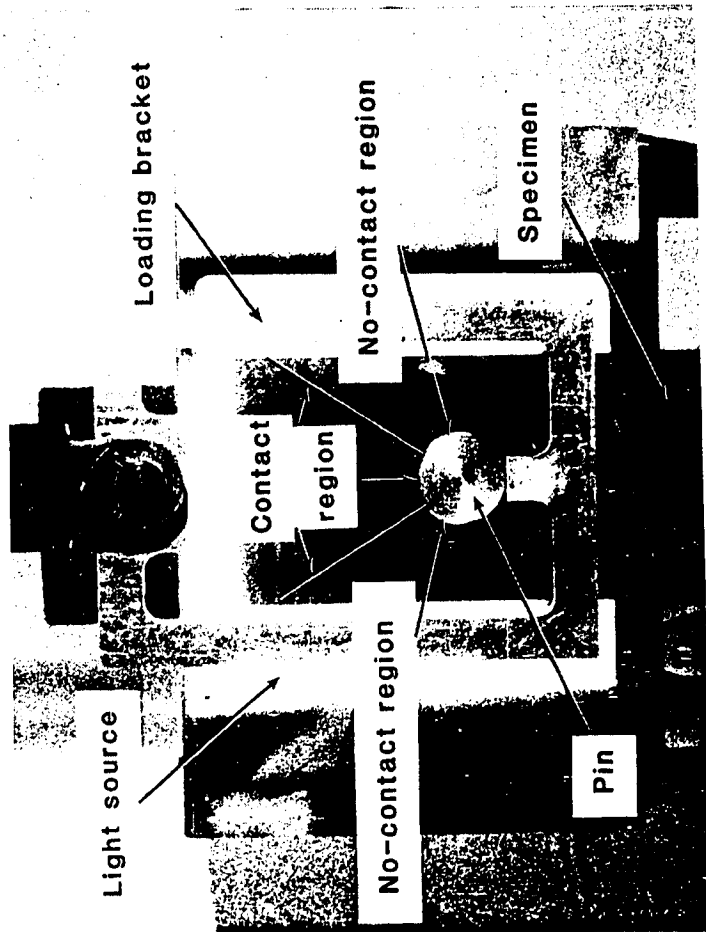
Fig. 41 Pin-hole interface with light source behind.

region. This concept was the basis of the present technique. The optical fiber used was a commercial, multimode, graded-index fiber with a 50 μm core diameter. A specially instrumented pin was used to locate the optical fiber at the pin outer diameter and to rotate it along the pin-hole interface.

3.2.1 Instrumented Pin

The instrumented pin was made of steel and was similar to the pin used for the electrical technique (see Section 3.1.1) in many respects. It consisted of an inner rotating shaft and an outer stepped ring (see Fig. 42). The outer ring had a stepped outer surface. The surface that loaded the hole in the graphite/epoxy specimen had a 49.8 mm diameter and was 7.94 mm wide. On either side of this centrally located bearing surface was a stepped down surface of diameter 46 mm. The purpose of this stepped down diameter was to allow for the location of the optical fiber close to the pin bearing surface. The inner rotating shaft was placed on bearings that fitted inside the outer stepped ring. In the assembled pin, the inner rotating shaft protruded out on one side. A vertical adjusting bar (see Fig. 43) was attached to this protruding inner rotating shaft. On the other side of the inner rotating shaft, provision was made to hang counterweights. The optical fiber was mounted on a horizontal adjusting bar which was attached to the vertical adjusting bar. The inner rotating shaft, along with the vertical and horizontal adjusting bars and the optical fiber were all free to rotate inside the outer stepped ring when the pin was under load. In order to accurately measure the angle of rotation of the inner shaft and
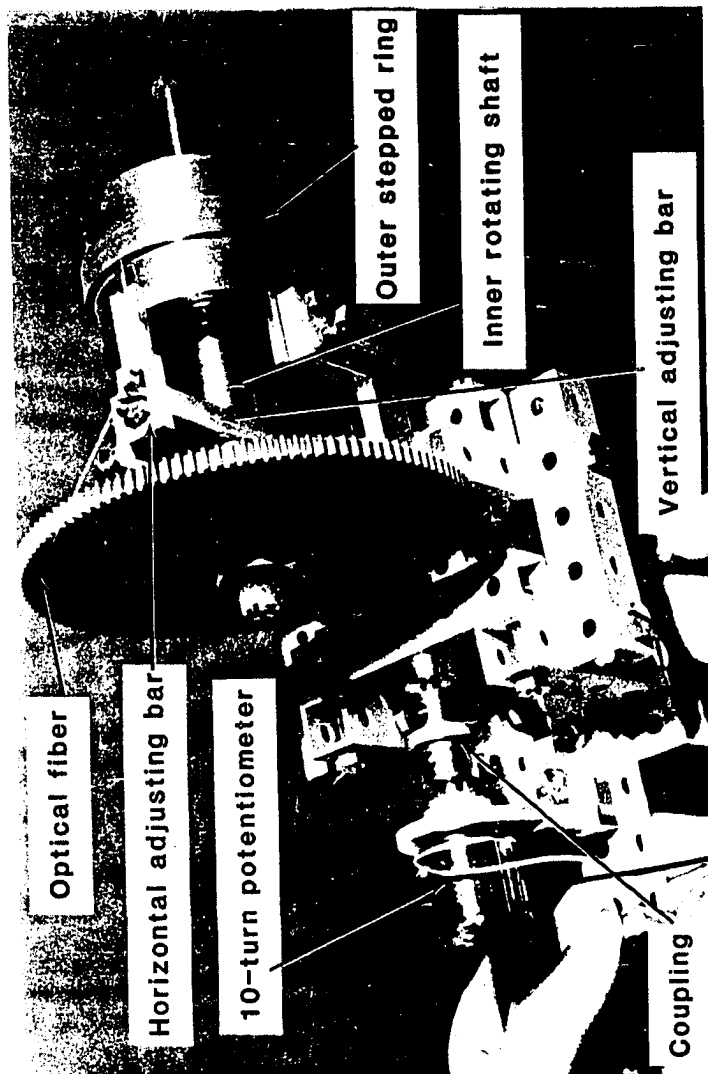
Fig. 42   Instrumented pin for optical fiber technique.
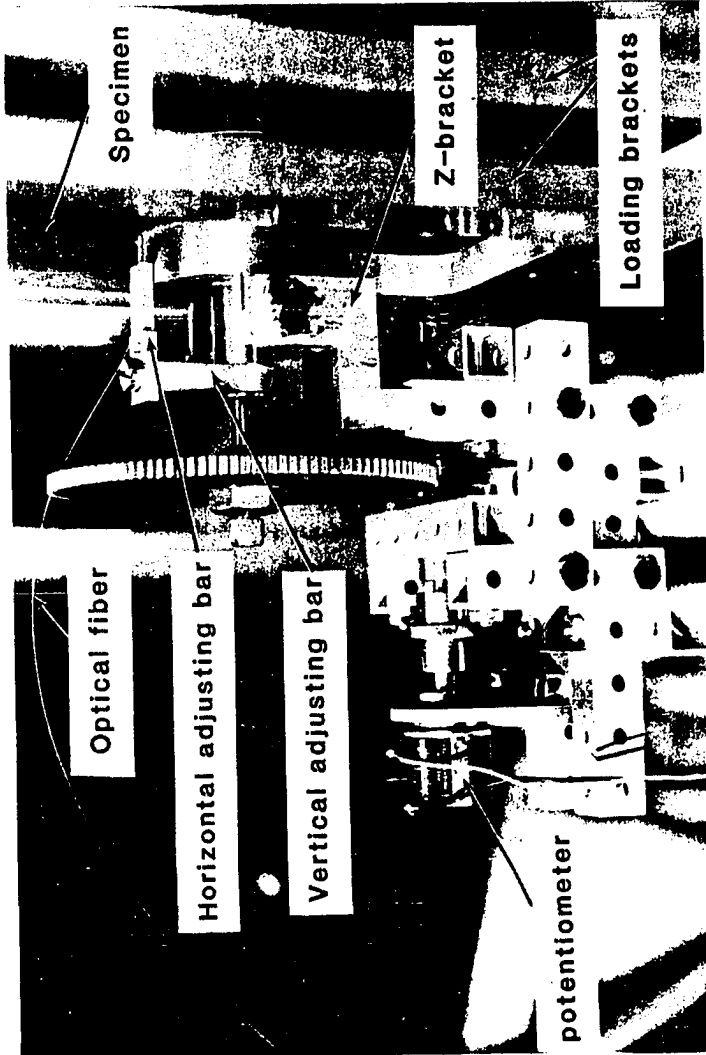
Fig. 43 Instrumented pin details.

optical fiber, a system of gears and a 10-turn potentiometer were used. A 120 tooth gear was attached to the inner shaft. This gear meshed with a 12 tooth gear on another shaft which was coupled to the 10-turn potentiometer. Thus ten turns of the potentiometer corresponded to one turn of the inner rotating shaft and optical fiber. The potentiometer was calibrated to measure inner shaft rotation in degrees (least count 2 min.). The 12 tooth gear shaft and potentiometer assembly was attached to the outer stepped ring by a Z-bracket. The instrumented pin, with the inner rotating shaft, the outer stepped ring, the optical fiber, the system of gears and the potentiometer could be handled as one unit.

3.2.2 Initial Setting

For accurate pin-hole contact angle measurements, it was necessary to locate the optical fiber such that it was just above the surface of the pin outer diameter (49.8 mm). This adjustment was made by placing the instrumented pin assembly on the loading frame (see Figs. 44 and 45) and loading the hole in the graphite/epoxy specimen. The specimen had a 50.8 mm diameter hole. This resulted in a pin-hole clearance of 1.0 mm. A light source on the other side of the specimen caused light to pass through the gap in the pin-hole interface (see Fig. 41). With the pin held stationary (due to the applied load), the inner shaft was rotated until the optical fiber was in a region where the pin-hole gap was large. Light that passed through this gap was picked up by the optical fiber and sensed by a photodiode/amplifier system. The horizontal adjusting bar was first used to locate the optical fiber very close to the pin-hole inter-
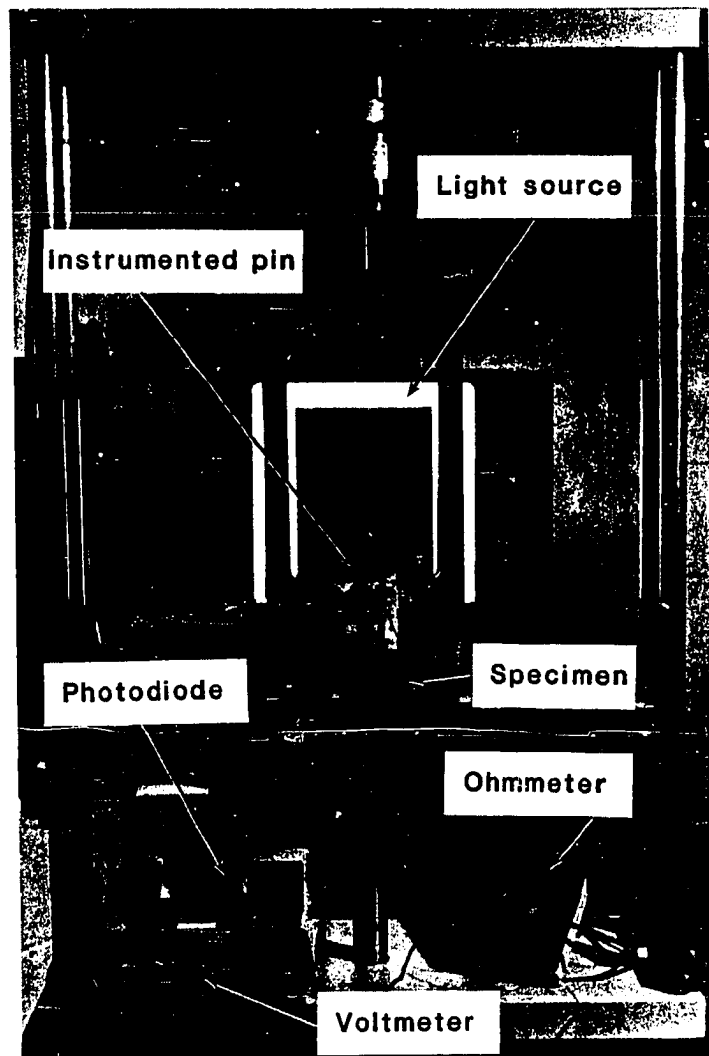
Fig. 44 Loading and sensing system - front view.
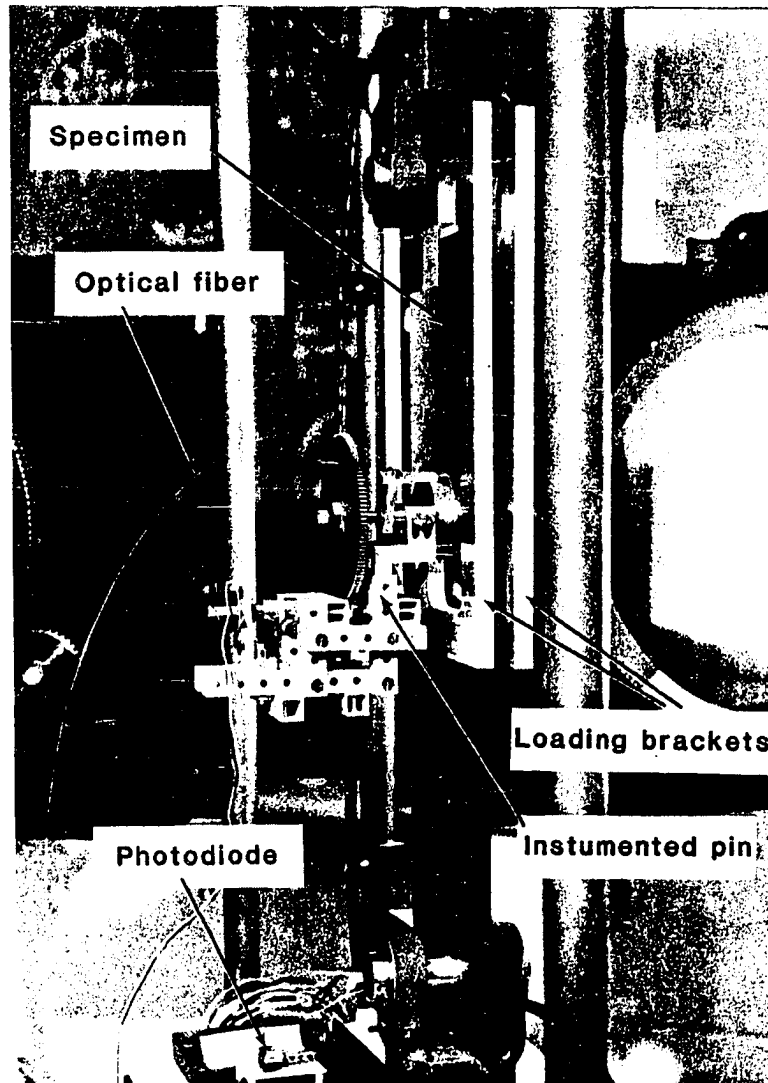
Fig. 45 Loading and sensing system - side view.

face. Then the vertical adjusting bar and the photodiode sensing system were used to locate the optical fiber just above the surface of the pin. When the optical fiber is below the surface of the pin, very little light is sensed by the photodiode. As the optical fiber is moved towards the pin surface there is a sudden increase in the photodiode output. The vertical adjusting bar was fixed in this location. The optical fiber is thus located just above the pin surface and ready to make contact angle measurements.

3.2.3 Test Procedure and Results

Contact angles were measured at increasing load levels. At each load level the contact angle was measured by rotating the inner shaft in just one direction (say clockwise) starting at one end of its travel. This caused the optical fiber to move (along the pin surface) first, through the no contact region, then the contact region and finally the no contact region (see Fig. 41). As the optical fiber moves through the no contact region and towards the contact region, there is a monotonic decrease in the photodiode output. This is due to the decreasing gap between the pin and the hole. When the optical fiber moves into the contact region there is no further decrease in the photodiode output which remains constant throughout the contact region. Further rotation of the inner shaft causes the optical fiber to move out of the contact region and into the no contact region. This is indicated by the monotonically increasing output from the photodiode/amplifier system. The angle over which the photodiode output remained constant was measured, using the potentiometer, as the contact angle. Contact angle measurements (Fig. 46)
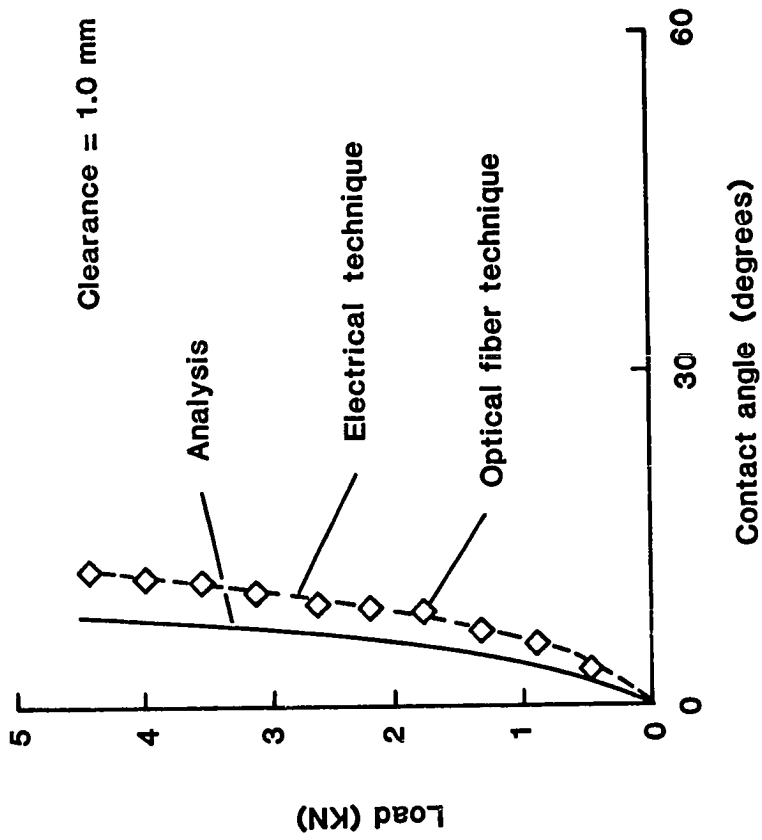
Fig. 46 Load-contact angle variation by optical fiber technique.

were made at increasing pin load levels. The measured angles by the present technique show excellent correlation with the load-contact variation obtained by the electrical technique of Section 3.1.

3.3 The Layout Fluid Technique

The contact angle in a clearance-fit bearing-loaded specimen can also be measured by this simple technique. The layout fluid technique consists of applying a thin layer of blue layout fluid on the bolt-bearing surface prior to load application. After the layout fluid has dried, the bolt can be used to load a bearing-loaded test specimen. The bolt is carefully removed from the test hole after loading to a desired level and then unloading. The layout fluid on the bolt gets scraped off in the region of bolt-hole contact and the impression left on the bolt can be used to measure the contact angle. This method was used to determine contact angles at increasing load levels, for the aluminum specimen, and the results are shown in Fig. 47. The measured angles by the layout fluid technique show excellent correlation with the load-contact variation obtained by the electrical technique of Section 3.1. The present technique is not very convenient for the determination of load-contact curves as it involves loading, unloading and the application of layout fluid to the bolt surface at each load level.

3.4 Photoelastic Results

The load-contact angle measurements clearly showed the influence of interfacial friction in a pin-loaded joint. In order to verify the finite element stress predictions photoelastic tests were
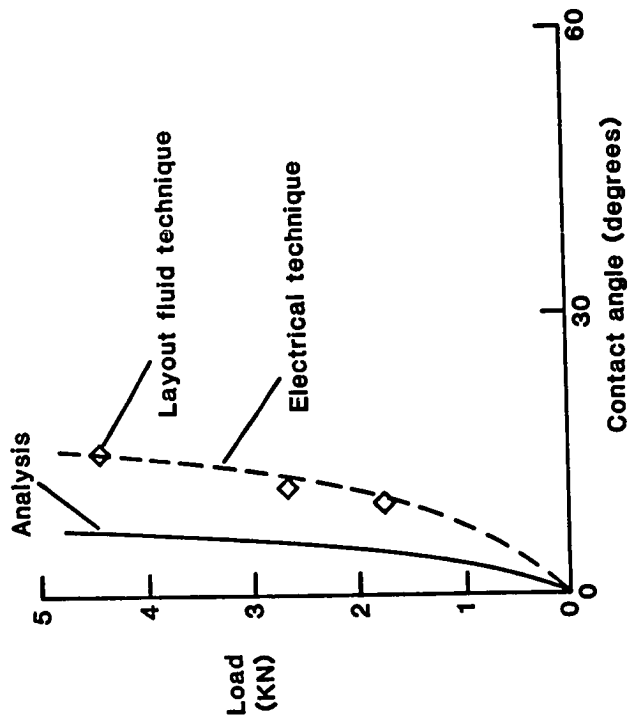
Fig. 47 Load-contact angle variation by layout fluid technique.

performed. The isochromatic fringe patterns for a polycarbonate specimen were used to determine the maximum shear stress distributions along the net-tension, shearout and bearing planes. The disturbances in the fringe patterns along the bolt-hole interface were the basis of the "photoelastic technique" for the measurement of load-contact variations in clearance-fit loaded holes. Photoelastic results for the stresses and load-contact variations were compared with results obtained numerically.

3.4.1 Test Procedure

The test specimen configuration and the loading arrangement used was similar to that shown in Fig. 35. The isotropic polycarbonate specimen was 6.35 mm thick and had a 50.8 mm diameter hole which was loaded using a 49.8 mm diameter pin. This resulted in a pin-hole clearance of 1.0 mm. The width of the plate was 139.7 mm and the end distance (from the center of the hole to the free end) was 127 mm. This resulted in a plate-width to hole-diameter ratio (w/d) of 2.75 and a end-distance to hole diameter ratio (e/d) of 2.5. To load the specimen without obscuring the neighbourhood of the hole, a special loading fixture was devised (see Fig. 35). With this loading arrangement, most of the region around the hole was visible. The material fringe value, f, for the polycarbonate was determined by the standard circular disc calibration method [50] as f = 6937 (N/m) per fringe order. The isochromatic fringes in a polycarbonate specimen represent contour lines of maximum shear stress (τ_{max}). The τ_{max} along a contour is given by,

$$\tau_{max} = \frac{N\ f}{2\ t} \tag{3.1}$$

where N is the fringe order, f the material fringe value and t is the thickness of the specimen. The isochromatic fringe patterns for the bearing-loaded polycarbonate specimen were photographed at successively increasing loads.

3.4.2 Results

Light field isochromatic fringe patterns for the polycarbonate specimen corresponding to bearing load levels of 245 N, 800 N and 1134 N are shown in Figs. 48, 49 and 50, respectively. The vertical centerline in all photographs represents the loading axis with the bearing load applied upwards. As expected, the fringe patterns are symmetric about the loading axis. The fringes in Fig. 50 were used along with equation (3.1) to determine the maximum shear stress distributions along the net-tension, bearing and shearout planes (see Figs. 51-53). The x-axis is along the loading direction, the y-axis along the net-tension plane and the line y = d/2 lies along the shearout plane in all three figures. Also shown in Figs. 51, 52 and 53 are the corresponding τ_{max} distributions obtained numerically by the stress analysis method described in Chapter 2. There is generally good agreement between the experimental and analytical results especially in the region away from the bolt. In the vicinity of the bolt-hole interface the experimental stresses are influenced by the interfacial friction. Frictional effects are not accounted for in the analysis and this may be the reason for small differences in the stresses near the bolt-hole interface.

Fig. 48 Light-field isochromatic fringe pattern for polycarbonate specimen (load = 245 N, w/d = 2.75, e/d = 2.5, c_d = 2%)
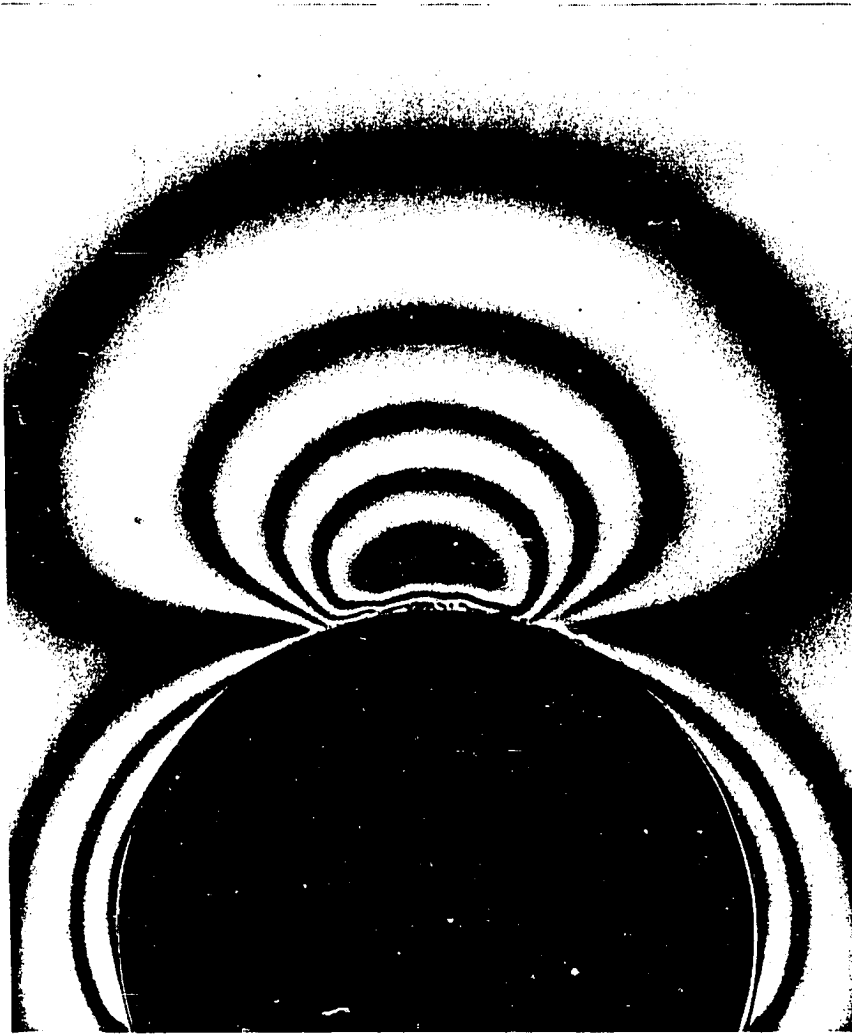
Fig. 49 Light-field isochromatic fringe pattern for polycarbonate
specimen (load = 800 N, w/d = 2.75, e/d = 2.5, c_d = 2%)
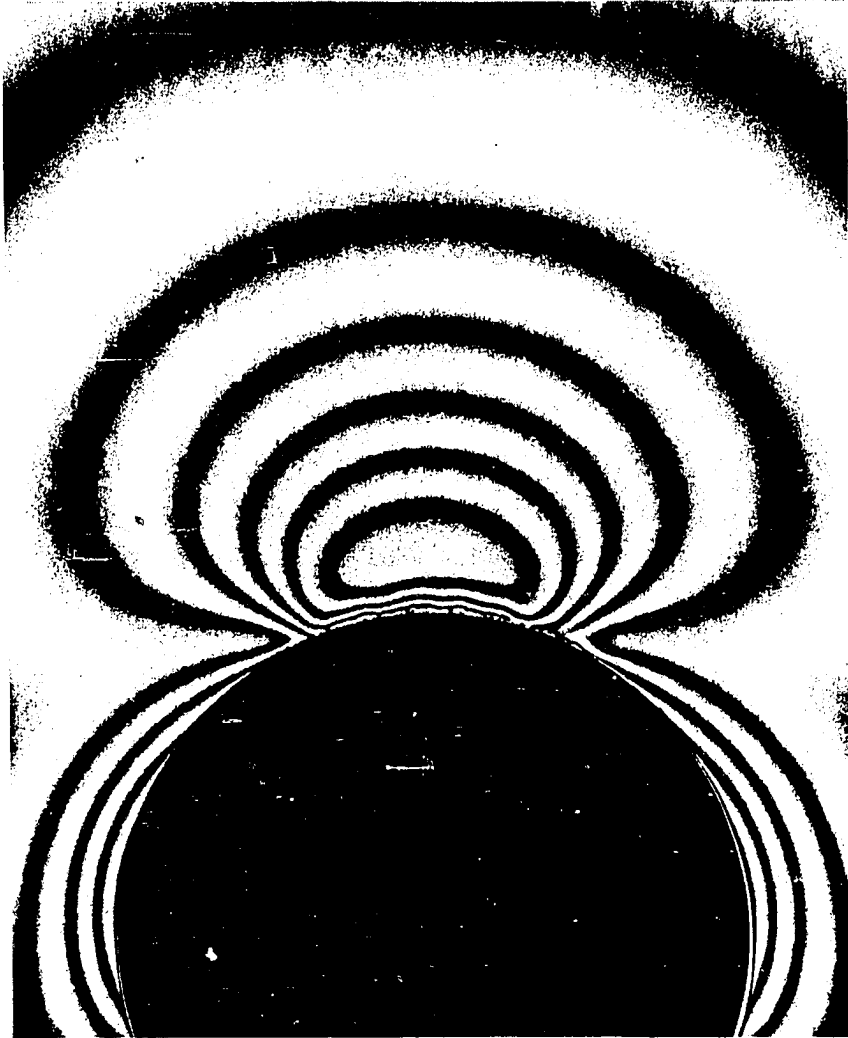
Fig. 50 Light-field isochromatic fringe pattern for polycarbonate
specimen (load = 1134 N, w/d = 2.75, e/d= 2.5, c_d = 2%)
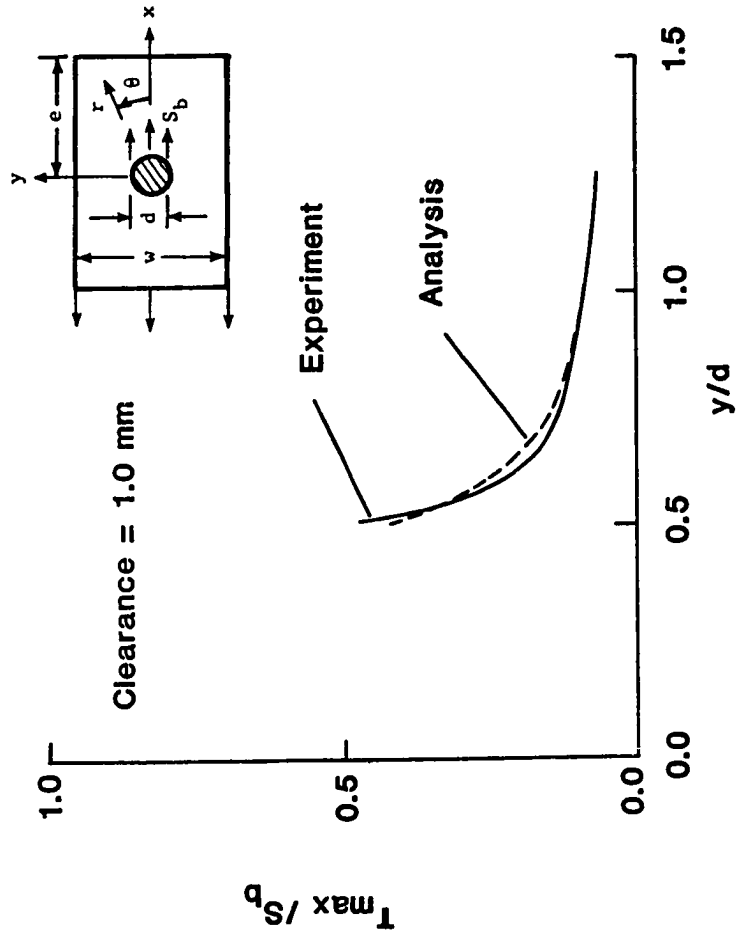
Fig. 51 Maximum shear stress distribution along net-section.
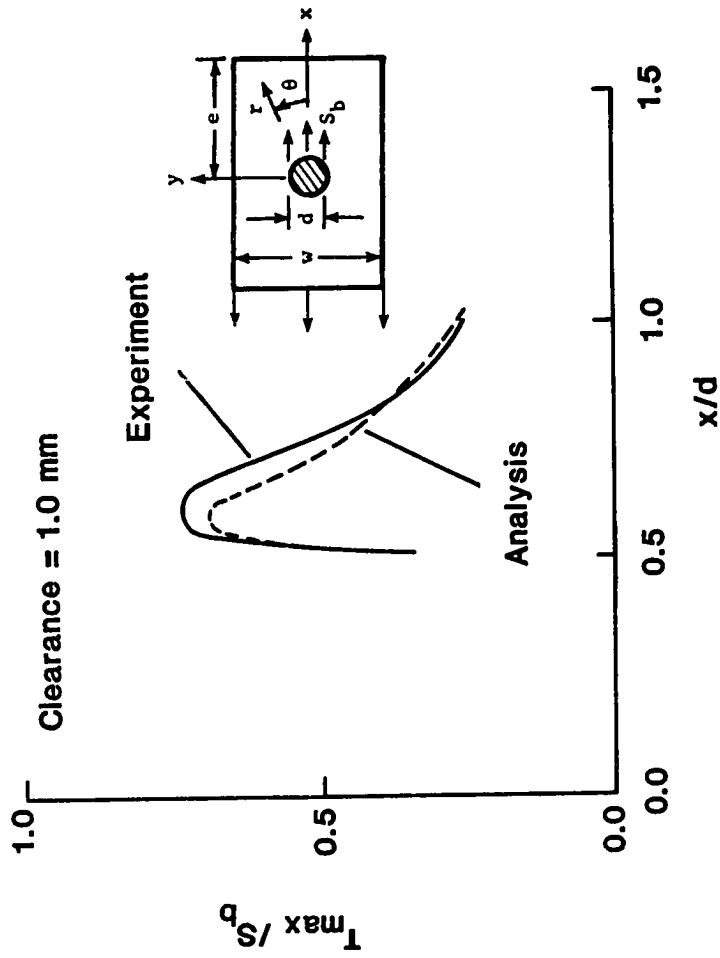
Fig. 52 Maximum shear stress distribution along loading axis.
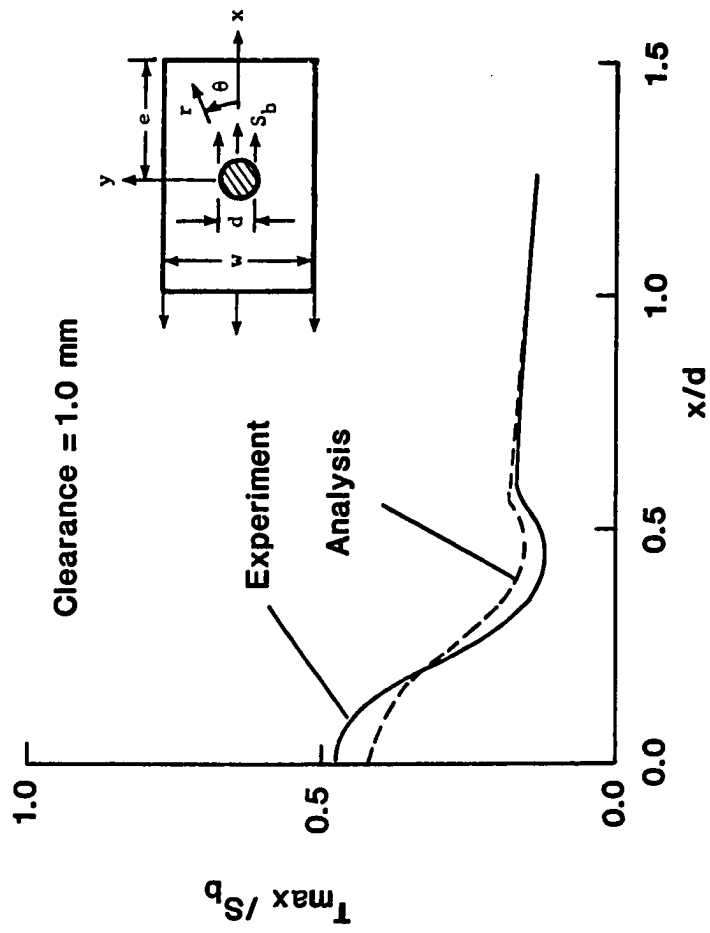
Fig. 53 Maximum shear stress distribution along shearout plane.

The photoelastic fringes in Figs. 48, 49 and 50 were also used for the measurement of contact angles at each load level. The fringe patterns at the bolt-hole interface exhibit small disturbances in the region of bolt-hole contact. This was the basis of the "photoelastic technique" for the measurement of contact angles at each load level. Contact angles were measured at each load level to construct the load-contact curve of Fig. 54. The results from the electrical technique, which was applicable to polycarbonate when the hole surface was covered with silver paint, are also shown in this figure. It is seen that the results from the two experimental techniques agree very well. The analytical load-contact curve for the polycarbonate specimen is also shown in the same figure. As shown earlier in Fig. 40, the experimental curve in Fig. 54 would approach the analytical curve if the friction at the pin-hole interface were reduced.

The tests on the polycarbonate specimens lead to an assessment of the influence of interfacial friction. The load-contact angle variations in Fig. 54 show considerable discrepancy between the finite element predictions and the measured values. This discrepancy is attributed, in most part, to friction between the pin and the hole, which is neglected for convenience in the finite element analysis. The stress distribution results shown in Figs. 51, 52, 53, however, show that the photoelastic results and the finite element results do not differ greatly. This appears to indicate that the interfacial friction influences the contact angle more than the stresses. Thus the use of the simple finite element analysis (that does not account for interfacial friction) in strength predictions is justified.
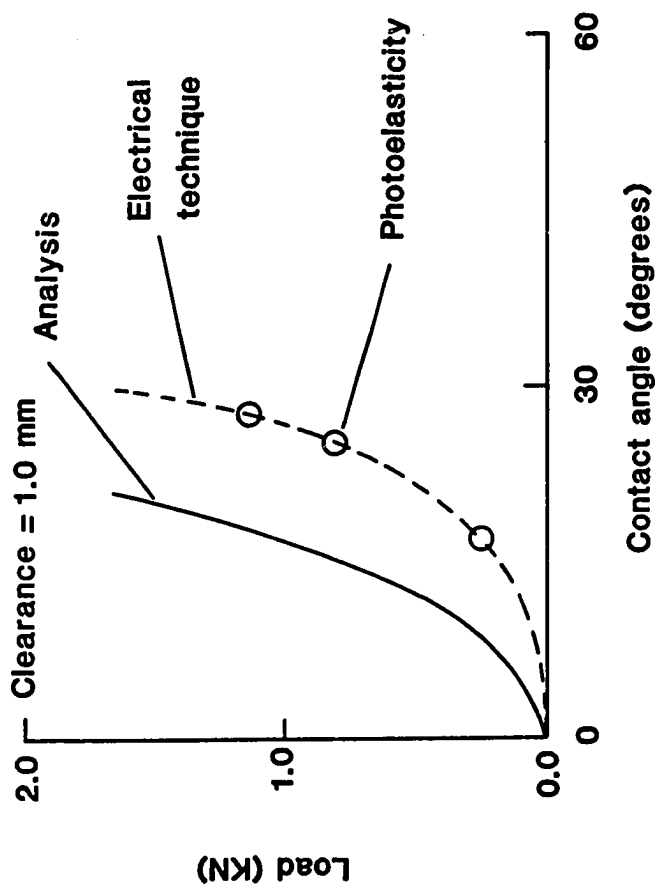
Fig. 54 Load-contact angle variation by the photoelastic technique.

CHAPTER 4

BEARING-BYPASS TESTING

Within a multi-fastener structural joint, fastener holes may be subjected to the combined effects of bearing loads and loads that bypass the hole, as illustrated in Fig. 7. The ratio of bearing load to bypass load depends on the joint stiffness and configuration. As the joint is loaded, this bearing-bypass ratio remains nearly constant until joint damage develops. Although the combined effects of bearing and bypass loads can be simulated by testing single-fastener specimens, such tests are difficult. The various approaches used for bearing-bypass testing have involved complex apparatus to simultaneously apply the bearing and bypass loads. As a result, very little bearing-bypass data have been reported. Virtually nothing has been reported for bearing-bypass loading in compression.

The test approach presented in this chapter was developed at the NASA Langley Research Center and is described in Ref. 52. It employs two hydraulic servo-control systems synchronized to apply proportional bearing and bypass loads to a laminate specimen with a central hole. The laminate tested was T300/5208 graphite/epoxy with a 16-ply quasi-isotropic layup. The bearing loads were applied through a 6.35 mm steel bolt with a clearance fit. In the present study, some tests were stopped when the load displacement record began to indicate specimen damage. The damage modes were determined

by radiographing each specimen after testing. Reference 14 showed that such damage onset could be accurately analyzed using the elastic stresses at the hole boundary. Specimens were also tested to failure to determine ultimate failure loads, failure sequences, and failure modes. The test results were plotted as bearing-bypass strength diagrams for damage onset and ultimate strength.

4.1 Bearing-Bypass Test Machine

Three approaches to bearing-bypass testing have been used in the past with simple specimens. The first approach uses levers and linkages to divide the applied load into two proportional parts [18]. One part acts on the end of the specimen and the other is reacted as a bearing load at the specimen hole. The bolt hole is thereby subjected to proportional bearing and bypass loading. The lever fulcrum points can be changed to produce different ratios of bearing to bypass loading. This lever-linkage approach works well for tension bearing-bypass loading but is difficult to apply in compression. The second approach to bearing-bypass testing uses a "scissor" mechanism to apply a bearing load between two holes in the test specimen [17]. This bearing load is held constant while the bypass load is increased until the specimen fails. Although this approach does produce bearing-bypass loading in tension or compression, it does not maintain the desired constant ratio of bearing to bypass loads. Furthermore, this approach could alter the sequence of local damage development. The third approach uses two servo-control systems; one controls the bearing load while the other controls the bypass load [51]. The bypass load is applied to the end

of the specimen in the conventional manner; however, the bearing load is applied through linkages with two hydraulic cylinders connected to the ends of a bearing bar which is bolted to the specimen. Constant bearing bypass ratios could be maintained by synchronizing the two control systems. Although this concept works in tension and compression, the test apparatus is rather complex and quite different apparatus arrangements are needed for the two types of loading.

Although developed independently, the present test machine[52] has some similarity to that in Ref. 51. As in Ref. 51, the present system has two servo-control systems. However, the present dual-control arrangement uses an apparatus that is much simpler than that in Ref. 51. Figure 55 shows the test specimen and loading. Figure 56 shows a photograph of the test system and Fig. 57 shows a block diagram of the test system. The center of the specimen is clamped between two "bearing-reaction" plates that are attached to the load frame. The two ends of the specimen are then loaded independently by the two servo-control systems (called upper and lower in Fig. 57). Any difference between these two loads produces a bearing load at the central bolt hole. This bearing load is measured by the two load cells under the bearing-reaction plates. The end loads are synchronized by a common input signal. As a result, a constant bearing-bypass ratio is maintained throughout each test.

A photograph of the apparatus is shown by Figs. 58 and 59. Only a small portion of the specimen edge is visible in Fig. 58. This photograph shows the friction grips that load each end of the specimen and the head of the 6.35 mm steel bolt that attaches the

(a) Test specimen

(b) Bearing-bypass loading
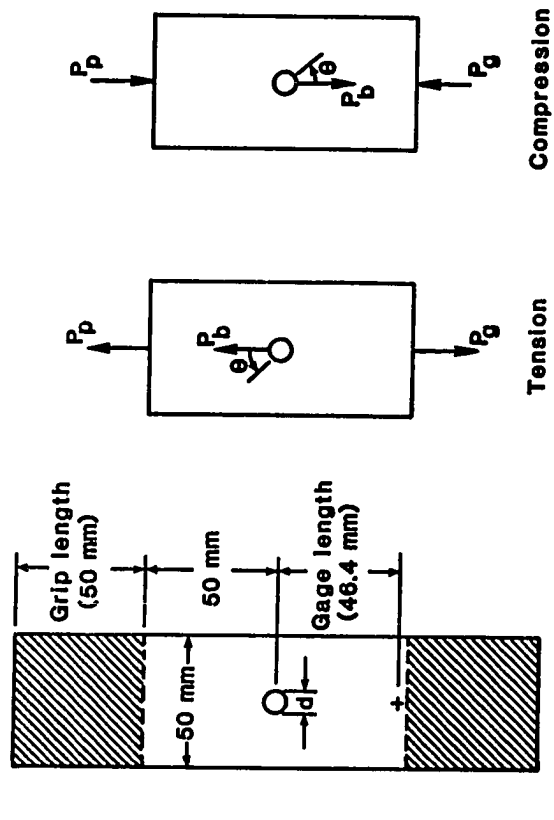
Fig. 55 Specimen configuration and bearing-bypass loading.
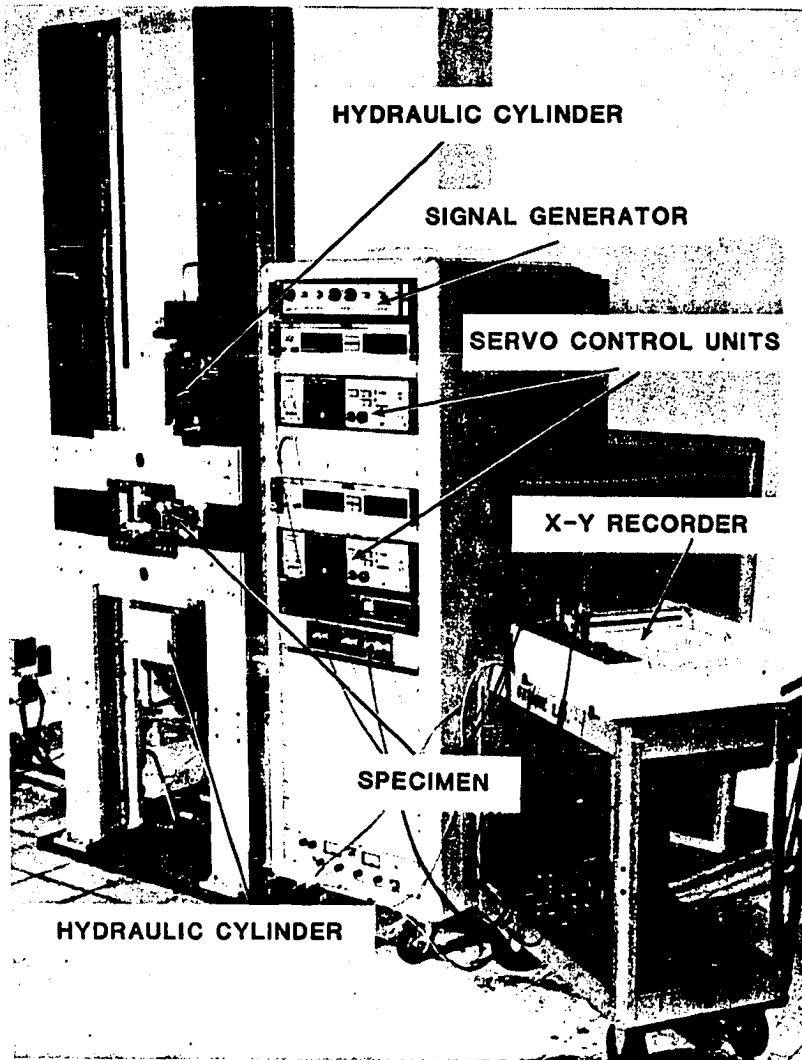
Fig. 56 Bearing-bypass test system.
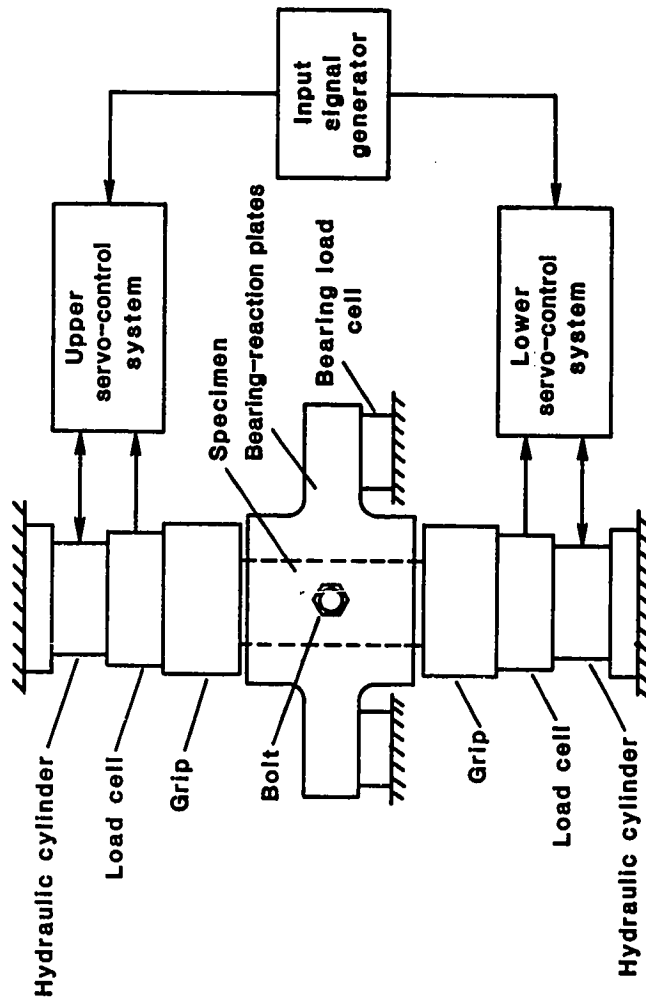
Fig. 57 Block diagram of the bearing-bypass test system.
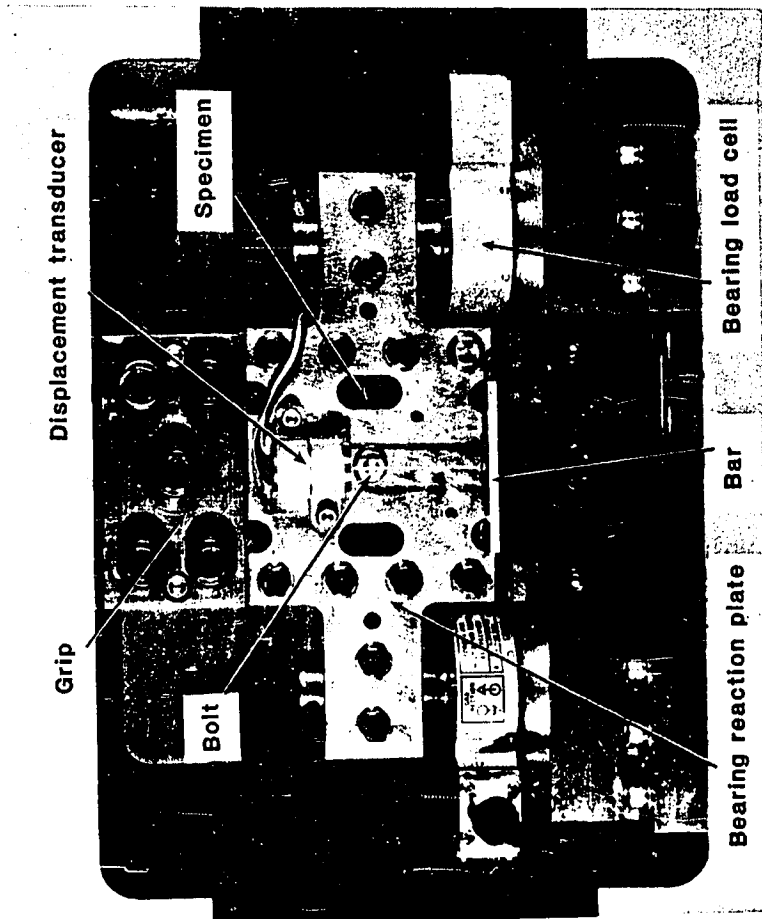
Fig. 58 Photograph of bearing-bypass test apparatus.
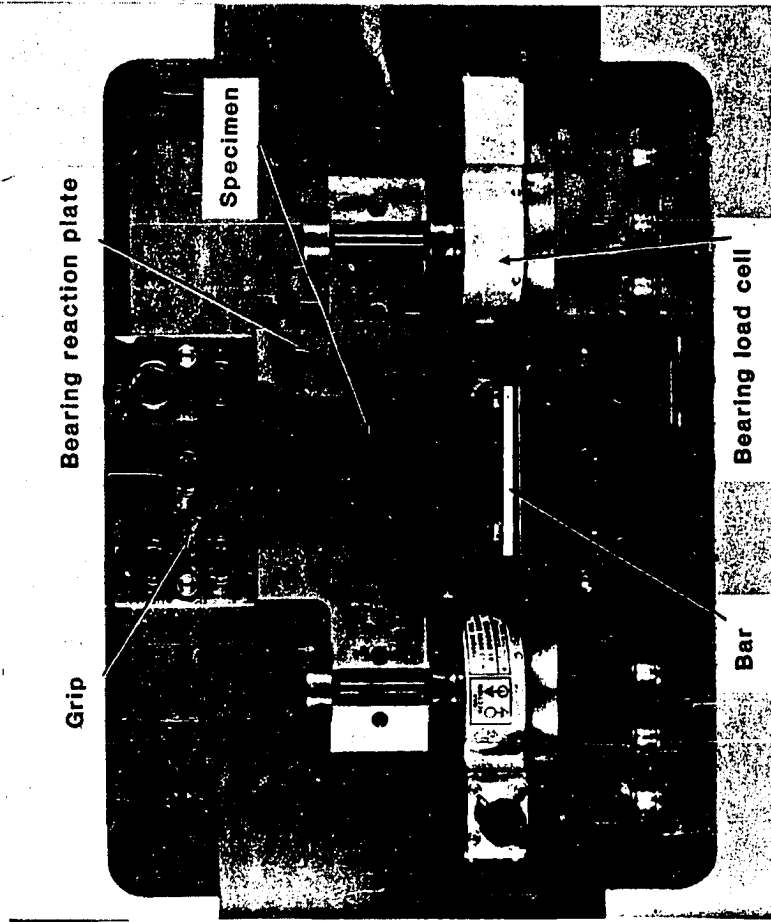
Fig. 59 Bearing-bypass test apparatus with front bearing-reaction plate removed.

specimen to the bearing-reaction plates. Notice that the bearing-reaction plates are bolted to the bearing load cells. This allows either tension or compression bearing loads to be reacted by these load cells. During compression loading, the bearing-reaction plates prevent specimen buckling. Figure 59 shows the apparatus with the front bearing-reaction plate removed.

The specimen deformation was measured throughout each test using displacement transducers. These transducers (DCDT) were mounted symmetrically on the front and back of the bearing reaction plates. (These plates were made with nonmagnetic 347 stainless steel so they would not affect the transducer performance). The transducer rods were cemented to small bars that were attached to the specimen slightly above the gripline as shown in Fig. 58. This arrangement provided a measurement of the relative displacement between the bearing-reaction plates and the specimen. These measurements were used to determine the damage onset, as explained in the next section.

Although not visible in Fig. 58, hardened steel bushings were used between the bolt and the bearing-reaction plates. These bushings had a 12.7 mm outside diameter that was machined for a sliding fit, thus allowing the bolt clampup force to be transmitted to the local region around the bearing-loaded hole. This arrangement was equivalent to having a clampup washer directly against each face of the laminate, as used in Refs. 13 and 14.

4.2 Test Specimens

The test specimens were fabricated from 16-ply quasi-isotropic graphite/epoxy laminates (T300/5208) with a $[0/45/90/-45]_{2s}$

layup. The specimen configuration is shown in Fig. 55(a). The test holes were first machined using an ultrasonic drill and then carefully hand-reamed by a diamond-coated expansion reamer. The hole diameter was controlled, by the hand reaming operation, to within 0.008 mm of the required diameter. A nominal hole diameter of 6.396 mm was used for a clearance of 0.076 mm with the 6.320 mm steel bolts. This clearance, used in previous analyses (see Chapter 2), was 1.2 percent of the hole diameter and is typical of aircraft joints. The bolts were finger tightened (about 0.2 N.m torque) to produce a very small clampup force against the specimen.

The loading notation is shown in Fig. 55(b). The test results are presented in terms of nominal stress rather than load. The nominal bearing stress S_b and nominal net-section bypass stress S_{np} were calculated from the following equations:

$$S_b = P_b/td \qquad\qquad (4.1)$$

and

$$S_{np} = P_p/t(w-d) \qquad\qquad (4.2)$$

The bearing-bypass ratio β was defined as

$$\beta = S_b/S_{np} \qquad\qquad (4.3)$$

4.3 Test Procedure

In each test, the nominal bearing and bypass stresses were plotted against specimen displacement. The tests were conducted at

the rather slow rate of 3.75 N/s at constant bearing-bypass load ratios (β = $\pm$0, $\pm$1, $\pm$3, and $\pm\infty$). Typical load-displacement curves are shown in Fig. 60 for a bearing-bypass ratio of -1. The two curves have a small initial nonlinearity (due to varying contact arc) but gradually develop a nearly linear response. At higher load levels, the curves gradually develop a second nonlinearity. This second nonlinearity indicates damage at the bolt hole, as discussed in Ref. 14. An offset of 0.001d was selected to define the damage onset level, as shown in Fig. 60. Soon after the damage-onset level was reached, some specimens were unloaded. They were then treated with an X-ray opaque dye-penetrant and radiographed to determine the damage location along the hole boundary. The damage-onset mode was deduced from the damage location as discussed in the next section. Other specimens were loaded to failure. The ultimate strength level and failure mode were recorded in each case.

4.4 Test Results

Results from the bearing-bypass tests are presented in Tables 3 and 4 and in Fig. 61. Symbols in Fig. 61 represent measured S_b and S_{np} values corresponding to damage onset and ultimate failure. Each solid symbol represents an average of three tests. The variability in the data at each test condition is indicated by short I-symbols around each solid symbol. The right side of Fig. 61 shows tension results for four β values (0, 1, 3, and ∞). The left side shows the corresponding compression results. Figure 61 also indicates the observed failure mode for each test condition.

124
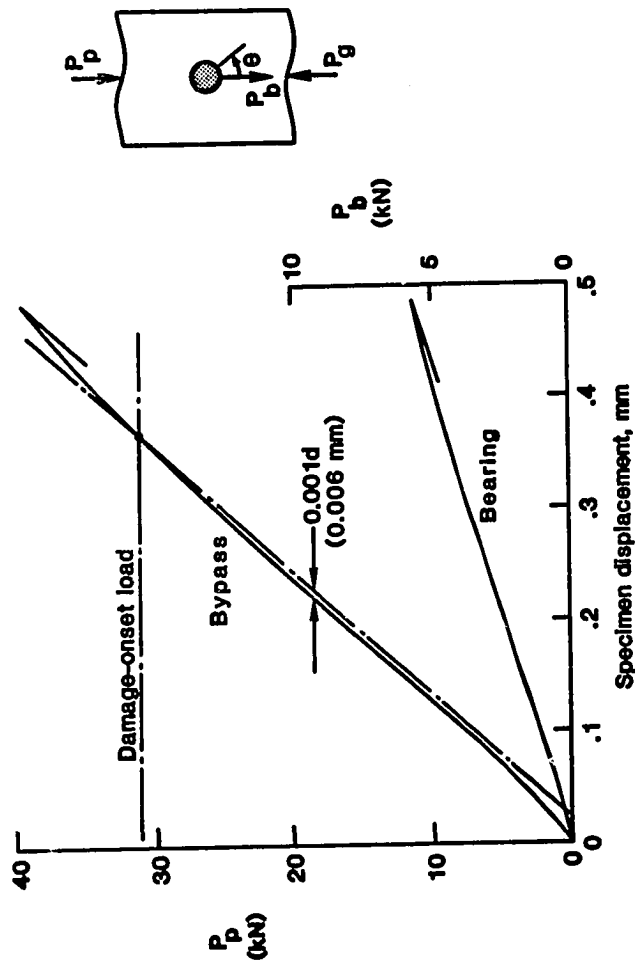
Fig. 60 Typical load-displacement curves, $\beta = -1$.

Table 3   Damage-onset test results.

Bearing-bypass ratio, β	Damage-onset strength		Damage-onset mode[a]
	S_b,MPa	S_{np},MPa	
Tension			
0	0	304	NT
1	237	237	NT
3	468	156	NT
∞	542	0	TRB
Compression			
-0	0	-422	NC
-1	314	-314	CRB/NC
-3	498	-166	CRB
$-\infty$	528	0	CRB

[a]NT - net-section tension, TRB - tension-reacted bearing, CRB - compression-reacted bearing, NC - net-section compression.

Table 4   Ultimate failure test results.

Bearing-bypass ratio, β	Ultimate failure strength		Ultimate failure mode[a]
	S_b,MPa	S_{np},MPa	
Tension			
0	0	330	NT
1	263	263	NT
3	648	216	NT
∞	812	0	TRB
Compression			
-0	0	-422	NC
-1	461	-461	OCB
-3	759	-253	OCB
$-\infty$	853	0	CRB

[a]NT – net-section tension, TRB – tension-reacted bearing, CRB – compression-reacted bearing, NC – net-section compression, OCB – offset compression-bearing.
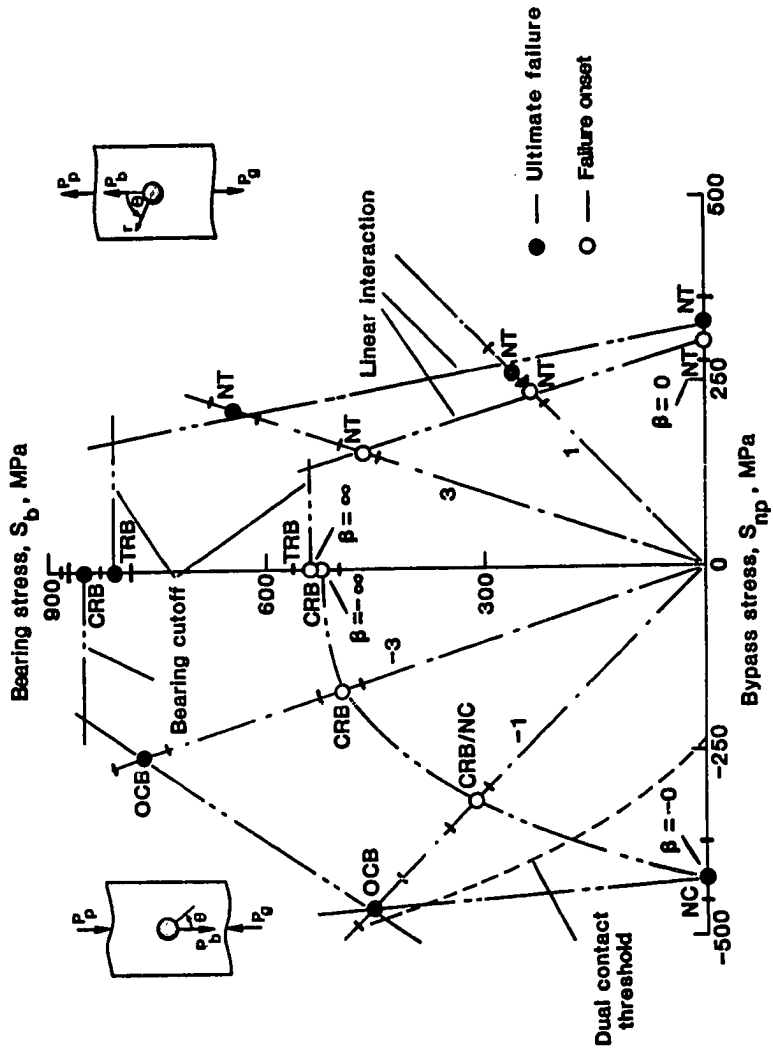
Fig. 61 Bearing-bypass diagram for damage-onset and ultimate strength.

4.4.1 Tension Results

The NT beside some symbols indicates net-section tension damage. For these cases, radiographs showed damage onset near $\theta = 90°$ on the hole boundary, as shown in Fig. 62(a). Continued loading failed these specimens through the net-section (see Fig. 63). The TRB in Fig. 61 indicates bearing damage for tension-reacted bearing loads. This damage developed at the upper edge of the hole, as shown in Fig. 62(b). On further loading these specimens failed in a bearing failure mode (see Fig. 64).

The tension cases with NT damage ($\beta = 0$, 1 and 3) could be represented, in Fig. 61, by a straight line, for both onset and ultimate failure, and thus show the linear "interaction" discussed by Hart-Smith in Ref. 12. This linearity suggests that the local stresses, responsible for damage onset and ultimate failure, may be assumed to consist of a component due to bearing and a second super-imposed component due to bypass loading. This assumption is investigated for damage onset failures in Ref. 52. The "bearing cutoff" reported by Hart-Smith [12] was represented by a horizontal line through the $\beta = \infty$ data points for damage onset and ultimate failure. The linear interaction and bearing cutoff lines through the data represent the damage onset strength and ultimate failure strength for combinations of bearing-bypass loading in tension.

4.4.2 Compression Results

The left side of Fig. 61 presents data for compression loading. The CRB indicates bearing damage for compression-reacted

(a) Net-section tension (NT)

(b) Tension-reacted bearing (TRB)

(c) Compression-reacted bearing (CRB)

(d) Net-section compression (NC)
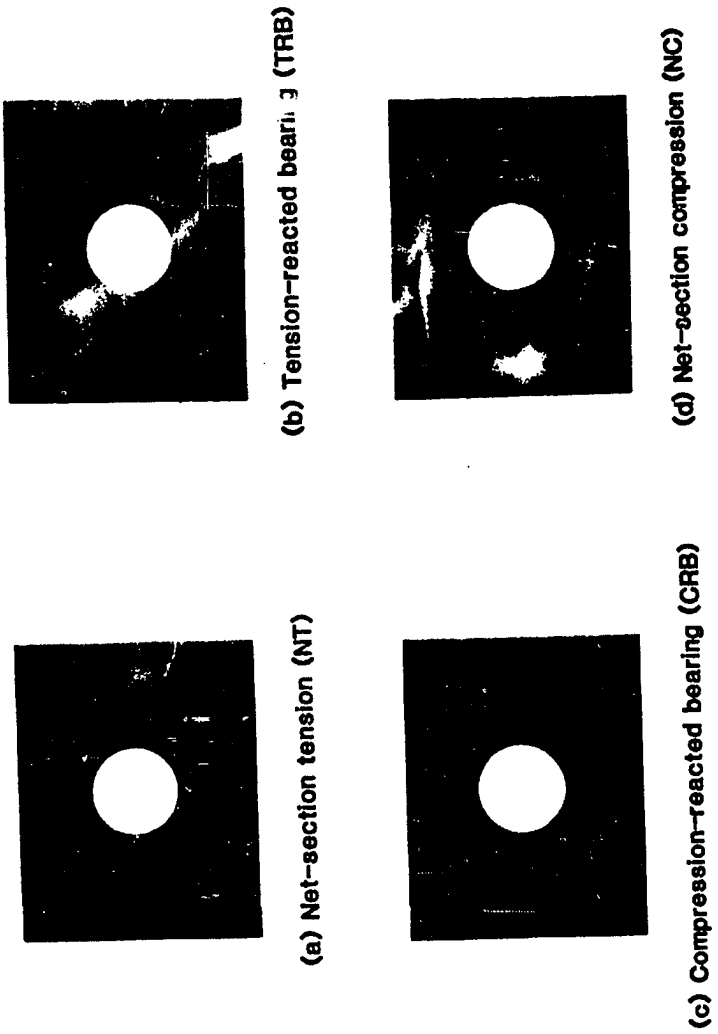
Fig. 62 Radiographs of damage-onset at fastener hole.
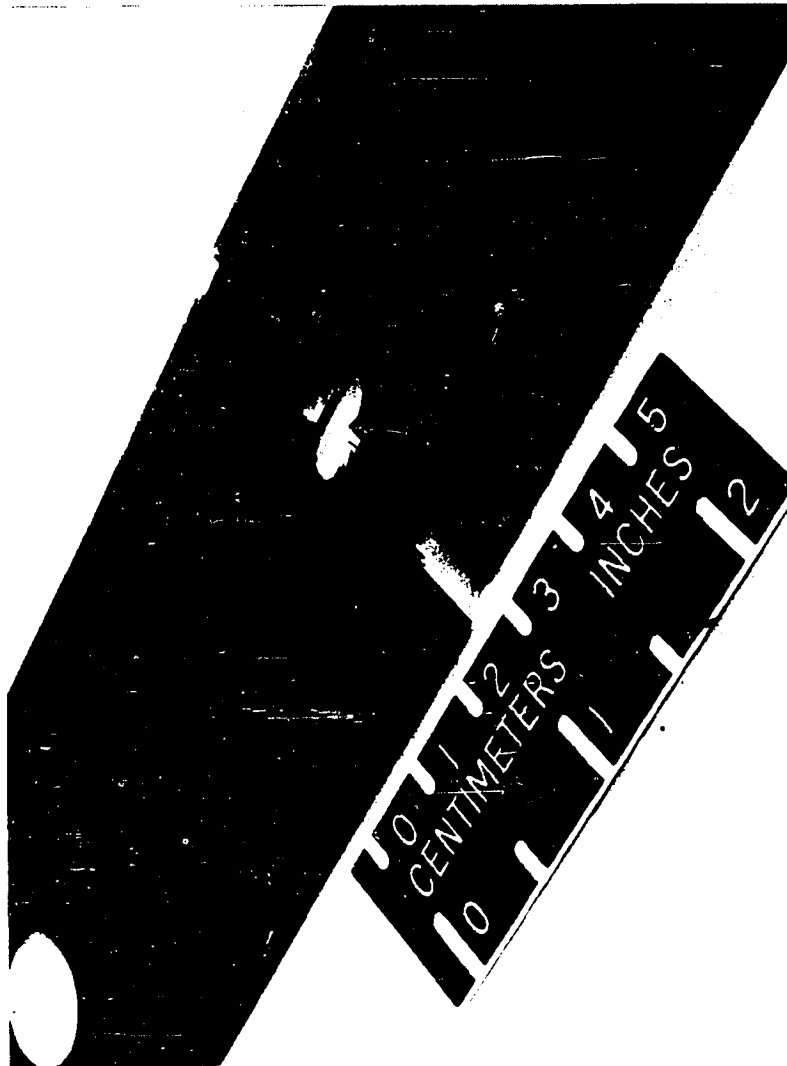
Fig. 63 Photograph of failed specimen showing net-section tension failure.
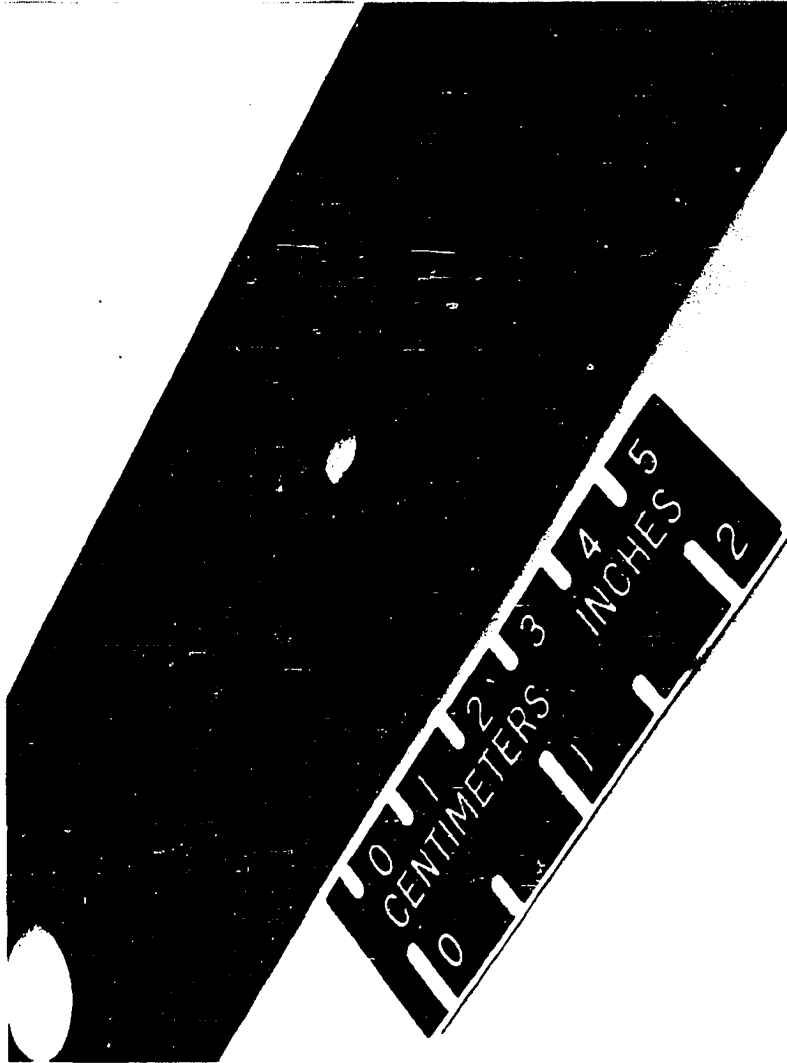
Fig. 64 Photograph of failed specimen showing bearing failure.

bearing loads. As shown in Fig. 62(c), CRB damage developed at the lower edge of the hole. Damage onset for $\beta = -\infty$ occurred at a slightly lower strength than for the tension-reacted bearing $\beta = \infty$, while the opposite was true for ultimate failure. This small difference may be due to strength variability and is not believed to be significant. The bearing-cutoff response, assumed for tension damage onset, does not apply for compression damage onset. However, as indicated by Hart-Smith [12,53], ultimate CRB failures may exhibit a bearing cutoff. For the $\beta = -\infty$ case, damage developed in the bearing failure mode and progressed until the specimen failed in the CRB mode.

When compression bypass loading was combined with compression-reacted bearing ($\beta = -3$), CRB damage developed at a lower load level than for the $\beta = -\infty$ case. Continued loading (at $\beta = -3$) caused ultimate failure in a new failure mode. Failed specimens showed considerable bearing damage at the hole combined with failure across the specimen width along a line offset from the hole. This "offset compression-bearing" (OCB) mode is shown in Fig. 65. For $\beta = -1$, damage-onset occurred mainly in the CRB mode, although some net-section compression (NC) damage was also present. Ultimate failure for this case occurred in the offset compression-bearing mode. Based on the results for the $\beta = -1$ and -3 cases, it may be concluded that CRB damage-onset at the hole (in the form of delamination) may have weakened the "offset-section" of the specimen thus leading to the offset compression-bearing failures observed.
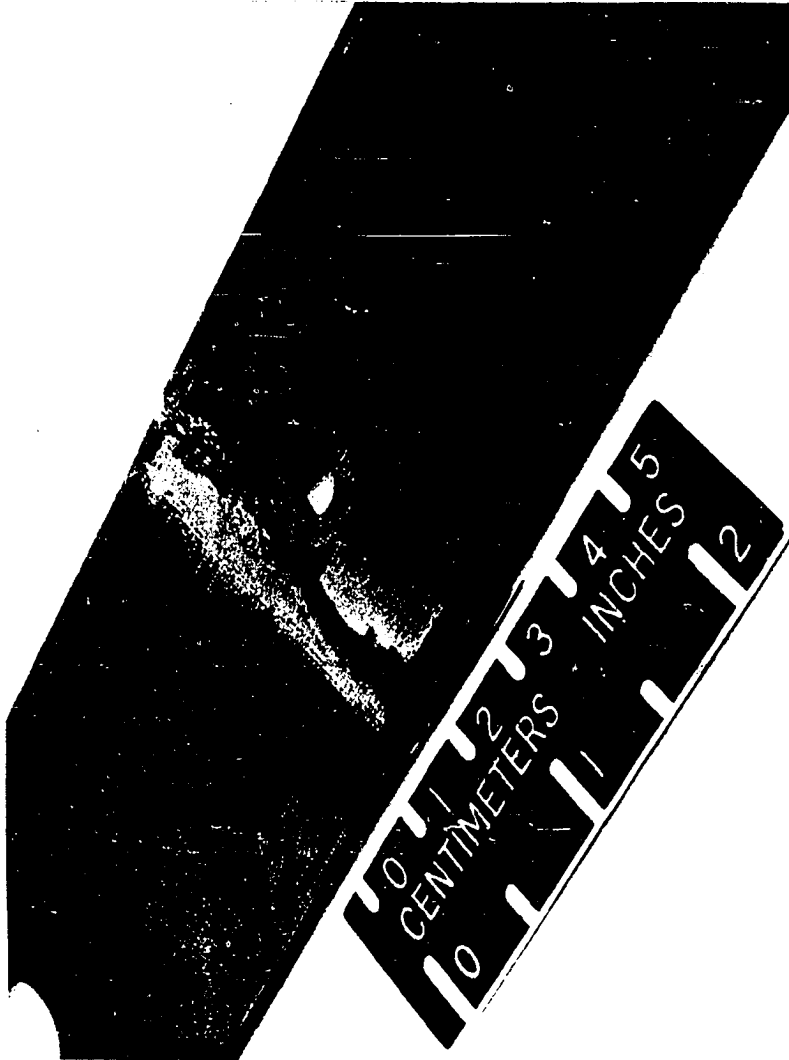
Fig. 65 Photograph of failed specimen showing "offset compression-bearing" failure.

For the remote compression case ($\beta = -0$) in Fig. 61, NC damage-onset occurred at -442 MPa, compared to 304 MPa for the corresponding $\beta = 0$ tension case. The basic laminate strength is only about 10 percent higher in compression than in tension, therefore, the higher NC damage-onset strength is believed to be attributable to the "dual" bolt-hole contact that allows load transfer across the hole. This load transfer decreases the net-section stress concentration and thereby increases the damage-onset strength for the NC mode. The dashed curve in Fig. 61 indicates the threshold for dual contact and will be discussed in the next section. The radiographs in Fig. 62 also show a difference between the NT and NC damage cases. Gray shadows, which indicate delamination, are evident in the NT radiographs but not in the NC radiographs. Ultimate failure for the remote compression case ($\beta = -0$) occurred abruptly after damage-onset in the NC failure mode. Some bearing damage was also evident at the hole and is believed to be a result of the dual bolt-hole contact.

Finally, the results in Fig. 61 can also be used to study failure sequences. For the tension cases ($\beta = 0$, 1 and 3), the onset of damage occurred in the NT failure mode and the specimens ultimately failed in the NT mode. For the $\beta = \infty$ and $-\infty$ cases damage developed in the bearing failure mode and resulted in ultimate bearing failures. The $\beta = -1$ and -3 cases showed an interaction of failure modes. Damage that initiated in the CRB mode may have caused a weakening of the offset-section resulting in the offset compression-bearing failure mode. NC damage-onset, for the $\beta = -0$ case, resulted in a NC ultimate failure mode.

134

Reproduced with permission of the copyright owner. Further reproduction prohibited without permission.

CHAPTER 5

STRENGTH PREDICTIONS

Predicting the strength for a laminate subjected to bearing-bypass loads involves two basic steps. First, the local stresses near the fastener hole must be accurately calculated. Second, the local stresses are then used in an appropriate failure criterion to predict a local failure mode and strength. A major problem associated with the use of fibrous composites in loaded hole applications is the selection of a suitable failure criterion. Typically, several failure modes are possible and a different failure criterion may be needed for each failure mode. In general, a governing stress (or combination of stresses) must be calculated for each failure mode and then compared with a corresponding failure criterion to determine the strength for each mode. The lowest such calculated strength is taken as the strength prediction for the laminate. Because the finite element stress calculations are acceptably accurate, the deficiencies in most strength predictions can be traced to the failure criterion or the associated procedures that were used.

In the present study, laminate stresses were calculated using the stress analysis procedures described in Chapter 2. A two-dimensional linear-elastic analysis was used. Any three-dimensional

effects that may be present were assumed to be small [36]. Damage-onset predictions were based on the elastic peak stresses at the hole boundary. It was assumed that the material response up to damage-onset is linear-elastic [14]. Predictions for ultimate failure were based on Whitney-Nuismer's [28] characteristic distance concept (Section 1.4) and the maximum stress criterion.

5.1 Damage-Onset Predictions

Damage-onset was assumed to be governed by the peak stresses at the hole boundary. The hole-boundary stresses corresponding to the measured damage onset strengths were calculated using the finite-element procedure described in Sections 2.2 and 2.3. The material properties (see Table 1) used in the analysis represented the quasi-isotropic T300/5208 graphite/epoxy specimens that were tested. The analysis model (see Fig. 23) represented a bolt-hole clearance of 1.2 percent of hole diameter. This corresponded to the nominal bolt-hole clearance used during testing. A finite element analysis was conducted for each test condition that corresponded to damage-onset. These stress analyses provided the basis for discussing the various bolt-hole contact conditions that developed during bearing-bypass testing. Furthermore, these stresses allowed the evaluation of the local interactions between bearing and bypass loads for both tension and compression.

5.1.1 Tension Stress Results

This section presents stresses for tension bearing-bypass loading corresponding to the measured damage-onset strengths. As

previously mentioned, these local stresses are then used to analyze the measured strength levels and failure modes.

Figure 66 shows $\sigma_{\theta\theta}$ and σ_{rr} stress distributions calculated along the hole boundary for four different cases. The $\beta = 0$ curve shows a familiar distribution of $\sigma_{\theta\theta}$ for the case of remote tension loading using the measured strength of $S_{np} = 304$ MPa. As previously mentioned in Section 4.4.1, the damage for this test case was found to develop in the NT mode and, therefore, was governed by the $\sigma_{\theta\theta}$ stress near $\theta = 90°$. The $\beta = 0$ curve has a peak value of about 812 MPa near $\theta = 90°$. This computed peak value grossly exceeds the unnotched laminate tensile strength of 414 MPa (see Table 1). Part of this discrepancy can be explained by the fact that the peak local stress acts over a very small volume of material subjected to a high stress gradient. The peak local strength should be higher than the unnotched tensile strength obtained using a relatively large tensile coupon under uniform stress. Also the NT damage onset reduced the stress concentration for the region of peak $\sigma_{\theta\theta}$ stress. Because the stress analysis did not account for this reduction, the computed peak $\sigma_{\theta\theta}$ was somewhat overpredicted. However, Ref. 14 showed that this computed $\sigma_{\theta\theta}$ peak corresponding to NT damage should agree with similar peak values calculated for the other cases with NT damage.

All four sets of curves in Fig. 66 correspond to the measured load levels for damage onset. For $\beta = 0$, 1 and 3, the $\sigma_{\theta\theta}$ curves have peak values near $\theta = 90°$, all within about 13 percent of 812 MPa, the peak value for $\beta = 0$. This is consistent with the earlier observation (see Section 4.4.1) that all three of these cases
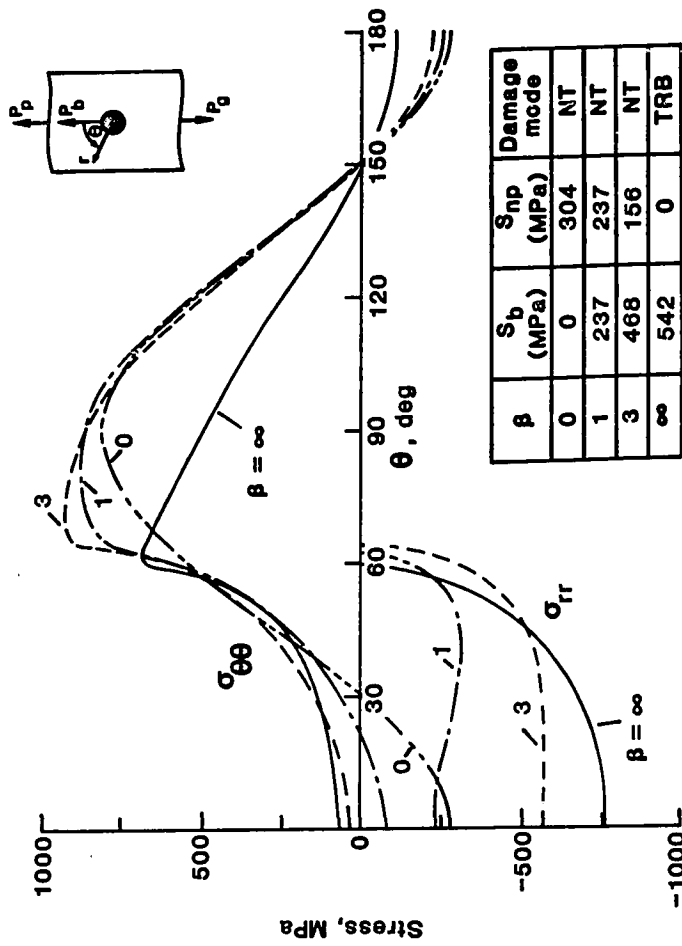
Fig. 66   Stresses along hole boundary for tension loading.

β	S_b (MPa)	S_{np} (MPa)	Damage mode
0	0	304	NT
1	237	237	NT
3	468	156	NT
∞	542	0	TRB

developed damage in the NT mode. The average peak stress, $\sigma_{nt} = 869$ MPa, for these three cases will be used later in the damage-onset predictions for NT damage. The two solid curves in Fig. 66 represent the tension-reacted bearing test case, $\beta = \infty$. The loading for this case corresponded to $S_b = 542$ MPa, the observed bearing damage-onset strength in tension. The peak σ_{rr} value of about -760 MPa exceeded the unnotched laminate compressive strength of 455 MPa (see Table 1), as expected. This peak value (σ_{bt}) of -760 MPa will be used later to indicate critical hole-boundary conditions for bearing damage onset in tension. For this bearing critical case, note that the $\sigma_{\theta\theta}$ peak of about 688 MPa is well below the critical ($\sigma_{nt} = 869$ MPa) level for NT damage. Conversely, the σ_{rr} peaks for $\beta = 1$ and 3 are well below the critical -760 MPa level for bearing damage.

5.1.2 Compression Stress Results

Figure 67 compares the hole-boundary stress distributions for the four compression test cases ($\beta = -0$, -1, -3, and $-\infty$). As expected, the $\sigma_{\theta\theta}$ and σ_{rr} curves for $\beta = -\infty$ are quite similar to those for $\beta = \infty$. The $\sigma_{\theta\theta}$ peak of about 556 MPa is somewhat lower than the 688 MPa peak for $\beta = \infty$ and much lower than the critical 869 MPa level for NT damage. The σ_{rr} peak of about -800 MPa for CRB damage is slightly larger than the -760 MPa level determined from the TRB $\beta = \infty$ case. This higher σ_{rr} peak for compression loading caused a lower damage-onset strength, compared to the corresponding tension case (see Fig. 61 and Table 3).

Recall that the CRB damage-onset strength decreased as the bypass load was increased, see the $\beta = -\infty$, -3, and -1 cases in

β	S_b (MPa)	S_{np} (MPa)	Damage mode
0	0	-422	NC
-1	314	-314	CRB/NC
-3	498	-166	CRB
-∞	528	0	CRB
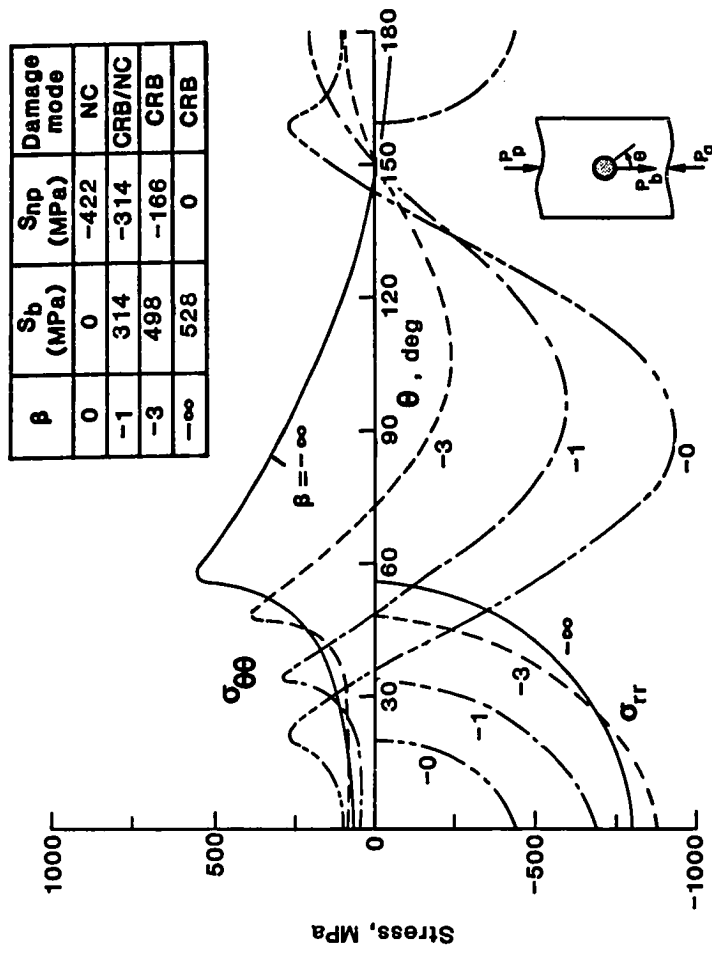
Fig. 67 Stresses along hole boundary for compression loading.

Fig. 61. This interaction was unexpected because the damage developed in the CRB mode and the compressive bypass loads were not believed to contribute to the σ_{rr} stresses that cause CRB damage. The interaction for CRB cases can be explained using Fig. 67. The peak σ_{rr} stresses for $\beta = -\infty$, -3, and -1 in Fig. 67 are nearly equal and are all within 9 percent of -808 MPa, the average peak stress for these three cases. Figure 67 also shows, that for these three cases, the lower the bearing load the smaller the contact angle. The smaller contact angles compensate for the smaller bearing loads. The compressive bypass loads decrease contact angle and allow the bearing loads to be more damaging. Therefore, the effect of the compressive bypass loads on the contact angle is responsible for the observed decrease in strength for CRB damage-onset. This discussion of contact angle suggests that a similar interaction probably exists in tension. The horizontal bearing-cutoff line, discussed in Section 4.4.1, probably underestimates the actual strength for small S_{np} levels. The average peak stress of -808 MPa will be used later as the critical stress, σ_{bc}, for CRB damage-onset predictions.

As previously mentioned, in Section 4.4.2, the compressive $\beta = -0$ case in Fig. 67 involves dual contact. For this case, the hole deforms enough to contact the bolt, starting at $\theta = 0$ and $180°$. The dashed curve in Fig. 68 (and Fig. 61) represents the calculated threshold for dual contact with a 0.076 mm initial bolt clearance (see Section 2.3.2 and Fig. 31). This dashed curve shows that contact started near $S_{np} = -220$ MPa for $\beta = -0$. The $\beta = -0$ curve in Fig. 67, for $S_{np} = -422$ MPa, shows that the contact extended by about $\pm 20°$ around $\theta = 0$ and $180°$. The $\sigma_{\theta\theta}$ curve for $\beta = -0$ has
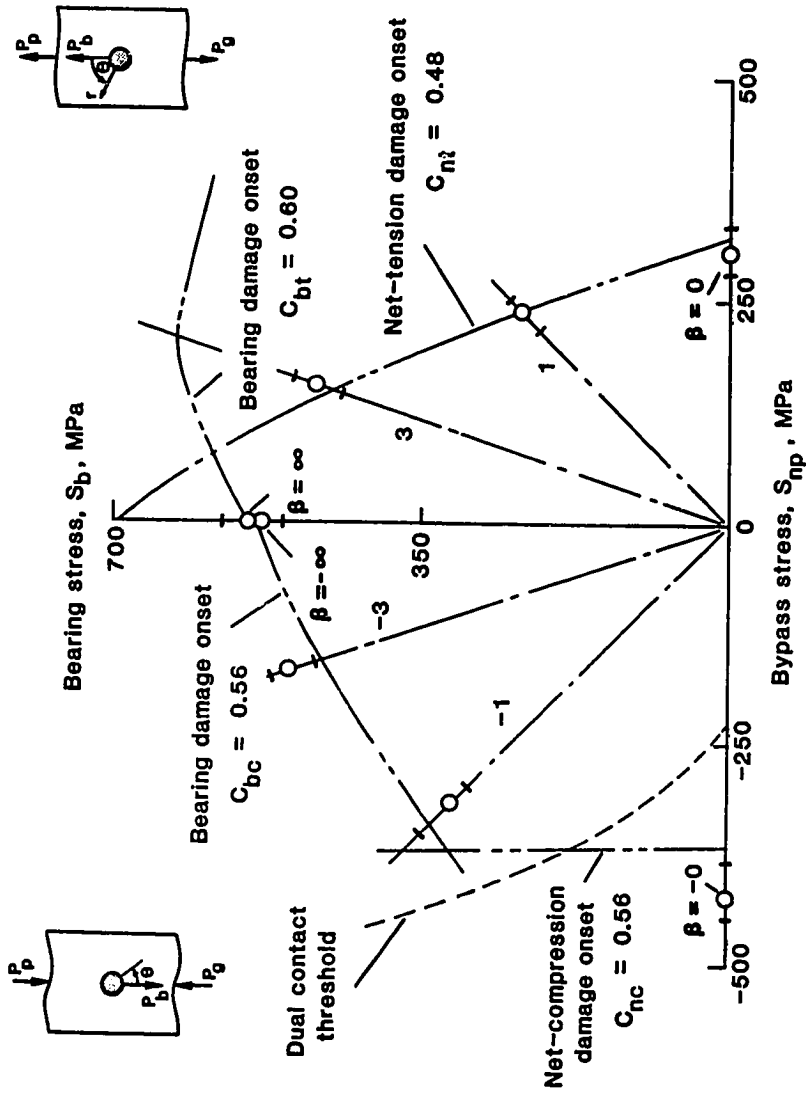
Fig. 68 Damage-onset predictions.

a compressive peak of about -940 MPa. This peak caused the net-section compression (NC) damage observed for this case. As discussed earlier (see Section 4.4.2), the dual contact in this case elevated the specimen strength by allowing load transfer across the hole. The β = -1 case showed some NC damage (see Fig. 61). The $\sigma_{\theta\theta}$ peak for this case, which may have caused the NC damage, was -694 MPa. Damage-onset predictions for NC damage will be based on the average of the $\sigma_{\theta\theta}$ peak stresses for the β = -0 and -1 cases. This critical (average) stress for NC damage-onset was σ_{nc} = -817 MPa.

The results in this and the previous section demonstrate that local hole-boundary stresses can be compared with critical stress levels to predict damage modes and damage-onset strengths.

5.1.3 Prediction Procedure

Damage initiation was assumed to be governed by the peak stresses at the hole boundary. Critical stress levels for each failure mode were determined, in the previous sections, from the appropriate peak stresses for the test cases that exhibited that failure mode. The critical stress levels calculated in Sections 5.1.1 and 5.1.2 were as follows:

$$\sigma_{nt} = 869 \text{ MPa} \quad \text{------} \quad \text{NT damage-onset}$$

$$\sigma_{bt} = -760 \text{ MPa} \quad \text{------} \quad \text{TRB damage-onset}$$

$$\sigma_{bc} = -808 \text{ MPa} \quad \text{------} \quad \text{CRB damage-onset}$$

$$\sigma_{nc} = -817 \text{ MPa} \quad \text{------} \quad \text{NC damage-onset.}$$

Net-tension damage-onset was predicted by setting the NT critical stress at the hole equal to the ultimate tensile strength, X_t, for the laminate. This produced the following equation:

$$C_{nt}\, \sigma_{nt} = X_t \tag{5.1}$$

The C_{nt} coefficient was introduced to account for the local stress gradient near the hole. Whereas the X_t value was obtained from coupons where a relatively large volume of material was subjected to a uniform stress, the material near the hole is subjected to a stress gradient and the peak stress exists only over a small volume. As a result, the hole boundary strength exceeds X_t. The coefficient C_{nt} attempts to account for this stress gradient effect and was computed by solving equation (5.1) for C_{nt} using the critical stress, σ_{nt}, for NT damage-onset. This resulted in a C_{nt} value of 0.48. To predict NT damage-onset, equation (5.1) was rewritten using this C_{nt} value as,

$$C_{nt}\, \frac{\sigma_{\theta\theta}}{X_t} \geq 1 \quad ; \quad C_{nt} = 0.48 \tag{5.2}$$

This empirical relationship is similar to that proposed in Ref. 14 to predict the damage-onset strength for bearing-loaded holes.

A similar expression was found for TRB damage-onset using the critical bearing stress σ_{bt} and the laminate compressive strength, X_c,

$$C_{bt} \frac{\sigma_{rr}}{X_c} \geq 1 \quad ; \quad C_{bt} = 0.60 \qquad (5.3)$$

The value of C_{bt} was calculated as 0.60 by a procedure similar to that used for determining C_{nt} .

For a given tension bearing-bypass case ($\beta \geq 0$), equations (5.2) and (5.3) can now be used to predict the damage-onset strength and the onset failure mode. The first load level at which either $\sigma_{\theta\theta}$ or σ_{rr} around the hole boundary satisfies either equation (5.2) or (5.3) will be the predicted load at which damage initiates. A NT damage mode would be predicted if $\sigma_{\theta\theta}$ satisfies equation (5.2). TRB damage would occur if equation (5.3) is satisfied. The damage location would be predicted as the location of the appropriate peak stress around the hole boundary.

Damage-onset for compression bearing-bypass can be predicted by a procedure similar to that described above for tension bearing-bypass. CRB damage-onset can be predicted by,

$$C_{bc} \frac{\sigma_{rr}}{X_c} \geq 1 \quad ; \quad C_{bc} = 0.56 \qquad (5.4)$$

and NC damage-onset will occur when,

$$C_{nc} \frac{\sigma_{\theta\theta}}{X_c} \geq 1 \quad ; \quad C_{nc} = 0.56. \qquad (5.5)$$

Figure 68 shows predictions for damage-onset, obtained by using the procedures described above. The laminate strengths used in

these predictions were 414 MPa and 455 MPa for the tension and
compression, respectively (see Table 1). Tension damage predictions
agreed reasonably well with the test data shown by open symbols. For
β = 0, 1 and 3, the tension-damage curve lies below the bearing
curve, indicating tension as the predicted damage-onset mode. For β
= ∞ bearing is the predicted mode. These trends agree with the
observed failure modes discussed earlier in Section 4.4.1. The
location of damage-onset can be predicted by looking at the stress
distributions in Fig. 66. For the β = 0 case, for example, the peak
$\sigma_{\theta\theta}$ stress occurs at θ = 90°. Damage-onset is most likely to start
at this location. This agrees with Fig. 62(a) which shows damage in
the vicinity of 90°.

The predicted curves for CRB and NC damage-onset, in Fig.
68, were constructed using equations (5.4) and (5.5). Again, the
predictions agree reasonably well with the test data shown by open
symbols. CRB damage-onset is predicted for β = -1, -3 and -∞. For
the β = -1 case the CRB-damage curve lies below the NC-damage curve
(along the β = -1 line), indicating bearing is the predicted mode.
An explanation for the presence of some NC damage for the β = -1 case
(see Table 3) can be found in Fig. 67. The $\sigma_{\theta\theta}$ stress for β = -1 has
a peak of about -694 MPa at around 90°. This peak stress, which may
have caused the NC damage, is only 15 percent below the critical
stress, σ_{nc}, for NC damage-onset.

5.2 Ultimate Strength Predictions

To predict the load at which a joint fails and the mode of failure, the conditions for failure must be established. In this investigation the joint is taken to have failed when the computed laminate stress (or stresses) has exceeded a prescribed limit at a "characteristic distance" from the hole boundary. The stress limit was evaluated using the maximum stress failure criterion. The characteristic distance was established by using Whitney and Nuismer's point-stress failure hypothesis [28] which assumes that failure (for open, unloaded holes) will occur when the computed stress at a characteristic distance from the hole exceeds the ultimate material strength (see Section 1.4). The characteristic distances r_{ot}, r_{oc} and r_{ocb} for net-tension, net-compression and offset compression-bearing failures, respectively, were determined using computed σ_{xx} stresses and appropriate laminate strengths.

5.2.1 Tension

Figure 69 shows the σ_{xx} stress distributions along the net-section for all the tension bearing-bypass test cases ($\beta = 0, 1, 3$ and ∞). These σ_{xx} stresses along the net-section were used to predict net-tension failures. The horizontal dashed-dot line corresponds to the laminate tensile strength, X_t, of 414 MPa (Table 1). The σ_{xx} stresses for the $\beta = 0, 1$ and 3 cases, which involved net-tension failures (Sec. 4.4.1), and the laminate tensile strength, X_t, were used to determine the characteristic distance, r_{ot}, for net-
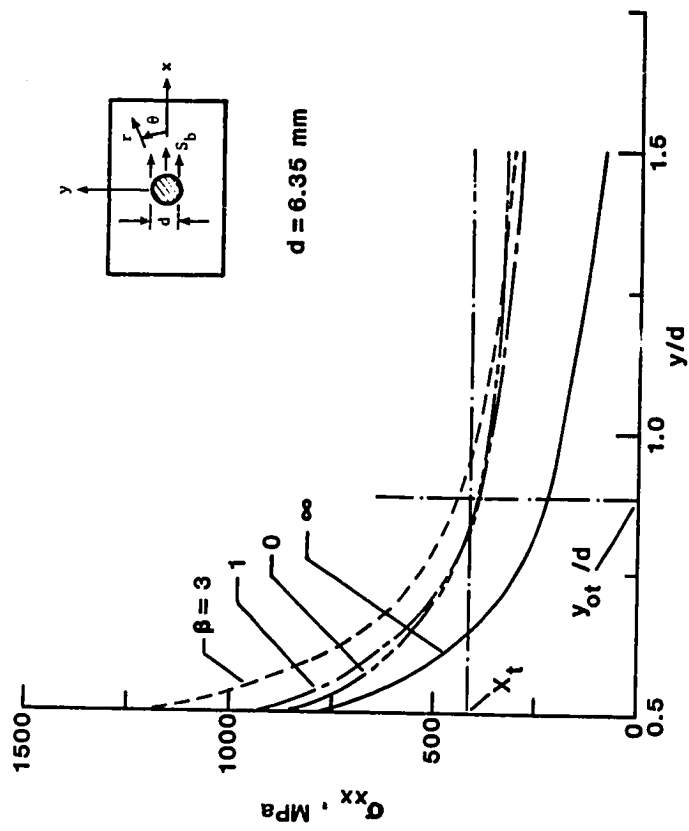
Fig. 69 Net-section σ_{xx} distributions for tension bearing–bypass.

tension failures. The value of (y_{ot}/d), shown in Fig. 69, was calculated as the average of the (y/d) values for the $\beta = 0$, 1 and 3 cases at which the stress distributions intersected the horizontal dashed-dot line (corresponding to X_t). This resulted in a (y_{ot}/d) value of 0.884. For a hole diameter, d, of 6.35 mm, this corresponds to a r_{ot} value (measured from the hole boundary) of 2.44 mm. This r_{ot} value was used along with the σ_{xx} stresses across the net-section to predict net-tension failure. The condition for failure was,

$$\frac{\sigma_{xx}}{X_t} \geq 1 \quad ; \quad at \quad r_{ot} = 2.44 \text{ mm.} \tag{5.6}$$

Figure 70 shows ultimate strength predictions for tension and compression bearing-bypass loads. The solid symbols represent test data (see Table 4) and the I-symbols around each solid symbol represent variability in the test data. The net-tension predictions were based on the procedure described above. The linear interaction trend (see Section 4.4.1) exhibited by the net-tension failure data is very well predicted by the above prediction procedure. Net-tension failures are predicted for the $\beta = 0$, 1 and 3 cases.

The $\beta = \infty$ test case was the only tension bearing-bypass case that exhibited a bearing failure mode. A horizontal bearing cutoff line was drawn through this data point. This was not a prediction but was based on earlier investigations by Hart-Smith [12]. A similar bearing cutoff line was also constructed through the $\beta = -\infty$ data point for compression bearing loading.
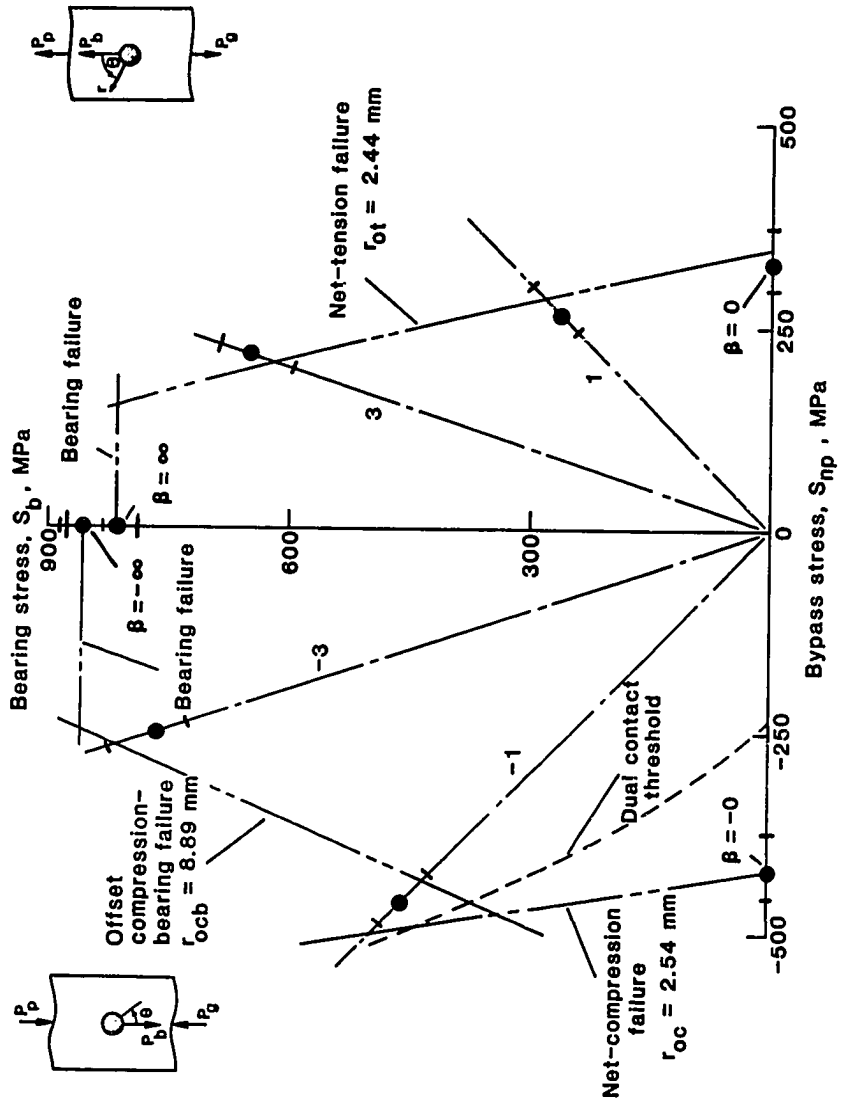
Fig. 70 Strength predictions for ultimate failure.

5.2.2 Compression

Figure 71 shows the σ_{xx} stress distributions along the loading axis (the x-axis) for the $\beta = -1$ and -3 cases which involved offset compression-bearing (OCB) failures. These σ_{xx} stresses were used to predict OCB failures. The horizontal dashed-dot line in Fig. 71 corresponds to the laminate compressive strength, X_c , of 455 MPa (see Table 1). The characteristic distance, r_{ocb} , for OCB failures was determined, by a procedure similar to that used for NT failures, as 8.89 mm. This r_{ocb} value was used together with the σ_{xx} stresses along the loading axis to predict OCB failure. The condition for failure was,

$$\frac{\sigma_{xx}}{X_c} \geq 1 \quad ; \quad \text{at } r_{ocb} = 8.89 \text{ mm.} \qquad (5.7)$$

Figure 70 shows predictions for OCB failures based on the above procedure. OCB failures are predicted for compression bearing-bypass cases with values of β between -1 and -3.

Figure 72 shows the σ_{xx} stress distributions along the net-section for the $\beta = -0$ and -1 cases. The $\beta = -0$ case involved net-compression (NC) failure and was thus used to determine the characteristic distance, r_{oc} , for NC failures. This r_{oc} (= 2.54 mm) was used together with the σ_{xx} stresses along the net-section to predict NC failure. The condition for failure was,

$$\frac{\sigma_{xx}}{X_c} \geq 1 \quad ; \quad \text{at } r_{oc} = 2.54 \text{ mm.} \qquad (5.8)$$
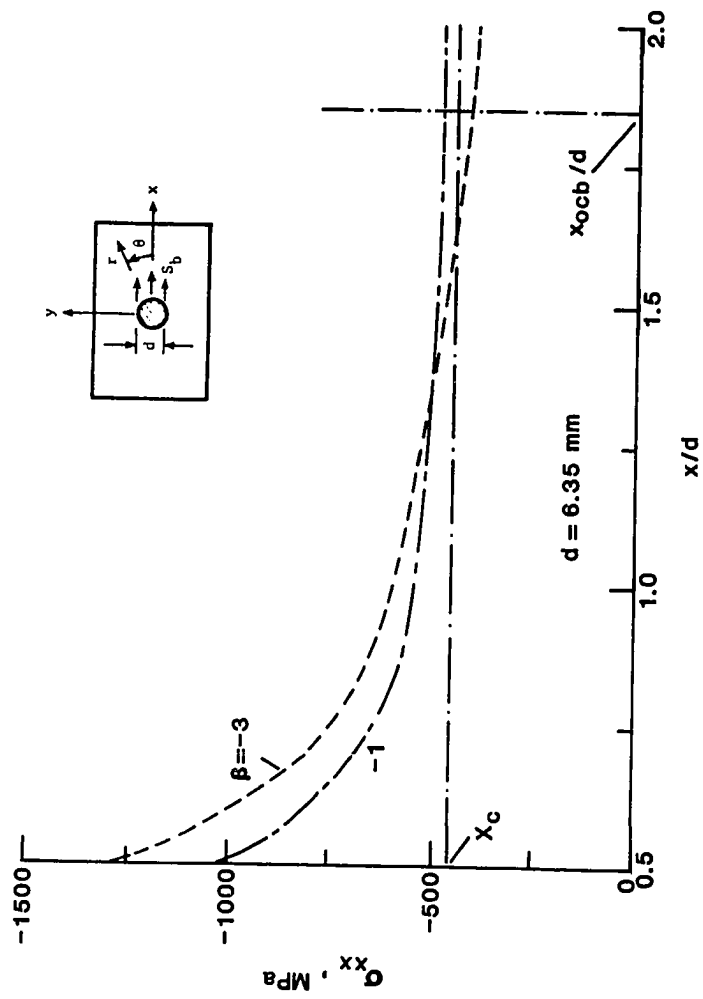
Fig. 71 Distributions of σ_{xx} along load axis for $\beta = -1$ and -3.
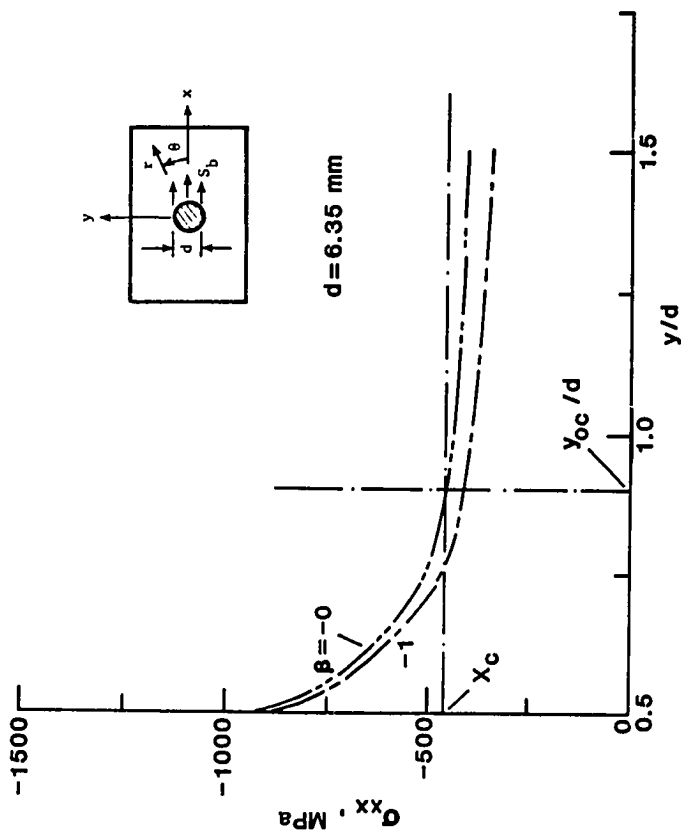
Fig. 72   Net-section σ_{xx} distributions for $\beta = -0$ and -1.

Figure 70 shows predictions for NC failures based on the above procedure. For the $\beta = -1$ case OCB failure is predicted at a lower load than NC failure. Therfore, the predicted failure mode, in this case, would be offset compression-bearing.

Equations (5.6), (5.7) and (5.8) can be used to predict NT, OCB and NC failures, respectively, by using the appropriate stresses at the appropriate characteristic distances. The predictions in Fig. 70 define a failure envelope over the entire range of bearing and bypass load combinations for the graphite/epoxy laminates. For any given combination of bearing and bypass loads, the designer could use Fig. 70 to predict the failure modes and strengths. Similar failure envelopes could be constructed for a different bolt-hole clearance by using equations (5.6-5.8) along with the stress analysis procedures described in Chapter 2.

The strength prediction procedures, described above, were also used with several failure criteria in addition to the maximum stress criterion. These other criteria were the Tsai-Hill [22], Tsai-Wu [26], Hoffman [24], Yamada-Sun [37], and the maximum strain criterion. However, none of the other criteria produced satisfactory predictions. Note that all of these other criteria involve multi-axial stress components. This suggests that the failures were governed primarily by the maximum stress, which in all cases was the x-axis stress component.

CHAPTER 6

SUMMARY AND CONCLUSIONS

This study addresses the need for an improved basic understanding of mechanically fastened joints in composites. The state-of-art of the research in composite bolted joints was reviewed and two important parameters that needed further investigation were identified. These were bolt-hole clearance effects and combined bearing and bypass load effects. First, a detailed analytical and experimental study was made of the effects of bolt-hole clearance on the contact and stresses around a fastener hole. Second, an extensive analytical and experimental study was made of the effects of combined bearing-bypass loading on the contact, stresses, failure modes and failure strengths of laminate fastener holes.

The effects of bolt-hole clearance on the contact and stresses around the fastener were studied both analytically and experimentally. A new finite element analysis technique was developed to analyze clearance-fit fastener holes. This method used an inverse formulation and conditions along the bolt-hole interface were specified by displacement constraint equations. After the method was verified, by comparison with previous work, it was then applied to the analysis of a simple joint with a smooth, rigid, clearance-fit bolt. For values of diametrical clearance, c_d, typically used in composite joints, the effect of clearance on the

contact angle, the local stresses, and joint stiffness were investigated.

The contact angle was found to be highly sensitive to changes in the clearance. Also the peak stresses and their locations were considerably influenced by the clearance. For example, when results for the c_d = 1.6 percent clearance case with a 475 MPa bearing stress were compared with the snug-fit reference case, the peak tangential stress was 16 percent higher, the peak radial stress was 36 percent higher, and the contact angle was 30 percent smaller than for this reference case. After a slight initial nonlinearity, the peak stresses, the hole elongation, and the overall plate deformation in a clearance-fit joint increased linearly with increasing stress level. At a bearing stress level of 1000 MPa for c_d = 1.6 percent, the hole elongation was 16 percent, greater than for the c_d = 0 reference case, whereas, the overall plate deformation was only 7 percent greater than the c_d = 0 case. These results suggest that the clearance in a mechanically fastened joint should be considered in stress and strength analyses but may have little influence on joint stiffness.

The finite element results for the load-contact angle variations and the local stresses were verified experimentally, especially, to assess the influence of bolt-hole friction which was neglected in the analysis. Various simple experimental techniques, using instrumented pins, were developed for the measurement of the nonlinear load-contact variation in a clearance-fit, pin-loaded hole. An instrumented pin, that activated a make-or-break electrical circuit in the pin-hole contact region, was found to be a simple and

effective technique. Because of the limitations of this technique another technique using an optical fiber sensing system was also developed and found to be very accurate. A layout fluid technique was more conveniently used for measuring contact angles in smaller diameter holes. Load-contact variations in photoelastic specimens were measured by observing the isochromatic fringe patterns around the bolt-hole interface. Photoelasticity was also used to obtain local stresses at clearance-fit fastener holes in order to verify the finite element stress results.

The test results for the load-contact variations and the local stresses lead to an assessment of the influence of interfacial friction. Whereas the load-contact angle variations for polycarbonate showed a discrepancy between the finite element results and the measured values, the stress distribution results did not differ greatly. This indicated that the interfacial friction influenced the contact angles more than the stresses. Thus, the simple finite element analysis, which did not account for interfacial friction, could be used to calculate reasonably accurate stresses around the hole.

The effects of combined bearing and bypass loading on laminate fastener holes were examined by testing graphite/epoxy specimens. Specimens were 16-ply, quasi-isotropic, T300/5208 graphite/epoxy laminates with a $[0/45/90/-45]_{2s}$ layup and were subjected to various bearing-bypass load ratios. Some specimens were tested upto damage-onset and unloaded to study damage-onset modes while other specimens were tested to failure. A finite element analysis was conducted for each test condition to determine how the

bearing-bypass loading influenced the interfacial contact and the local stresses near the fastener. The computed stresses were then used in a failure prediction procedure to analyze the test results.

Combination bearing and bypass loading was found to influence both the contact angles and the stresses around the hole. For tension bearing-bypass loading, an increase in bearing-bypass ratio decreased the interfacial contact angle. The opposite was true for compression bearing-bypass loading where an increase in bearing-bypass ratio increased contact angle. Some compression bearing-bypass ratios led to dual contact resulting in load transfer across the bolt. This led to lower stress concentrations at the hole and therefore higher strengths.

The effect of combined bearing and bypass loads on the failure modes and strengths was studied over the entire range of bearing-bypass ratios. Tension data showed a linear interaction for combined bearing-bypass loading with damage developing in the net-tension mode and growing to failure in the same mode. The compression bearing-bypass strengths for damage-onset showed an unexpected interaction involving the bearing mode. Compressive bypass loads reduced the bearing onset strength. This effect was analyzed and explained using the hole-boundary stresses. The compressive bypass loads were shown to decrease the bolt-hole contact arc and, thus, increase the severity of the bearing loads. Compression data for ultimate strength exhibited a failure mode called offset compression-bearing for combined bearing-bypass loading with damage developing in the bearing mode and causing a weakening of the offset-section leading to ultimate failure in the offset

compression-bearing mode. Damage-onset was predicted reasonably well using the peak stresses at the hole. Strength predictions indicated that damage corresponding to ultimate strength was governed by the maximum stress near the hole.

Furthermore, the present investigation predicted a failure envelope over the entire range of bearing and bypass load combinations for the graphite/epoxy laminates. For any given combination of bearing and bypass loads, the designer could use this failure envelope to predict the failure modes and strengths. Similar failure envelopes could be constructed for different bolt-hole clearances by using the stress analysis and strength prediction procedures developed in this study. Finally, the present study should help improve the basic understanding of composite bolted joints and lead to better structural design procedures.

The present investigation has also shown that further research is needed to investigate bearing damage-onset under tension bearing-bypass loading, especially, to verify the predicted trend (from the present analysis) for bearing damage-onset. More testing is required to investigate the effect of bearing-bypass loading on the net-compression damage-onset strength in the dual contact region. Also, an assessment of the effect of combined bearing-bypass loading on the onset and growth of interlaminar damage needs to be undertaken. Finally, laminate response under cyclic bearing-bypass loading needs to be explored.

REFERENCES

1. DOD/NASA Advanced Composites Design Guide, Vol.IV-A: Materials, First Edition, Contract No. F33615-78-C-3203, Air Force Wright Aeronautical Laboratories, July 1983. (Available as NASA CR-173407 and from DTIC as AD B080 184L.).

2. Crews, J. H., Jr., "A Survey of Strength Analysis Methods for Laminates with Holes," The Journal of the Aeronautical Society of India, Vol.36, No.4, Nov. 1984, pp. 287-303.

3. Collings, T. A., "The Strength of Bolted Joints in Multi-Directional CFRP Laminates," Composites, Jan. 1977, pp. 43-55.

4. Waszczak, J. P. and Cruse, T. A., "A Synthesis Procedure for Mechanically Fastened Joints in Advanced Composite Materials," AD-771795, Sept. 1973.

5. Quinn, W. J., and Matthews, F. L., " The Effect of Stacking Sequence on the Pin-Bearing Strength in Glass Fibre Reinforced Plastic," Journal of Composite Materials, Vol. 11, April 1977, pp. 139-145.

6. Prabhakaran, R., "Photoelastic Investigation of Bolted Joints in Composites," Composites, July 1982, pp. 253-256.

7. Hyer, M. W. and Liu, D., "Stresses in Pin-Loaded Orthotropic Plates : Photoelastic Results," Journal of Composite Materials, Vol. 19, March 1985, pp. 138-153.

8. Crews, J. H., Jr., Hong, C. S. and Raju, I. S., "Stress-Concentration Factors for Finite Orthotropic Laminates with a Pin-Loaded Hole," NASA TP 1862, May 1981.

9. Stockdale, J. H. and Matthews, F. L., "The Effect of Clamping Pressure on Bolt Bearing Loads in Glass Fibre-Reinforced Plastics," Composites, Jan. 1976, pp. 34-38.

10. Kretsis, G. and Matthews, F. L., "The Strength of Bolted Joints in Glass Fibre/Epoxy Laminates," Composites, Vol. 10, April 1985, pp.92-102.

11. Van Siclen, R. C. , "Evaluation of Bolted Joints in Graphite/Epoxy," Proceedings of the Army Symposium on Solid Mechanics, 1974: The role of mechanics in design-structural joints. AMMRC MS 74-8, Sept. 1974, pp. 120-138.

12. Hart-Smith, L. J., "Bolted Joints in Graphite-Epoxy Composites," NASA CR-144899, June 1976.

13. Crews, J. H., Jr., "Bolt-Bearing Fatigue of a Graphite/Epoxy Laminate ," ASTM STP 749, K. T. Kedward, Ed., American Society for Testing and Materials, 1981, pp. 131-144.

14. Crews, J. H., Jr. and Naik, R. V. A., "Failure Analysis of a Graphite/Epoxy Laminate Subjected to Bolt Bearing Loads," Composite Materials : Fatigue and Fracture, ASTM STP 907, H. T. Hahn, Ed., American Society for Testing and Materials, Philadelphia, 1986. Also NASA TM 86297, Aug. 1984.

15. Prabhakaran, R. and Naik, R. A., "Measurement of Contact Angle in a Clearance-Fit, Pin-Loaded Hole," Experimental Techniques, Feb. 1986, pp. 25-27.

16. Naik, R. A. and Crews, J. H., Jr., "Stress Analysis Method for a Clearance Fit Bolt Under Bearing Loads," Proceedings of AIAA/ASME/ASCE/AHS, 26th Structures, Structural Dynamics and Materials Conference, April 1985, Orlando, AIAA-85-0746, pp. 522-527.

17. Garbo, S. P., "Effects of Bearing/Bypass Load Interaction on Laminate Strength," AFWAL-TR-81-3114, Sept. 1981.

18. Ramkumar, R. L., "Bolted Joint Design," Test methods and design allowables for fibrous composites. ASTM STP 734, C. C. Chamis, Ed., 1981, pp. 376-395.

19. Ramkumar, R. L., "Bolt-Bearing/Bypass Study on Composite Laminates," NOR 78-154, Dec. 1978.

20. Ramkumar, R. L., Kulkarni, S. V., and Pipes, R. B., "Evaluation and Expansion of an Analytical Model for the Fatigue of Notched Composite Laminates," NASA-CR-145308, National Aeronautics and Space Administration, March 1978.

21. Waszczak, J. P. and Cruse, T. A., "Failure Mode and Strength Predictions of an Isotropic Bolt Bearing Specimens," Journal of Composite Materials, Vol. 5, July 1971, pp. 421-425.

22. Tsai, S. W.,"Strength Theories of Filamentary Structures," Fundamental Aspects of Fiber Reinforced Plastic Composites, R. T. Schwartz and H. S. Schwartz, editors, Wiley Interscience, New York, 1968, pp. 3-11.

23. Oplinger, D. W. and Gandhi, K. R., "Stresses in Mechanically Fastened Orthotropic Laminates," Proc. the Second Conference on Fibrous Composites in Flight Vehicle Design, AFFDL-TR-74-103, Sept. 1974, pp. 813-841.

24. Hoffman, O., "The Brittle Strength of Orthotropic Materials," Journal of Composite Materials, Vol. 1, 1967, pp. 200-206.

25. Soni, S. R. , "Stress and Strength Analysis of Bolted Joints in Composite Laminates," Composite Structures, edited by I. H. Marshall, Applied Science Publishers, London and New Jersey, 1981, pp. 50-62.

26. Tsai, S. W., and Wu, E. M., "A General Theory of Strength for Anisotropic Materials," Journal of Composite Materials, Vol. 5, Jan. 1971, pp. 58-80.

27. Eisenmann, J. R., "Bolted Joint Static Strength Model for Composite Materials," Third Conference on Fibrous Composites in Flight Vehicle Design, NASA TM X-3377, April 1976.

28. Whitney, J. M., and Nuismer, R. J., "Stress Fracture Criteria for Laminated Composites Containing Stress Concentrations," Journal of Composite Materials, Vol. 8, July 1974. pp. 253-265.

29. Nuismer, R. J., and Whitney, J. M., "Uniaxial Failure of Composite Laminates Containing Stress Concentrations," Fracture Mechanics of Composites, ASTM STP 593, 1975, pp. 117-142.

30. Agarwal, B. L., "Static Strength Prediction of Bolted Joints in Composite Material," Presented at 20th Structures, Structural Dynamics, and Materials Conference, St. Louis, MO, April 4-6, 1979 (AIAA Paper 79-0799).

31. Garbo, S. P., and Ogonowski, J. M., "Effect of Variances and Manufacturing Tolerances on the Design Strength and Life of Mechanically Fastened Composite Joints," Vol. 1, Methodology Development and Data Evaluation, AFWAL-TR-81-3041, Vol.1, April 1981.

32. Karlak, R. F., "Hole Effects in a Related Series of Symmetrical Laminates," Proceedings of Failure Modes in Composites IV," Am. Soc. Metals, Chicago, 1977, pp. 105-117.

33. Pipes, R. B., Wetherhold, R. C., and Gillespie, J. W., Jr., "Superposition of Notched Strength of Composite Laminates," Polymer Engineering and Science, Dec. 1979, Vol. 19, No. 16, pp. 1151-1155.

34. Wilson, D. W., and Pipes, R. B., "Analysis of the Shearout Failure Mode in Composite Bolted Joints," Composite Structures, edited by I. H. Marshall, Applied Science Publishers Inc., Englewood, London and New Jersey, 1981, pp. 34-49.

35. York, J. L., Wilson, D. W., and Pipes, R. B., "Analysis of the Net Tension Failure Mode in Composite Bolted Joints," Journal of Reinforced Plastics and Composites, Vol. 1, April 1982, pp. 141-152.

36. Chang, F. K., Scott, R. A., and Springer, G. S., "Strength of Mechanically Fastened Composite Joints," Journal of Composite Materials, Vol. 16, Nov. 1982, pp. 470-494.

37. Yamada, S. E., and Sun, C. T.. "Analysis of Laminate Strength and its Distribution ," Journal of Composite Materials, Vol. 12, July 1978, pp. 275-284.

38. Harris, H. G., Ojalvo, I. U., and Hooson, R. E., "Stress and Deflection Analysis of Mechanically Fastened Joints," Grumman Aerospace Corp., Bethpage, New York, Air Force Flight Dynamics Lab., Contract Rep. No. AFFDL-TR-70-49 (AD-709-221), May 1970.

39. Oplinger, D. W. and Gandhi, K. R., "Analytical Studies of Structural Performance in Mechanically Fastened Fibre-Reinforced Plates," Proc. Army Symp. on Solid Mech., 1974: The Role of Mech. in Design - Struct. Joints, pp. 211-242. Army Mater. and Mech. Res. Center, Watertown, Mass., Rep. No. AMMRC MS 74-8 (AD 786 543), Sept. 1974.

40. Eshwar, V. A., "Analysis of Clearance Fit Pin Joints," International Journal of Mechanical Sciences, Vol. 20, 1978, pp. 477-484.

41. Mangalgiri, P. D., Dattaguru, B., and Rao, A.K, "Finite Element Analysis of Moving Contact in Mechanically Fastened Joints," Nuclear Engineering Design, Vol. 78, 1984, pp. 303-311.

42. Francavilla, A. and Zienkiewicz, O. C., "A Note on Numerical Computation of Elastic Contact Problems," International Journal for Numerical Methods in Engineering, Vol. 9, 1975, pp. 913-924.

43. White, D. J. and Enderby, L. R., "Finite Element Stress Analysis of a Nonlinear Problem: A Connecting-Rod Eye Loaded by Means of a Pin," Journal of Strain Analysis, Vol. 5, No. 1, 1970, pp. 41-48.

44. Sholes, A. and Strover, E. M., "The Piecewise-Linear Analysis of Two Connecting Structures Including the Effect of Clearance at the Connections," International Journal for Numerical Methods in Engineering, Vol. 3, 1971, pp. 45-51.

45. Chan, S. K. and Tuba, I. S., "A Finite Element Method for Contract Problems of Solid Bodies-Part I. Theory and Validation," International Journal of Mechanical Sciences, Vol. 13, 1971, pp. 615-625.

46. Rao, A. K., "Elastic Analysis of Pin Joints," Computers and Structures, Vol. 9, 1978, pp. 125-144.

47. Wilkinson, T. L., Rowlands, R.E. and Cook, R. D., "An Incremental Finite-Element Determination of Stresses Around

Loaded Holes in Wood Plates," Computers and Structures, Vol. 14, No. 1-2, 1981, pp. 123-128.

48. Kim, W., "Stress Analysis Methods for Clearance-Fit Mechanical Joints in Laminated Composites," Ph.D. Thesis, Rensselaer Polytechnic Institute, 1982.

49. Pradhan, B. and Kumar, R., "Stresses Around Partial Contact Pin-Loaded Holes in FRP Composite Plates," Journal of Reinforced Plastics and Composites, Vol. 3, January 1984, pp. 69-84.

50. Dally, J. W. and Riley, W. F., Experimental Stress Analysis, Second Edition, McGraw-Hill, Inc., 1978.

51. Concannon, G., "Design Verification Testing of the X-29 Graphite/Epoxy Wing Covers," Proceedings of the Fall Meeting, Society of Experimental Stress Analysis, Salt Lake City, Utah, 1983, pp. 96-102.

52. Crews, J. H., Jr., and Naik, R. A., "Combined Bearing and Bypass Loading on a Graphite/Epoxy Laminate," Proceedings of the International Symposium on Joining and Repair of Fibre-Reinforced Plastics, London, UK, September 1986. Also published as NASA TM 87705, April 1986.

53. Hart-Smith, L. J., "Design Methodology for Bonded-Bolted Composite Joints, Vol. 1, Analysis Derivations and Illustrative Solutions," AFWAL-TR-81-3154, Vol. 1, Feb. 1982.

BIOGRAPHY

Rajiv Vikas Arun Naik was born in Pune, India, on April 20, 1956. He graduated from St. Vincent's High School, Pune, India, in 1972. In 1979, he graduated from the Indian Institute of Technology-Powai, Bombay, India, with a Bachelor's degree in Mechanical Engineering. He then joined the Ruston & Hornsby (I) Ltd. company as a Production Engineer. In 1980, he came to the United States to pursue graduate studies. He received his Master of Science degree in Mechanical Engineering from the University of Maine at Orono, Orono, Maine in 1982. In July 1982, he moved to Norfolk, Virginia and since then he has worked towards a Ph.D. degree in Engineering Mechanics at the Old Dominion University, Norfolk, Virginia under a joint NASA-ODU Research Participation in Aeronautics Program. In 1986, he was elected to membership in The Honor Society of Phi Kappa Phi. During the course of his graduate work, he has co-authored the following publications:

1. Schmidt W. F., and Naik R. A.; "Finite Element Analysis of the Extrusion of Metals." International Journal of Modelling & Simulation, Vol. 3, No. 3, 1983.

2. Crews J. H. Jr., and Naik R. A.; "Failure Analysis of a Graphite/Epoxy Laminate Subjected to Bolt Bearing Loads." NASA TM 86297, August 1984. Also ASTM STP 907, 1986, pp. 115-133.

3. Naik R. A., and Crews J. H. Jr.; "Stress Analysis Method for a Clearance Fit Bolt Under Bearing Loads." Proceedings AIAA/ ASME/ ASCE/ AHS, 26th Structures, Structural Dynamics and Materials Conference, Orlando, Florida, April 1985. To be published in AIAA Journal, July 1986.

4. Prabhakaran R., and Naik R. A.; "A Technique for the Measurement of Contact in a Clearance Fit, Pin Jointed Connection." Experimental Techniques, Feb. 1986, pp. 25-27.

5. Prabhakaran R., and Naik R. A.; "An Analytical and Experimental Study of Contact, Stresses, and Failure in Clearance Fit, Pin Loaded Polycarbonate Specimens." Proceedings of the 1986 Spring Conference on Experimental Mechanics, New Orleans, Louisiana, June 1986.

6. Crews J. H. Jr., and Naik R. A.; "Bearing Bypass testing of a Graphite/Epoxy Laminate." Submitted for presentation at International Symposium on Joining and Repair of Fibre-Reinforced Plastics, London, UK, September 1986. Also published as NASA TM 87705, April 1986.

7. Prabhakaran R., and Naik R. A.; "Investigation of Non-Linear Contact for a Clearance-Fit Bolt in a Graphite/Epoxy Laminate." Submitted for presentation at International Symposium on Joining and Repair of Fibre-Reinforced Plastics, London, UK, September 1986.